Flow modelling of Ti-6Al-4V under moderate and large strains

MASTER'S THESIS

to achieve the university degree of

Diplom-Ingenieurin

Master's degree programme: Advanced Materials Science

submitted to

Graz University of Technology

Supervisor

Assoc.Prof. Dr.techn. Maria Cecilia Poletti

Institute of Materials Science, Joining and Forming

Graz, January 2019

AFFIDAVIT

I declare that I have authored this thesis independently, that I have not used other than the declared sources/resources, and that I have explicitly indicated all material which has been quoted either literally or by content from the sources used.
The text document uploaded to TUGRAZonline is identical to the present master‘s thesis.

Date Signature

Acknowledgements

The author wants to thank the FWF Project for Flow localizations and instabilities and the CD Laboratory for Design of High-Performance Alloys by Thermomechanical Processing for the support of the work, carried out during this masters's thesis.

I would like to thank my supervisor Cecilia Poletti for her competent and friendly help and hope, my work will also be of some use in future projects. I am also grateful to the whole IMAT team and institute for providing me with the necessary equipment and the many experts in different fields. Up front I have to thank here Sandra Wesener for her nice assistence in every administrative matter.

Finally, I want to thank my family and friends for supporting me throughout the work of this thesis and keeping up also with the exhausted and annoyed version of myself. Especially Desirée Weiß and Ladislaus Lang-Quantzendorff have been my dear companions along the way and I hope, we will all finish our studies both with relieve and excitement for future challenge.

I can call myself a really lucky woman, that the one person most special in myself does not only understand the troubles of my heart, but also of my mind.

Index

Abstract

The wide field of applications for the titanium alloy Ti-6Al-4V(Ti64) demands for accurate design and predictability of hot deformation processes. By understanding the underlying metallurgical phenomena, the evolution of microstructure and flow stresses during deformation processes can be modelled. This work uses flow stresses obtained experimentally by hot compression and hot torsion tests at different strain rates and temperatures to validate physical based flow models. For this purpose, hot torsion tests are carried out within this work by means of a Gleeble® 3800. Two different physically based models are implemented for Ti64 in the β phase field and are compared regarding their input and output parameters. Firstly, a Kocks and Mecking model is adapted for the present titanium alloy. A good agreement of modelled and experimental curves is obtained up to moderate strains. Additionally, an overall dislocation density evolution is generated as output. Secondly, a model of continuous dynamic recrystallization (CDRX) based on the work of Montheillet et al. for aluminium is implemented after some modification for Ti64. The model consists of a more detailed description of the microstructure, based on different dislocation densities and grain boundaries. All these internal variables evolve by a production and a recovery term correlated phenomenologically with temperature and strain rate. Beside the flow stress, the model outputs are the total, the interior and the wall dislocation densities as well as the formation of new grains by continuous dynamic recrystallization at large strains. The model can describe the softening occurring during large strain deformations, partly produced by the formation of new high angle grain boundaries (HAB). The fraction of HAB is used to determine the recrystallization grade, validated with microstructural characterization of samples deformed by hot torsion.

Kurzfassung

Das breite Anwendungsfeld der Titanlegierung Ti-6Al-4V(Ti64) fordert präzises Design und präzise Vorhersagbarkeit von Warmumformprozessen. Ein Verständnis der zugrundeliegenden metallurgischen Phänomene erlaubt das Modellieren der Entwicklungen in Gefüge und Fließspannung während einer Umformung. Die vorliegende Arbeit zieht experimentell bestimmte Fließspannungen aus heißen Druck- und Torsionsversuchen bei verschiedenen Temperaturen und Dehnraten zur Validierung physikalisch basierter Fließmodelle zu Rate. Zu diesem Zweck werden Torsionsversuche mit einer Gleeble® 3800 durchgeführt. Zwei unterschiedliche Modellansätze werden für Ti64 im β-Phasenzustand implementiert und bezüglich ihrer Eingangs- und Ausgangsgrößen verglichen. In einem ersten Schritt wird ein Kocks-Mecking-Modell für die vorliegende Legierung adaptiert. Es liegt eine gute Übereinstimmung zwischen modellierten und experimentellen Werten bis zu moderaten Dehnungen vor. Als zusätzliche Ausgabe generiert das Modell die Entwicklung der totalen Versetzungsdichte mit der Dehnung. In einem zweiten Schritt wird ein Modell zu kontinuierlich dynamischer Rekristallisation (CDRX), basierend auf der Arbeit von Montheillet et al. für Aluminium, modifiziert und für Ti64 weiterentwickelt. Das Modell setzt sich aus einer detaillierten Beschreibung des Gefüges, basierend auf verschiedenen Arten von

Versetzungsdichten und Korngrenzen zusammen. Die Entwicklung dieser verschiedenen internen Variablen wird durch einen Erholungs- und einen Produktionsterm beschrieben, die phänomenologisch mit Temperatur und Dehnrate korreliert werden. Neben der Fließspannung sind die totale, die interne und die Wandversetzungsdichte die Ausgaben dieses Modells, sowie die Bildung von neuen Körnern durch kontinuierlich dynamische Rekristallisation bei hohen Dehnungen. Das Modell ist in der Lage die Entfestigung während Umformungen hoher Dehnung zu beschreiben, die teilweise aus der Bildung neuer Großwinkelkorngrenzen (HAB) resultiert. Der Anteil an HAB wird als Indiz für den Rekristallisationsgrad benötigt, welcher durch Charakterisierung der Mikrostruktur von Torsionsproben bestätigt wird.

Abbreviations

CDRX	continuous dynamic recrystallization
DDRX	discontinuous dynamic recrystallization
DRV	dynamic recovery
EBSD	electron backscatter diffraction
FEM	finite element method
GDRX	geometric dynamic recrystallization
HAB	high angle boundary
HTC	heat transfer coefficient
KHL model	Khan–Huang–Liang model
KM model	Kocks Mecking model
LAB	low angle boundary
PA	power angle
PTemp	programmed temperature
RMSE	root mean square error
RWTH	Rheinisch-Westfälische Technische Hochschule
RX	recrystallization
SiN	silicon mononitride
TC	thermocouple
Ti	titanium
Ti-7333	Ti-7Mo-3Nb-3Cr-3Al
Ti5553	Ti-5Al-5Mo-5V-3Cr
Ti64	Ti-6Al-4V

Symbols

α…	numerical constant
α'…	hexagonal martensite in Ti
α''…	orthorhombic martensite in Ti
α_1…	fraction of dislocations forming new LAB
a…	lattice parameter
a_{0-2}…	parameters for iteration process
A…	constant
A_1…	constant
A_2…	constant
b…	Burgers vector
b_{0-2}…	parameters for iteration process
B….	different constant
$\dot{\gamma}$…	shear strain rate
c…	lattice parameter

c_{0-2}…	parameters for iteration process
C…	material constant
C_p…	specific heat
D…	average size of crystallites
D_0^p…	upper bound strain rate
dV…	volume swept by mobile HAB
δ…	density
Δt…	time increment
ΔT…	difference in temperature
ε…	strain
ε_0…	initial strain
ε_{eff}…	initial strain
$\dot{\varepsilon}$…	strain rate
ε^p…	effective plastic strain
$\dot{\varepsilon}^*$…	normalizing strain rate
f_{ρ_w}…	factor for the wall dislocation density
f_{HAB}…	fraction of HAB
f_{YS}…	factor for yield stress function
G…	shear modulus
h_1…	hardening coefficient
$h_{0,1}$…	initial value for hardening coefficient
h_2…	recovery coefficient
$h_{0,2}$…	initial value for recovery coefficient
h_{all}…	overall HTC
HTC…	interface heat-transfer coefficient
$K_{HAB/LAB}$…	Hall-Petch constant for HAB and LAB, respectively
K_w…	workpiece thermal conductivity
K_D…	die thermal conductivity
η…	adiabatic correction factor
l…	sample length
m…	strain rate sensitivity
m_{h_1}…	strain rate sensitivity for h_1
m_{h_2}…	strain rate sensitivity for h_2
M…	Taylor factor
N…	number of torsion revolutions
n…	experimental hardening coefficient
n_1…	material specific constant
n_0…	material specific constant
n_w…	set of dislocations considered to form a LAB
ρ…	dislocation density
ρ_0…	initial dislocation density
ρ_i…	interior immobile dislocation density
ρ_{LAB}…	LAB dislocation density

$\rho_m \cdots$	mobile dislocation density
$\rho_w \cdots$	wall dislocation density
$\dot{\rho}_x \cdots$	dislocation density rate
$\dot{\rho}_x^+ \cdots$	production rate of dislocation density
$\dot{\rho}_x^- \cdots$	reduction rate of dislocation density
$Q_{h_1} \cdots$	activation energy for h_1
$Q_{h_2} \cdots$	activation energy for h_2
$r \ldots$	radius of torsion sample
$\mathrm{R}^2 \ldots$	coefficient of determination
$\sigma \ldots$	flow stress
$\sigma_{ath} \cdots$	athermal contribution to the flow stress
$\sigma_{eff} \cdots$	effective flow stress
$\sigma_{corr} \cdots$	corrected flow stress
$\sigma_{HP} \cdots$	Hall Petch contribution to the flow stress
$\sigma_{meas} \cdots$	experimentally measured flow stress
$\sigma_{mod} \cdots$	modelled flow stress
$\sigma_{th} \cdots$	thermal contribution to the flow stress
$\sigma_{YS} \cdots$	yield stress
$\sigma_\infty \ldots$	steady-state stress
$S_{V(LAB/HAB)} \cdots$	total area of boundaries (LAB and HAB, respectively) per unit volume
$\bar{\theta} \ldots$	average misorientation angle
$\theta_0 \cdots$	starting misorientation angle
$\theta_c \ldots$	critical misorientation angle
$\tau_{HP_{HAB/LAB}} \cdots$	shear stress contribution by Hall Petch
$T \ldots$	temperature
$T_m \ldots$	melting temperature
$T_{ref} \ldots$	reference temperature
$v \ldots$	average dislocation glide velocity
$v_{HAB} \cdots$	velocity of HABs
$\varphi(\theta) \ldots$	distribution function of the misorientation angle
$x_D \cdots$	distance from the die surface to the die interior
$x_w \cdots$	half of the workpiece height
$Z \ldots$	Zener-Hollomon parameter

1. Introduction

Ti-6Al-4V (Ti64) is the most frequently used titanium alloy. The wide field of applications rose the interest for designing forming processes at elevated temperatures. The alloy presents allotropic phase transformation, with a β transus temperature of 1000°C. To optimize and design hot deformation processes, the underlying metallurgical phenomena need to be described and correlated with the flow stresses evolution. If the temperature exceeds half of the melting temperature of the material, the microstructure may evolve dynamically during deformation. Flow curves at high temperatures can help to better plan and understand required forces for forming, accurate dimensional control of final parts and process simulations for various metals. Especially with the advancing power of computer simulations like the finite element method (FEM), accurate flow stress curves are essential as input parameter to secure the proper simulation of the software. [1], [2]

A large variety of models exists in the literature describing the hot deformation behaviour of Ti64. While phenomenological models depend on experimentally derived parameters, physical-based models try to correlate the macroscopic property of the flow stress with modelled mechanisms in the microstructure. Regarding moderate stresses a satisfying degree of predictability of the flow behaviour is reached with the existing methods. Contrary, for large strains only few attempts have been made to model the flow behaviour. As for higher degrees of deformation the complexity of metallurgical phenomena in the material rises, also models have to account for these mechanisms. [3], [4], [5]

The present work aims to model the flow behavior in the β field of Ti64 during hot deformation at moderate and large strains using two different approaches. In a first step, the flow stress up to strains of 0.8 is modelled with a Kocks Mecking model and validated with experimentally obtained hot compression flow curves. As the model assumes isothermal conditions during the deformation, the experimental data is corrected for deformation heating during the tests. As the flow stress in the Kocks Mecking model is only a function of one total dislocation density, the evolution of the latter is here the only description of the microstructure. In a second step, a model is implemented to predict the flow behavior of Ti64 at large strains. For this purpose, a model that implements the process of continuous dynamic recrystallization for Ti5553 is adapted. The goal is to find a suitable model to describe internal variables representing the microstructure in the β field and also to predict the macroscopic quantity of the flow stress. For the validation of the results obtained for large strains, hot torsion experiments are carried out with Ti64 using a Gleeble® 3800.

The input and output of both models are discussed. Especially the total amount and evolution of dislocation density gives an insight about the assumptions made by the two models.

2. State of the art

2.1.Titanium alloys and Ti-6Al-4V

Titanium has an abundance of 0.6% in the earth's crust and therefore belongs to the fourth most abundant structural metals with iron, aluminium, and magnesium. Titanium has the highest strength to density ratio compared to other metals and is used in different areas of research and industry. Apart from the widespread use in aerospace applications titanium is used in chemical, power and automotive industry as well as for medical applications, consumer goods and in civil engineering. The high strength, low density and superior corrosion resistance make it an attractive material for all these various applications. When it comes to the requirements of high strength and high fatigue resistance, the widely used pure titanium is often replaced by the alloy Ti-6Al-4V (Ti64). [1]

The crystal structure of pure titanium at room temperature is hexagonal. The lattice parameters of the so called α phase are a = 0.295 nm and c = 0.468 nm and are close to the ideal ratio of a hexagonal close-packed structure. In the α phase there are three different kinds of densely packed planes: one basal plane (0002), three prismatic planes $\{10\bar{1}0\}$, and six pyramidal planes $\{10\bar{1}1\}$. $<11\bar{2}0>$ are the indices of the close-packed directions. At 882°C titanium undergoes an allotropic phase transition to the body-centred cubic β phase (the lattice parameter at 900°C is a = 0.332 nm). Like for any bcc structure, the β phase crystal has six densely packed planes {110} with the directions <111>. [1]

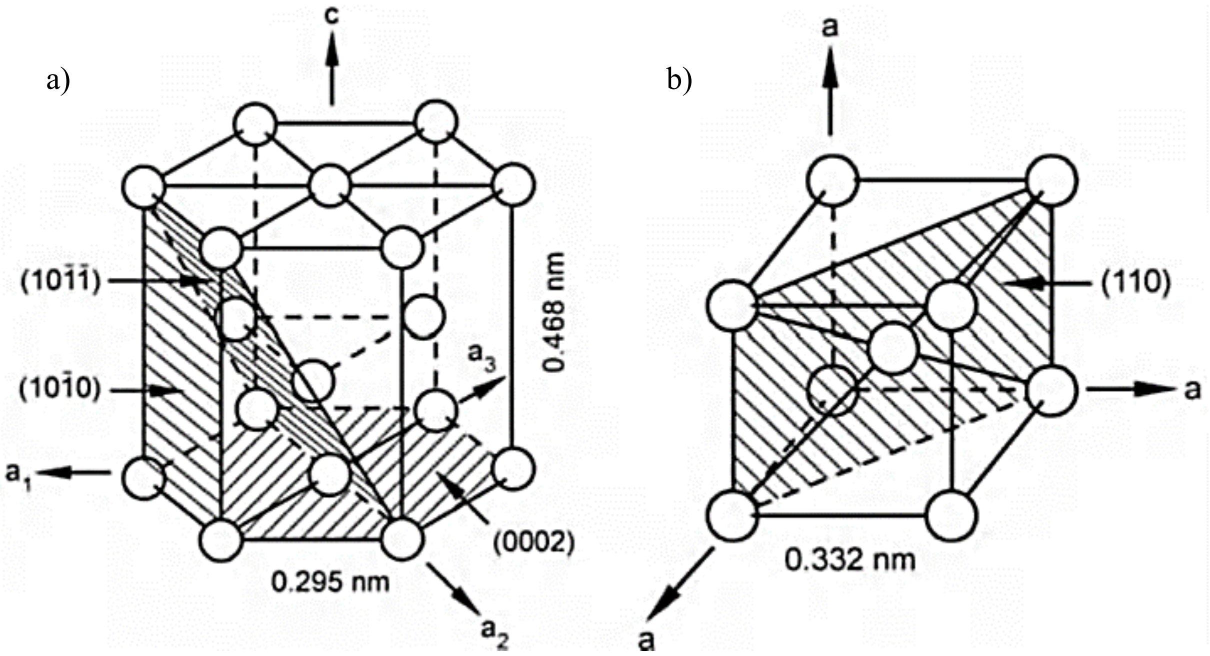

Figure 1: Unit cell of titanium in the two allotropic configurations: a) α phase, b) β phase. [1]

Titanium can be alloyed with other elements to meet a larger variety of material properties. Titanium alloys are categorized in three different groups: α, α+β and β (or near-β) alloys. The α+β alloys are present in a fully lamellar, a fully equiaxed or a bimodal microstructure, this last microstructure containing equiaxed primary α in a lamellar α+β matrix. A fully lamellar microstructure can be obtained by a recrystallization treatment after deformation in the β phase field. The cooling rate from this field determines the characteristics especially of the α phase, like size of colonies and lamellae and the thickness of layers at β grain boundaries. Fully

lamellar microstructures of a different kind can also be generated by skipping the recrystallization step and heat treating the material after the hot deformation in the α+β phase field. For generating a bimodal microstructure, the deformation and recrystallization step are performed below the β transus temperature. A fully equiaxed microstructures can be obtained when the cooling time from the recrystallization step as in the bimodal processing is prolonged, because only recrystallized equiaxed primary α grains will grow. The β phase will remain at the triple-points of the α grains. Another possibility to get fully equiaxed grains is by lowering the recrystallization temperature so that the volume fraction of α is large enough to form the equiaxed grains directly from the deformed lamellae. In this process the α phase separates the final β grains by penetrating through the β/β grain boundaries into the recrystallized lamellae. For Ti64 this recrystallization step can be performed at 800-850 °C and will give smaller α grains (~2 µm) than the method described before. The different microstructures can be transformed into each other by a heat treatment in the designated region (α+β or β) and cooling according to the desired end product. Various parameters during deformation, recrystallization and annealing influence the final microstructure.
For very fast cooling from the β field the material forms martensite. This martensite is a distorted form of the α phase, either α'(hexagonal) for more diluted alloys and α'' (orthorhombic) for alloys with higher solute content. [1]

The different kinds of alloys are obtained by alloying with other elements. Aluminium, an α stabilizer is the most common alloying element for titanium. Its content is limited to 6%, to avoid precipitation of $TiAl_3$. Vanadium is a β stabilizer and results in an isomorphous phase diagram. By addition of ca. 15% V (max. content) the transformation temperature to α is lowered to ~700°C. The solid solubility of vanadium in the α phase is limited to ca. 3% at elevated temperatures.
Considering the physical properties titanium presents some differences compared to Fe, Ni and Al. The linear thermal expansion coefficient for Ti64 is $9.0\ 10^{-6}$ 1/K and its thermal conductivity 7 W/mK, both are lower values than for the other metals. The electrical resistivity is higher than for Fe, Ni and Al, with a value of 1,67 µΩ m for Ti64. [1]

The titanium alloy used for this project is the α+β alloy Ti64 (Ti-6Al-4V) and has an aluminium content of 6 wt% and a vanadium content of 4 wt%. The β-transition temperature is reported to be between 995°C [1] and 1000°C [6].
At 800°C Ti64 contains ca. 15 vol% of β-phase in equilibrium. Apart from pure titanium the alloy is the most frequently used titanium alloy. The success of Ti64 can be traced back to its excellent material properties. It comprises a significant strength at low temperatures, it is suitable for forming and welding and has an enhanced corrosion resistance and stability. [7] Similar to other titanium alloys, literature reports a broad range of elastic moduli for Ti64 varying from 100 to 130 GPa. The value is determined by the specific phases and their volume fraction in the alloy. [8]

2.2.Hot deformation behavior

The broad use of Ti64 gave rise to the application and analysis of different forming processes for this alloy. As cold deformation requires a high load capacity, often hot deformation is preferred, also because more complex shapes can be obtained and formability is enhanced. Hot deformation used for various applications can be simulated via different experiments. Like other mechanical and physical properties also the maximum flow stress of Ti64 depends on the temperature, strain rate and microstructure condition. Figure 2 shows the dependency of this material property for different strain rates and across the β transus temperature. [9]

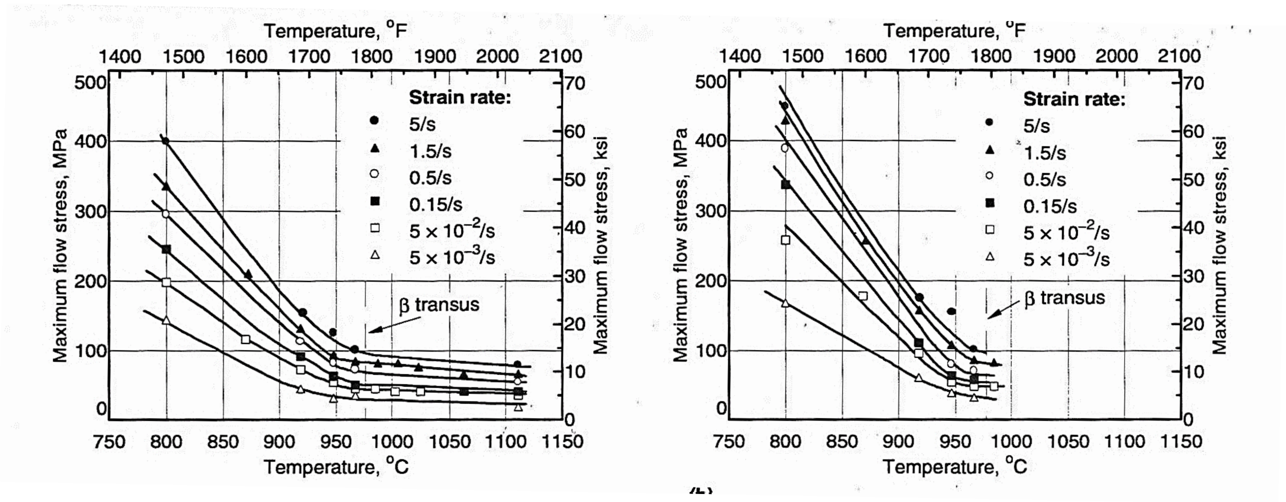

Figure 2: Effect of strain rate and temperature in flow stress. A) equiaxed initial microstructure, b) lamellar initial microstructure. [9]

A common method to simulate hot deformation are hot compression tests. Compression flow curves of Ti64 may show flow softening, where the generation of heat during deformation is one of the causing reasons. For a temperature rise of 19.5°C the flow stress was reported to drop 17% at a temperature of 1100°C in a compression test. This example shows clearly the importance of considering the heating effect when working with experimental flow curves. [10] While compression tests normally give flow curves up to moderate strains, with hot torsion tests also large strains can be reached. Although the analysis of torsion tests is of importance for workability testing, there is relatively small amount of information available in the literature.[11] The data obtained in hot torsion has to be converted to effective stress and strain to give comparable flow curves. Several options are available in the literature to perform this conversion. Fields and Backofen suggest the most widely used method [12], see section 3.2. This method is mostly suited for materials with monotonic behaviour related to strain hardening and therefore has limitations for torque curves with varying characteristics in this sense. Canova et al. [13] and Khoddam and Hudgson [14] suggest alternative methods to convert the torque torsion curves to flow curves of effective stress and strain. The latter describe a method that allows for varying conditions of strain hardening.

If the temperature exceeds roughly half of the melting temperature of the material, the microstructure may evolve during deformation. [2] Different phenomena can take place in a material during hot deformation, namely dynamic recovery and dynamic recrystallization.

Dynamic Recovery

For materials with high stacking fault energy stacking faults are not easily formed and climbing and slipping of dislocations is facilitated. Accordingly, dynamic recovery is a very fast process and especially at high temperatures and low strain rates it is the main restoration phenomenon to occur. In the beginning of deformation, the amount of dislocations increases and they interact with each other, which results in an increase in flow stress. With the dislocation density, also the driving force for dynamic recovery increases and via the rearrangement of dislocations subgrains form. After some time, the rate of dislocation formation and annealing conform, yielding a steady-state for both dislocation density and flow stress. [15]

Dynamic Recrystallization

For materials with a low or medium stacking fault energy dynamic recrystallization will be initiated when a critical amount of deformation is reached. Dynamic recrystallization can be split into a continuous (CDRX) and discontinuous (DDRX) phenomenon, while this terminology only originates from phenomenological observations. Discontinuous dynamic recrystallization starts when a critical amount of deformation is reached. New grains usually originate at existing boundaries. With increasing deformation, the dislocation density in the new grains grows. This decreases the driving force for further growth, as well as the nucleation of new grains at migrating grain boundaries. Characteristics of flow curves showing dynamic recrystallization are a broad peak or several oscillations in the beginning of the flow curve, because several cycles of recrystallization can overlap (one peak) or occur subsequently after one another. A short softening regime follows to the peak stress as well as a steady state. With decreasing stress, the dynamically recrystallized grains grow while the initial grains do not. The driving force for the growth of recrystallized grains is the distribution and density of dislocations. [15]

Apart from the standard discontinuous dynamic recrystallization with clear nucleation and growth stages, under certain conditions dynamic recrystallization may occur with different mechanisms, summarized under the name continuous dynamic recrystallization. The so called geometric dynamic recrystallization (GDRX) occurs for alloys deformed up to large strains. When during deformation the material suffers from a large decrease in cross section (e.g. in compression), the initial microstructure is flattened. While the grains become flatter and flatter with increasing strain, the average subgrain size does not change during hot deformation. The fraction of high angle boundaries will increase until the grains have the size of the former subgrains, see Figure 3. This kind of process was observed e.g. for aluminium alloys. GDRX occurrence depends on the starting grain size and the deformation conditions. For a large Zener-Hollomon parameter Z the subgrain size is small, and therefore GDRX only occurs at very high strains, while for low Z the mechanism starts at lower strains. [15]

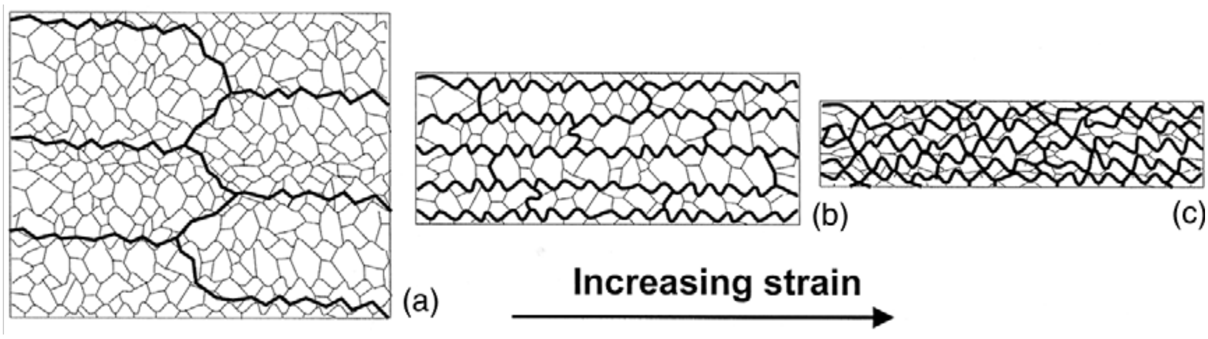

Figure 3: Process of geometric dynamic recrystallization, from a) low deformation to c) high deformations. [15]

Another mechanism for continuous dynamic recrystallization occurs through progressive lattice rotation. With increasing strain, the misorientation at the grain boundaries in pre-existing grains increases, resulting in a progressive rotation of the neighbouring subgrains. The misorientation increases and at a certain critical angle the low angle boundary (LAB) converts to a high angle boundary (HAB), see Figure 4.

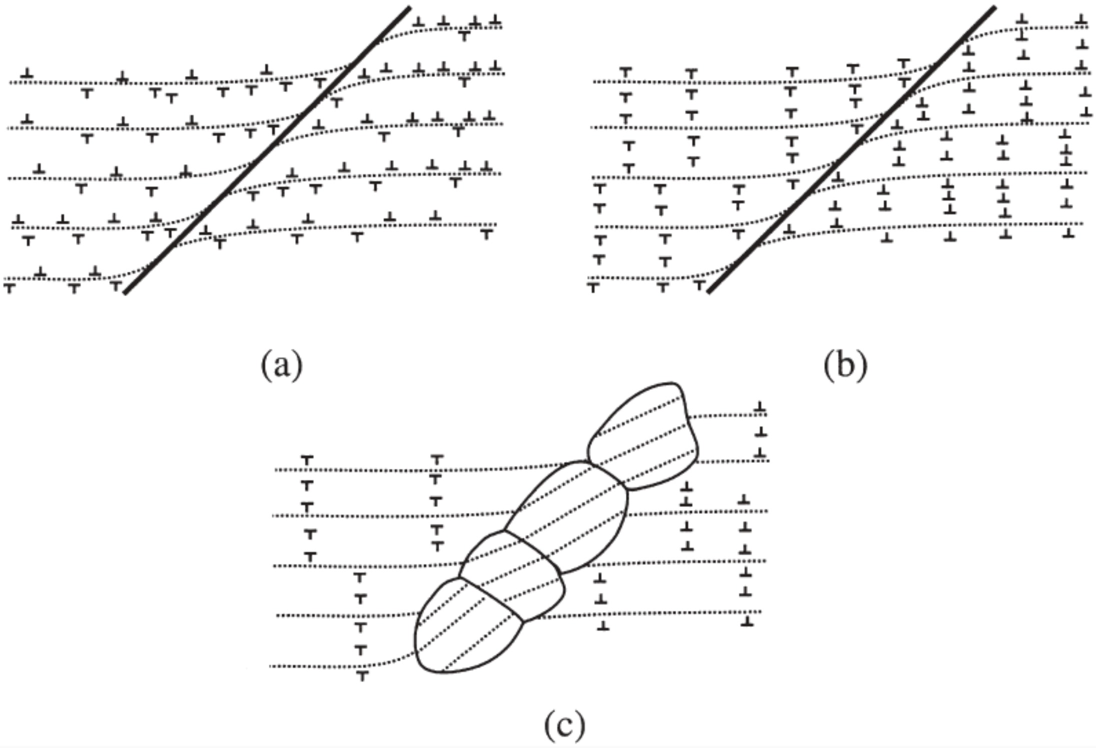

Figure 4: Mechanism of CDRX by progressive lattice rotation. a) local shearing close to grain boundaries, b) geometrically necessary dislocations recover dynamically, c) conclusively formation of new grains and subgrains. [16]

According to Hartherly et al. the mechanism of the progressive subgrain rotation is not yet fully understood. One assumption is that hindered dislocation motion plays an important role, because conventional dynamic recrystallization cannot take place. This can be the case when there is a lack of slip systems like in magnesium alloys or a drag effect from solutes like in Al-Mg-alloys. [15]

Montheillet et al. [17] reported a detailed description of CDRX for materials with high stacking fault energy on the example of Aluminium. Due to the high rate of dynamic recovery in this specific class of materials, dislocations accumulate progressively in low angle boundaries. With further accumulation, the misorientation angle increases and LAB transform into HAB when a critical misorientation is reached. The authors distinguish between different kinds of dislocations to describe the formation and evolution of subgrains. The resulting microstructure therefore contains both LABs and HABs at the limits of grains and subgrains, see Figure 5.

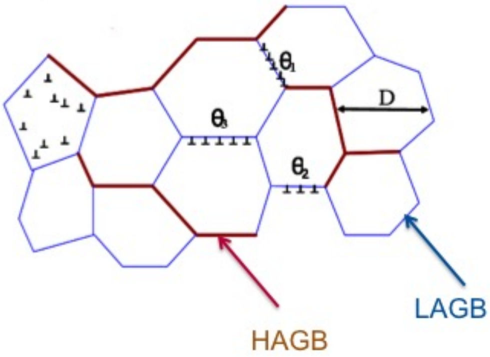

Figure 5: Schematic microstructure formed by CDRX, D is the mean intercept length and θ the misorientation angles of the LABs. [17] edited by Buzolin.

For Ti64 different restoration mechanism have been reported. Porntadawit et al. [2] reported dynamic recrystallization during hot compression at high temperatures in the β and the α+β field, due to the stress-strain curve with a single peak point and recrystallized grains from the β field. Fan et al. [4] argue, that due to high stacking fault energy of bcc crystals the β phase of titanium alloys experiences heavy recovery, which annihilates the majority of dislocations forming during plastic deformation. Poletti et al. [18] report DRV as the only restoration mechanism in the β phase at low and moderate strain rates and DRV followed by CDRX for high strain rate. The authors argue their findings with the formation of new grains by progressive lattice rotation close the former grain boundaries of β phase. The formation of subgrains and subgrain boundaries was revealed by reconstructing the β phase from EBSD data of the quenched martensitic microstructure. The formation of grains as observed in [2] can be attributed to slow quenching rates, as static recrystallization happens within few seconds after deformation in the β phase of Ti64. [19]

2.3. Flow models

In past decades the manufacturing industry relied on empirically designed processes, which consumes both a large amount time and costs. Designing models helps to understand and predict processing-microstructure-property relationships and improve conditions for manufacturing. The development of computer models to correlate processing parameters with mechanical properties and microstructure evolution is therefore an important field of research for titanium alloys. Existing models are able to solve complex tasks from fundamental problems to existing problems in industry. Still, certain phenomena are not fully understood and described, which leads to unforeseeable problems. Microstructure modelling contributes to a holistic understanding of properties and evolution of the microstructure and will also show several benefits in its application, e.g. the improved quality of titanium products. Additionally, modelling attempts for titanium may be used to describe the behaviour of other alloys. [20], [5] Flow modelling at high temperatures in particular can help to better understand required forces for forming, accurate dimensional control of final parts and process simulations for various metals. Especially with the advancing power of computer simulations like the finite element method (FEM), accurate flow stress curves are essential as input parameter to secure the proper simulation of the software. [2]

The definition of a model in science is a theoretical sketch that tries to illustrate complex structures and processes and allows an approximate evaluation of a defined problem. [21]. In terms of flow models, first a constitutive equation to describe the flow stress is required. The modelled flow stress can either depend solely on material and experimental parameters or on one or several internal variables representing the microstructure, such as the grain size or the dislocation density.

From the variety of models predicting deformation behaviour, the models can be classified into two groups: purely phenomenological models and physical-based models. While the former determine material constants from experimental data, the latter work with mechanisms of plastic deformation. Phenomenological models are often inflexible when it comes to different microstructure setting of the tested material, while the structure of physical-based models allows the consideration of these effects. However, also most of the published physical modelling requires parameters, that are fit to experimental flow curves. [3] In physical models the aim is to give a physical meaning also to these fitting parameters.

The two types of modelling will be illustrated by one example for phenomenological modelling and three examples for physical based modelling.

2.3.1. Phenomenological modelling

Khan et al. [22] propose a model for Ti64 for different loading conditions in torsion and compression tests that is based on the Khan–Huang–Liang (KHL) model.[23],[3]

The constitutive equation for the KHL model includes several experimental and material parameters.

$$\sigma = \left[A + B\left(1 - \frac{ln\,\dot{\varepsilon}}{ln\,D_0^p}\right)^{n_1} (\varepsilon^p)^{n_0}\right]\left(\frac{\dot{\varepsilon}}{\dot{\varepsilon}^*}\right)^C \left(\frac{T_m - T}{T_m - T_{ref}}\right)^m \tag*{\textit{eq. 1}}$$

A, B, n_1, n_0, C and *m* are material specific constants, σ, ε^p, $\dot{\varepsilon}$ are the effective stress, effective plastic strain and strain rate, while T_m, T, and T_{ref} mark the melting, current, and reference temperatures. D_0^p is the arbitrarily chosen upper bound strain rate and the normalizing strain rate is $\dot{\varepsilon}^*$. The determination of the material constants is achieved by uniaxial loading test results for different $\dot{\varepsilon}$ and *T*. This first set of constants is refined by using different mathematical approaches to minimize the discrepancies between the actual and the correlated data. The model has the ability to reproduce flow curves of pure torsion and torsion followed by compression from room temperature up to 315°C.

2.3.2. Physical modelling

Model considering one type of dislocation density [24]

The model by Mecking and Kocks was developed in 1981. It is a simple model to describe the flow stress of a material by considering the evolution of the solely internal variable dislocation density ρ, to be given by one hardening and one recovery term. It is valid for a material consisting of just one phase and coarse grains, so the effects of structure are negligible. [25]

The model considers the total stress as function of the dislocation density, giving the following constitutive equation.

$$\sigma = M\alpha Gb\sqrt{\rho} \qquad \textit{eq. 2}$$

M is the Taylor factor and is usually taken as constant value, even though it evolves with straining to account for texture. [25] α is a numerical constant, G is the shear modulus, b is the Burgers vector and ρ is the dislocation density. Kocks also described the evolution of the dislocation density with strain ε in the course of plastic deformation. [26] The expression involves the hardening and recovery coefficients h_1 and h_2, respectively.

$$\frac{\partial\rho}{\partial\varepsilon} = h_1\sqrt{\rho} - h_2\rho \qquad \textit{eq. 3}$$

The dislocation density in this model is considered as an arrangement of isolated dislocations, that are homogenously distributed.

Model considering different types of dislocation densities [27]

Roters, Raabe and Gottstein present a model trying to emphasize recent understanding of the microstructure evolution and interactions of dislocations and other essentials of the microstructure. They distinguish interactions between dislocations and the processes happening between dislocations and precipitates.

The concept includes three internal variables and their evolution. For a metal that forms cells and subgrains during deformation, the cell walls are described as the wall dislocation density ρ_w. Inside the cells there is the immobile dislocation density ρ_i and a so called mobile dislocation density ρ_m that is generated at different sources inside the cells. These mobile dislocations interact with interior and wall dislocations due to their motion caused by proceeding deformation. The formation of dislocation dipoles and the annihilation of mobile dislocations are the described interactions. Dipoles will undergo thermally activated recovery processes as they reach the dislocation walls.

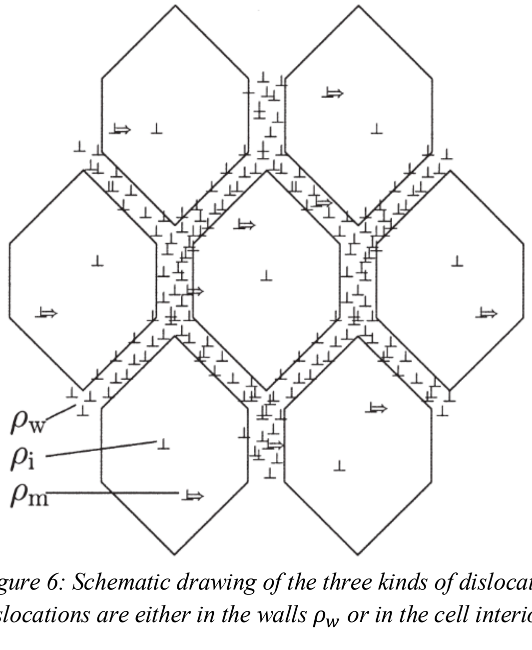

Figure 6: Schematic drawing of the three kinds of dislocation densities. ρ_m are the mobile dislocations, the immobile dislocations are either in the walls ρ_w or in the cell interior ρ_i . [27]

Each category of this dislocations densities follows in their evolution the following rate equation, with $\dot{\rho}_x^+$ representing the production terms of dislocations and $\dot{\rho}_x^-$ the consumption terms.

$$\dot{\rho}_x = \dot{\rho}_x^+ - \dot{\rho}_x^- \qquad \textit{eq. 4}$$

An equation of state represents the flow stress for a set microstructure and temperature. Rotters et al. use the Orowan equation for this matter.

$$\dot{\gamma} = \dot{\varepsilon}M = \rho_m b v \qquad \textit{eq. 5}$$

$\dot{\gamma}$ is the shear rate, $\dot{\varepsilon}$ the strain rate, M the Taylor factor, b the Burgers vector and v the average dislocation glide velocity depending on several material and experimental parameters. For the mobile dislocation density, the Orowan equation is used to get a relation with the imposed strain, as for a certain time increment a certain rate of mobile dislocations density is produced and immobilized after travelling a mean free path. The reduction of mobile dislocation density occurs either by annihilation, or by the formation of dipoles and dislocations locks. For the immobile dislocations in the cell interior the production term corresponds to the reduction term of the mobile dislocation density due to the formation of dislocation locks. The only reduction process for ρ_i is the annihilation caused by dislocation climb, because dislocation locks are not able to glide. Immobile dislocations sitting at the walls experience the same processes as ρ_i. One additional mechanism for ρ_w was found by Kratochvíl et al. [28], who described the accumulation of dipoles at the walls and therefore add another production term for ρ_w. The authors also consider the effects of precipitates present in the investigated Al-alloy. As Ti64 is free of precipitates, this consideration is not further elucidated here.
Adjustment of physical parameters was done using reference ranges from the literature and some fitting with experimental flow curves.

A model of continuous dynamic recrystallization [17]
The model by Gourdet et Montheillet is based on the mechanism of CDRX described in 2.2 . As the model is built for materials with high stacking fault energy, the microstructure is structured both by HABs and LABs. While the dislocation densities within the crystals and the crystallite sizes are quite evenly distributed, the LABs show a continuous range of misorientations. To account for these, three internal variables are defined: the average dislocation density within the crystallites ρ_i, a distribution function of the misorientation angle $\varphi(\theta)$ and the average size of the crystallites *D*, which is an intercept length defined as 2 divided by the total area of boundaries per unit volume. With the integral of the distribution function from the starting misorientation angle to a critical value (where a LAB converts to a HAB) the fraction of LAB can be calculated. The fraction of HAB can be obtained by considering that the fractions of LAB and HAB add to 1. With the fraction of LAB and the distribution function of the misorientation angle, an average misorientation angle is calculated and in the following a LAB dislocation density ρ_{LAB} (corresponds to ρ_m) considering both these charactersitics of LAB.

The evolution of dislocations with strain ε includes a strain hardening and dynamic recovery coefficient h_1 and h_2 as well as the volume *dV* swept by mobile HAB annihilating dislocations.

$$d\rho_i = (h_1 - h_2\rho_i)d\varepsilon - \rho_i dV \qquad \textit{eq. 6}$$

dV is defined as the HAB area per unit volume multiplied with the distance moved during a certain step of deformation. Concerning the decrease of ρ_i, some dislocations form new LAB while the other fraction is absorbed by already existing boundaries. If this absorbing boundary is a LAB the misorientation will change. As a consequence of the deformation, the fraction of high and low angle boundaries will change as well as the distribution of the misorientation and thereby the different dislocation densities. The constitutive equation of this model is a function of ρ_i and ρ_{LAB}.

$$\sigma = Gb(A_1\sqrt{\rho_i} + A_2\sqrt{\rho_{LAB}}) \qquad \textit{eq. 7}$$

σ is the modelled flow stress, b the Burgers vector, A_1 a constant parameter close to unity and A_2 another smaller parameter, because the strengthening efficiency of ρ_{LAB} is less than for ρ_i. The model was successfully applied for aluminium up to strains of 6.

3. Methodology

3.1. Hot compression tests

Compression tests were performed prior to this work at the Institute of Metal Forming at the RWTH in Aachen. Table 1 lists the chemical composition of the used Ti64.

Table 1: Chemical composition of testing material for two performed analyses.

	Al	V	Fe	O_2	C	N_2	H_2	Y
TOP	6.47	3.94	0.18	0.178	0.023	0.003	0.002	<0.001
BOTTOM	6.46	4.05	0.21	0.174	0.022	0.003	0.002	<0.001

The sample geometry was a cylinder with a diameter of 16.0 mm and a height of 24.6 mm. The samples were heated to the test temperature and held for 5 minutes at this temperature before deformation started. The used lubricant was Schmelzglas 8470. Compression tests were performed at six different strain rates at eight different temperatures for strains up to 0.8 in a Servotest machine. The samples were quenched with water after deformation.

Table 2: Experimental matrix of compression tests performed in RWTH Aachen, ✓ marks successful test.

$\dot{\varepsilon}$	800°C	900°C	940°C	970°C	1010°C	1050°C	1100°C	1150°C
0.001 s^{-1}	✓	✓✓	✓✓	✓	✓✓	✓	✓	✓✓
0.1 s^{-1}	✓✓	✓✓	✓✓	✓✓	✓✓	✓✓	✓	✓✓
1 s^{-1}	✓✓	✓✓	✓✓	✓	✓✓	✓✓	✓	✓✓
10 s^{-1}	✓✓	✓✓	✓✓	✓	✓✓	✓✓	✓✓	✓✓
50 s^{-1}	✓✓	✓✓	✓✓	✓✓	✓	✓	✓✓	✓✓
100 s^{-1}	✓✓	✓✓	✓✓	✓✓	✓✓	✓✓	✓✓	✓✓

3.2. Hot torsion tests

A plate of Ti64 with the dimensions 280 x 228 x 15 mm was wire cut to long and narrow bars and then torsion samples were manufactured at the Institute of Production Engineering. 19 samples were generated whereas three of them were cut perpendicular to the other ones. The geometry of the torsion samples can be seen in Figure 7.

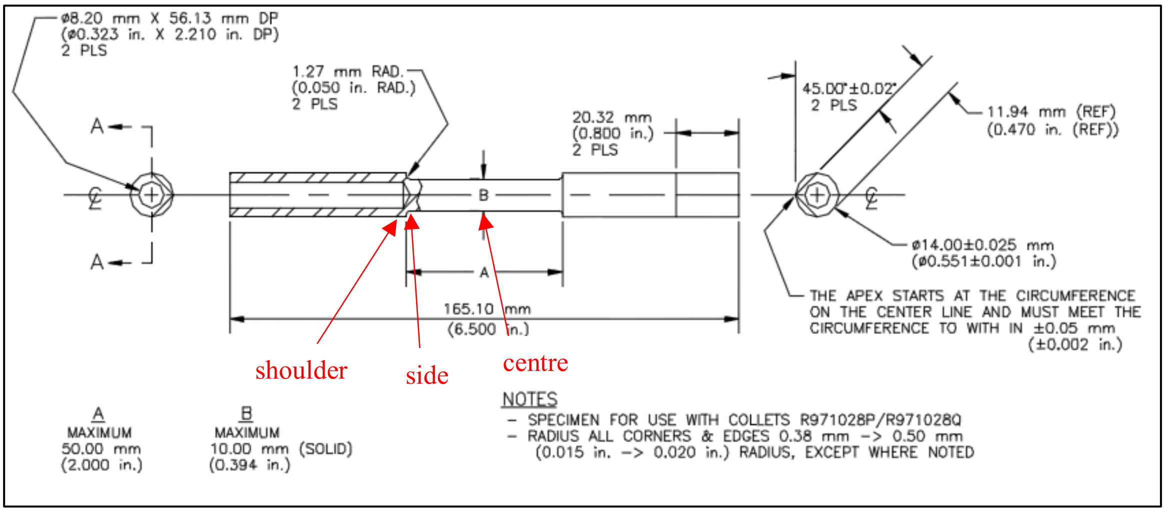

Figure 7: Geometry for torsion samples.[29] A=20 mm, B=10 mm and the drill hole was 67.5 mm.

Hot torsion tests were performed for Ti64 with a Gleeble® 3800. Preliminary tests to determine temperature gradients were performed for one sample of Ti64. The temperature was measured at three points (centre, side and shoulder, see Figure 7) using spot welded thermocouples type K and S. A preliminary temperature program was carried out with three holding points (950°C, 1000°C and 1050°C). The torsion tests were done at five different temperatures in the α+β and the β field and for three different strain rates. The proceeding of each experiment was programmed with the QuickSim software. The experimental matrix can be seen in Table 3.

Table 3: Experimental matrix of performed torsion tests, ✓marks successful test.

$\dot{\varepsilon}$	950°C as received	950°C lamellar	970°C as received	970°C lamellar	1030°C as received	1050°C as received	1070°C as received
0.01 s^{-1}				✓	✓	✓	✓
0.1 s^{-1}	✓	✓	✓	✓	✓	✓	✓
1 s^{-1}		✓		✓	✓	✓	✓

Most experiments were programmed for 8 revolutions, which corresponds to effective strains of 8.1. The samples were heated to the test temperature with a heating rate of 5 K/s and held at the testing temperature for 5 minutes. The torsion tests in the α+β field were performed using two different microstructures. One part was twisted with the as received microstructure following Figure 8. The other part was modified via heat treatment to obtain a lamellar microstructure. For this purpose, the samples were heated in the Gleeble® to 1050°C with 5 K/s and held at this temperature for 10 minutes, then cooled down to the test temperature with 0.66 K/s (40 K/min) and held at that temperature for 5 minutes before torsion started, see Figure 9.

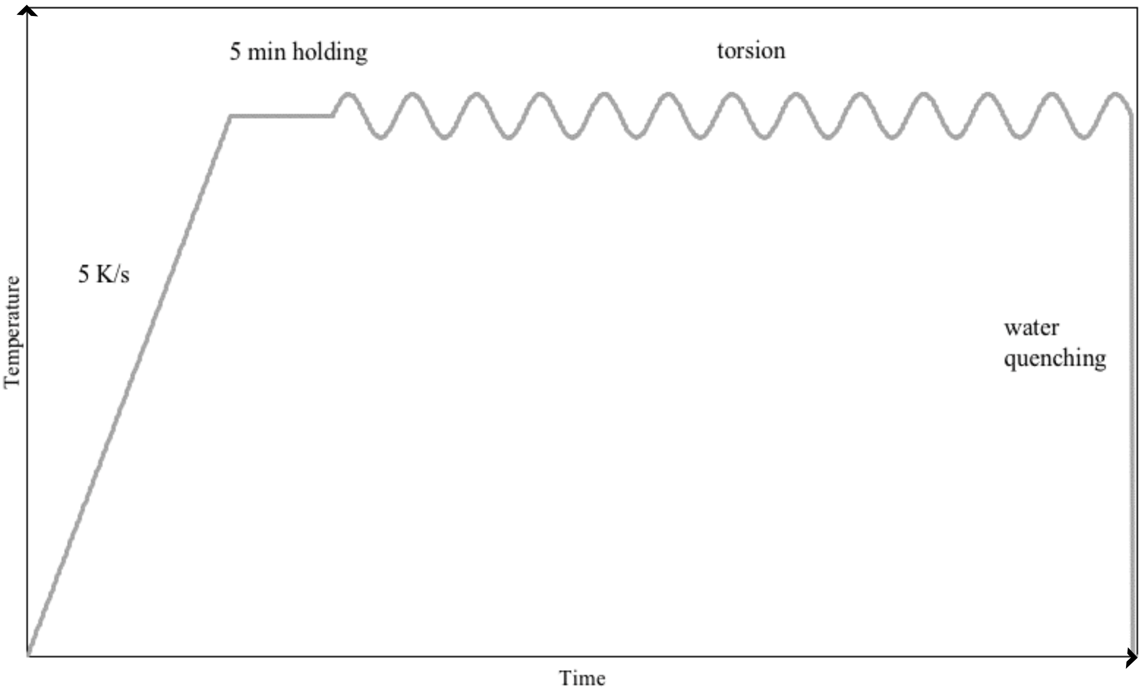

Figure 8: Program for the torsion experiments in the β and α+β field.

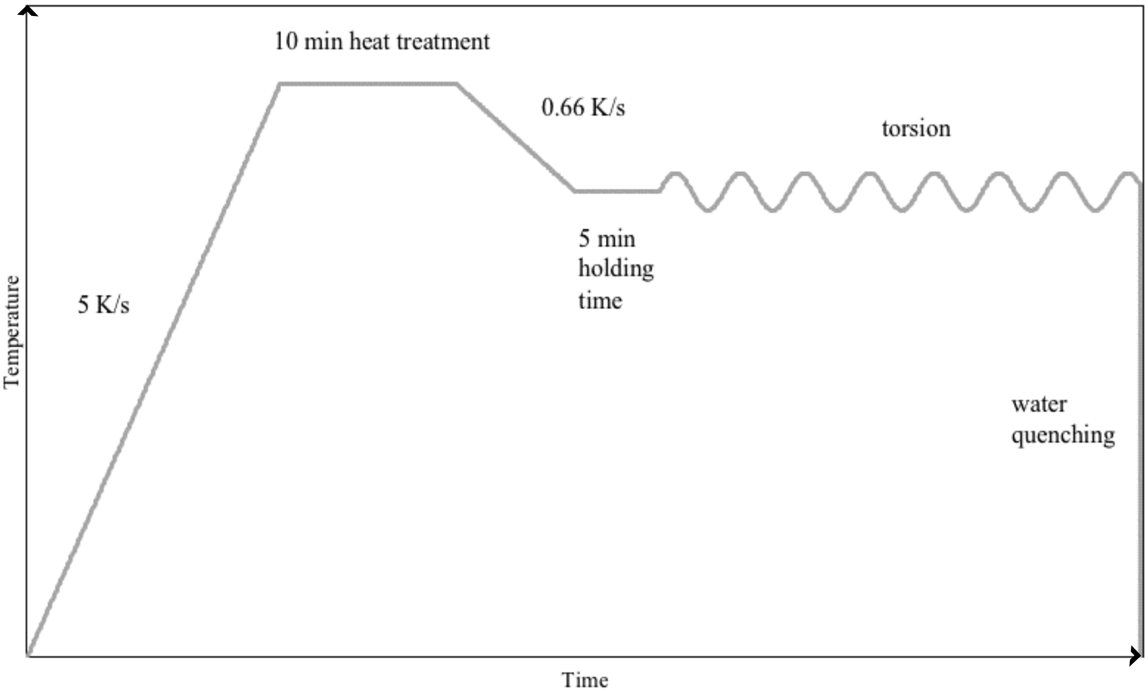

Figure 9: Program for the torsion experiments in the α+β field to obtain an initial lamellar microstructure.

The temperature gradient was estimated along the L-Gauge of the torsion sample using a simple heat increment test. Figure 10 shows the temperature measured at different positions within the sample by thermocouples TC1, TC2 and TC3. While the temperature for the controlling thermocouple TC1 is in good agreement with the programmed temperature (PTemp), the signals given by the thermocouples on the side (TC2) and the shoulder (TC3) are lower and increase during the holding period. The difference in temperature between centre and side of the sample is around 20°C while the difference between the centre and the shoulder is about 50°C. The maximum difference between the thermocouples is 75°C, which was observed in the beginning of the temperature plateaus.

Figure 11 shows the temperature measurement during a torsion test. As the thermocouple in the centre may detach at large deformations and also may hinder the sample movement, the temperature during the torsion tests was controlled using the thermocouple on the side of the L-Gauge (TC1). A second thermocouple (TC2) on the shoulder served as a reference. The difference in temperature between these two thermocouples is about 20°C and stays rather constant also during torsion.

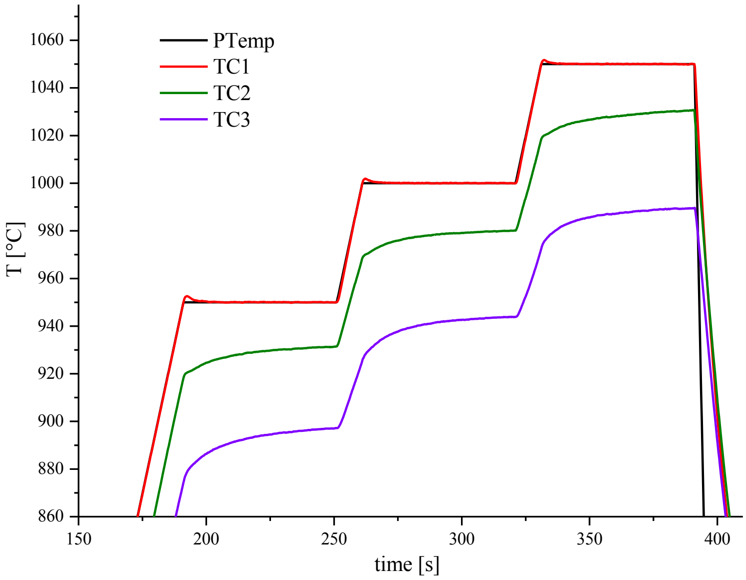

Figure 10: Detail of temperature measurement for heat increment test of Ti64. TC1 was placed in the centre, TC2 on the side and TC3 at the shoulder of the sample. The regulating thermocouple is TC1. The programmed temperature (PTemp) can be seen as a reference.

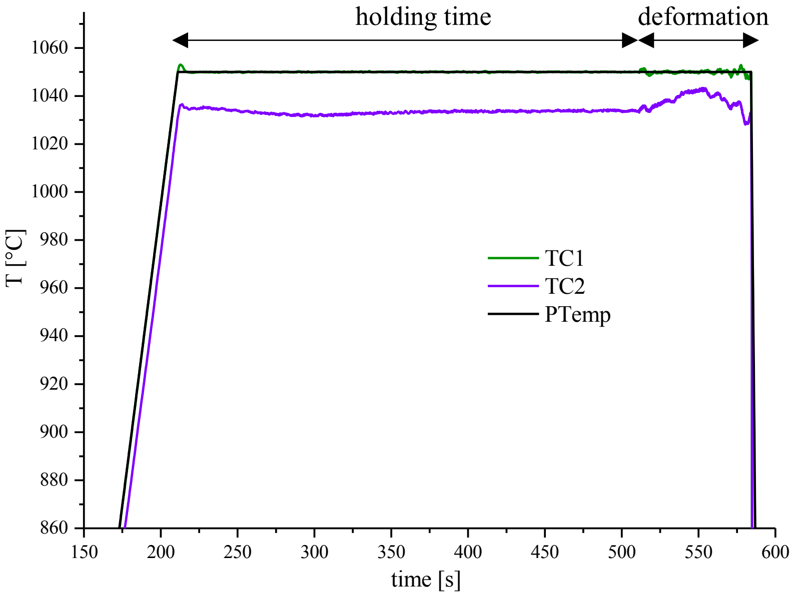

Figure 11: Temperature measurement during a torsion test. TC1 is placed on the side and TC2 at the shoulder of the sample. The regulating thermocouple is TC1. The programmed temperature (PTemp) can be seen as a reference.

Before fastening the sample within the Gleeble® 3800 the two sample holders were controlled for their alignment with a straight piece of metal. The screws of the sample holder were fastened crosswise with a torque meter to 123 pounds inch. Before starting the torsion test, the test chamber was evacuated and flushed with Argon several times to provide an inert atmosphere. During the experiment the chamber was sealed or flushed with a low stream of Argon. After deformation the samples were quenched with water via two H_2O jets (Figure 12). Figure 13 shows one exemplary deformed torsion sample. As the quenching device in the Gleeble® is not ideally aligned to quench the sample equally from two sides, the sample cools down from bottom to top. This results in a different amount of stresses within the sample and causes a bending of the sample, depicted in Figure 13.

A detailed protocol of the performed experiments can be seen in the Appendix on page 75.

Selected torsion samples were investigated via light optical microscopy.

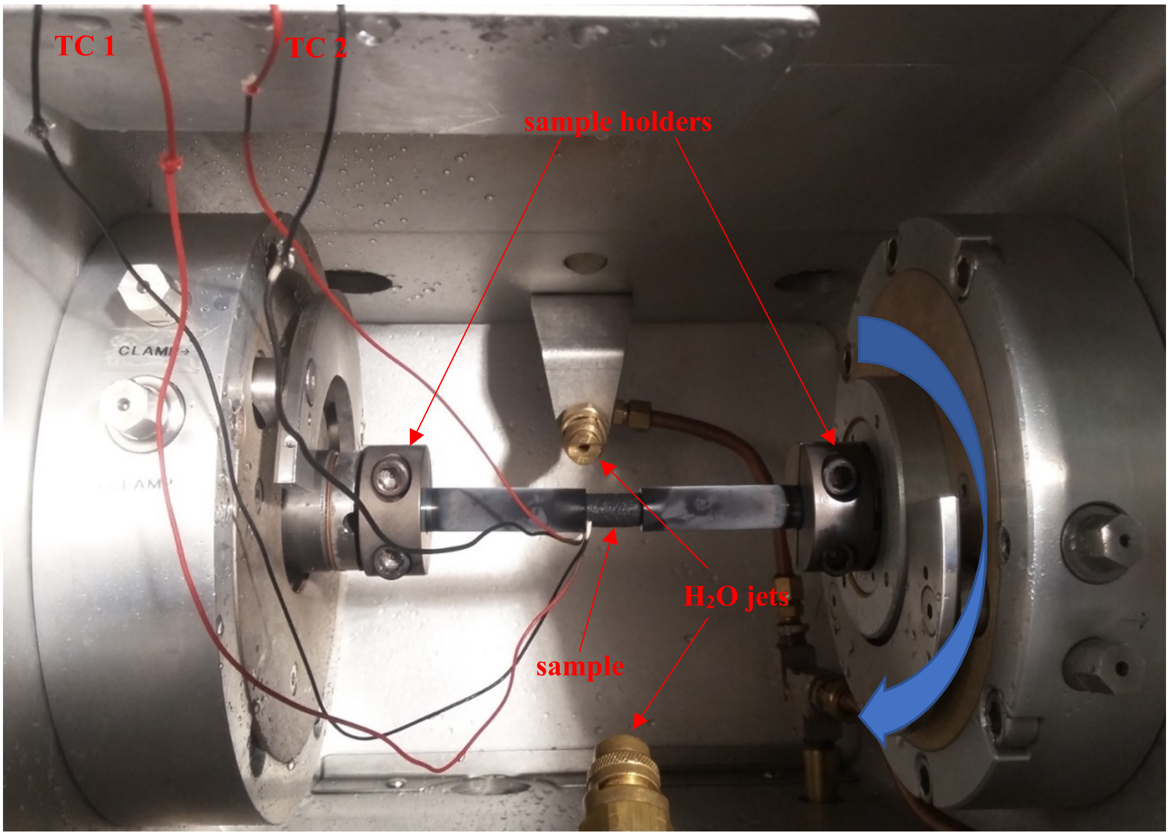

Figure 12: Assembly of torsion sample in the Gleeble® 3800.

Figure 13: Torsion sample deformed at 1070 °C 0.01 1/s strain rate.

3.3. Characterization of base material

The base material plate of Ti64 was completely used for the fabrication of the torsion samples. To get insight into the initial microstructure, a similar plate from the same delivery (Lang GmbH (Ebern) delivery receipt 2017-02-10) was investigated. The plate was cut in small cubes with an edge length of ca. 1 cm. The cubes were heat treated in the β field and cooled with two different cooling rates, to investigate the effects of a heat treatment on the material. The cubes were put in a Nabertherm furnace (30 – 3000°C) at a temperature of 1050°C for 2 minutes and held at 1050°C for 10 and 30 minutes. For each holding time one sample was quenched in water and the other one was allowed to cool down to room temperature within the furnace.
The initial and the heat-treated microstructures were investigated via light optical microscopy.

3.4. Metallography

The deformed or heat treated parts were cut with a Struers Accutom-10 machine and a Silicon Carbide Cut-off Wheel (10S15) to appropriate size and embedded in a Multifast black resin. The grinding and polishing steps are listed in Table 4.

Table 4: Grinding and polsihing steps for metallography preparation of Ti-6Al-4V.

Step	Grinding/Polishing Cloth	Suspension, Lubricant	Time[min]	Force per sample[N]	Rotation setting	Rotations
1	Si-C paper #180	-, H_2O	5	10	co-rotation	300/150
2	Si-C paper #320	-, H_2O	5	10	co-rotation	300/150
3	Si-C paper #500	-, H_2O	5	10	co-rotation	250/150
4	Si-C paper #800	-, H_2O	5	10	co-rotation	250/150
5	Si-C paper #1200	-, H_2O	5	5	co-rotation	250/150
6	Si-C paper #2000	-, H_2O	5	5	co-rotation	200/150
7	MD-Chem	OP-S, -	10	20	counter-rot.	40/150
8	MD-Chem	OP-S, -	5	10	counter-rot.	40/150

The samples were etched with Kroll reagent (91 ml dist. water, 6 ml HNO_3, 3 ml HF) for 8-15 seconds, cleaned with water and ethanol and observed with a Zeiss Axio Observer optical microscope. As α-titanium shows optical anisotropy, polarized light was used to enhance the visibility of certain features of the microstructure, e.g. to distinguish prior β grains that were transformed into martensitic microstructure during water quenching.

3.5. Flow curves: data treatment

3.5.1. Compression flow curves

Several of the compression flow curves were measured twice with the same deformation parameters. Therefore, the average of these curves was calculated. and plotted as a simple curve. Subsequently the curves were interpolated with 50 points from strain 0 to strain 0.8, see Figure 14.

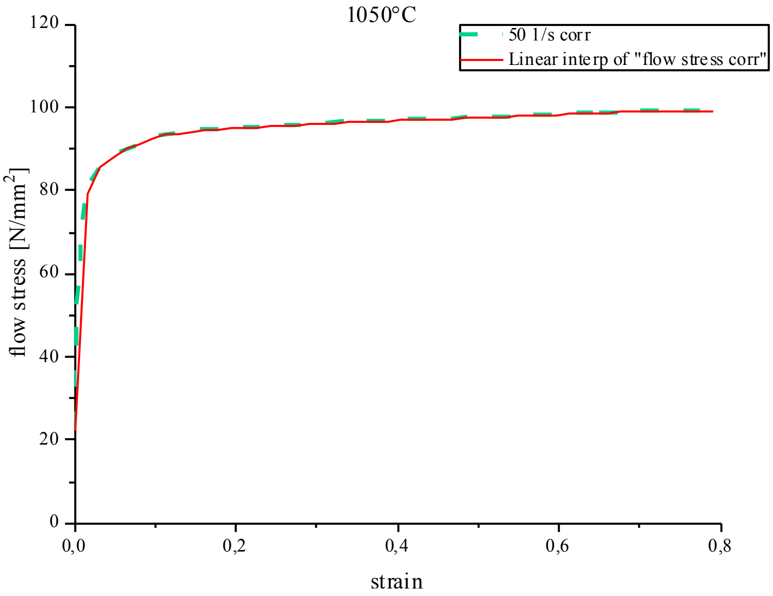

Figure 14: Exemplary interpolation of a compression flow curve.

During the deformation process mechanical energy is converted to heat, rises the temperature and decreases the flow stress for the sample. The corrected flow stress can be calculated with eq. 8, which was successfully used by Kapoor et al. before [30], [31].

$$\sigma_{corr} = \sigma_{meas}(\varepsilon) - \frac{\partial\sigma}{\partial T} I_{\varepsilon,\dot{\varepsilon}}\, \Delta T \qquad \textit{eq. 8}$$

σ_{corr} corresponds to the corrected flow stress, σ_{meas} is the experimentally measured flow stress, $\frac{\partial\sigma}{\partial T}$ is the temperature dependence of the flow stress as a function of strain and strain rate and ΔT is the rise in temperature due to deformation. The temperature dependence of the flow stress was evaluated out of ten stress values ranging from $\varepsilon = 0 - 0.8$ as a function of the temperature, see Figure 15.

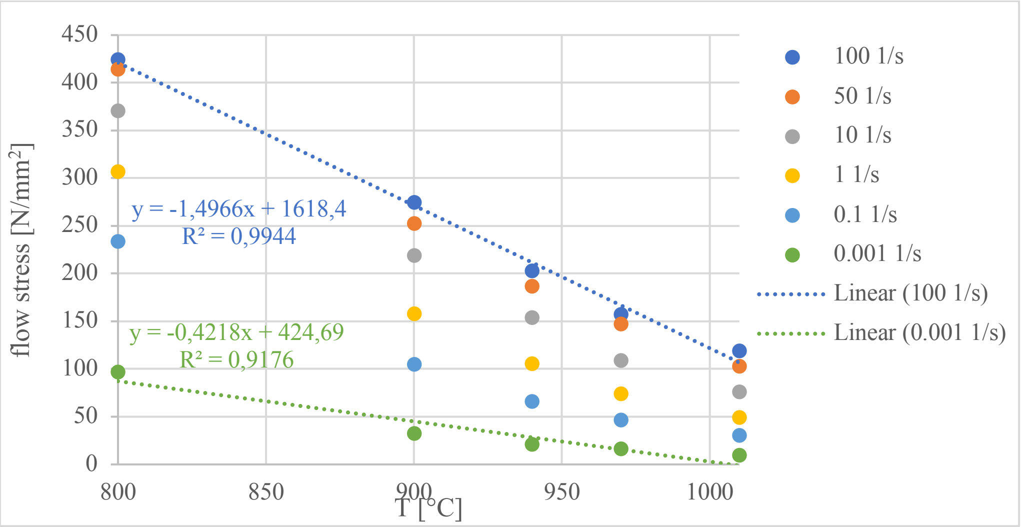

Figure 15: Flow stress versus the temperature for a strain of 0.074 in the α+β field.

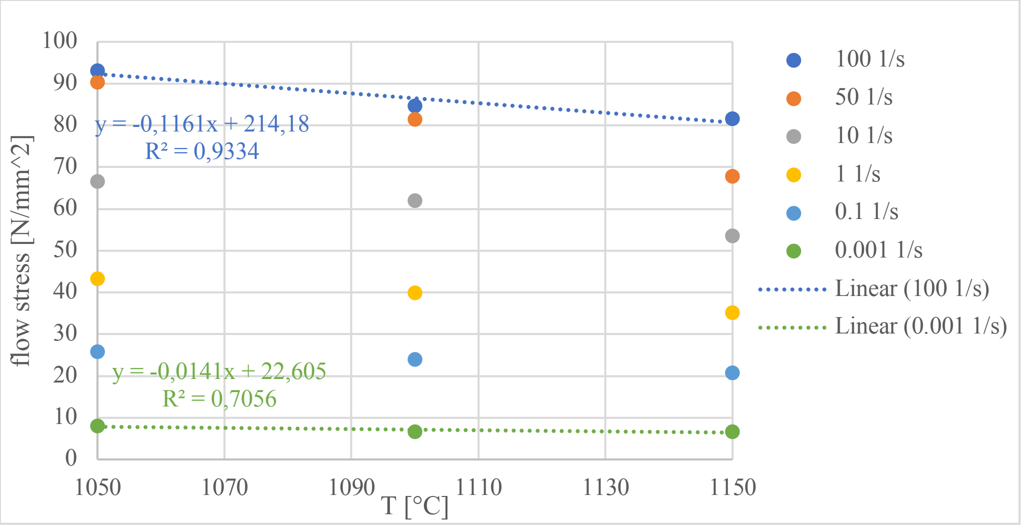

Figure 16: Flow stress versus the temperature for a strain of 0.074 in the β field.

The dependence on temperature showed the influence of strain rate and phase field. Larger slopes were observed for higher strain rates. With respect to the temperature ranges, two slopes were observed: a steeper dependency of the flow stress on the temperature in the α+β field (below 1000°C) and a smaller slope for the β-field, see Figure 15 and Figure 16. The plots of the slope $\frac{\partial\sigma}{\partial T}$ with the strain, shows that $\frac{\partial\sigma}{\partial T}$ values were rather constant, especially for low strain rates, see Figure 17. Therefore, the values were assumed to be constant with strain.

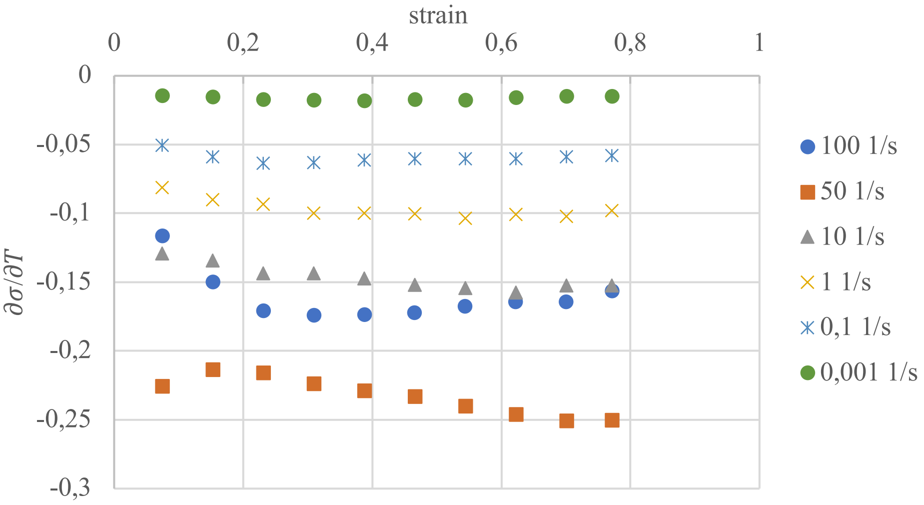

Figure 17: Strain dependency of $\frac{\partial\sigma}{\partial T}$ *in the β field.*

When plotting $\frac{\partial\sigma}{\partial T}$ versus the strain rate a logarithmic law was found. The flow stress dependency with the temperature in the range of 800°C, 900°C, 940°C, 970°C was:

$$\frac{\partial\sigma}{\partial T} = -0.098\ln(\dot{\varepsilon}) - 1.1022 \qquad \textit{eq. 9}$$

and the curves measured at 1010°C, 1050°C, 1100°C and 1150°C with the law.

$$\frac{\partial\sigma}{\partial T} = -0.013\ln(\dot{\varepsilon}) - 0.1019 \qquad \textit{eq. 10}$$

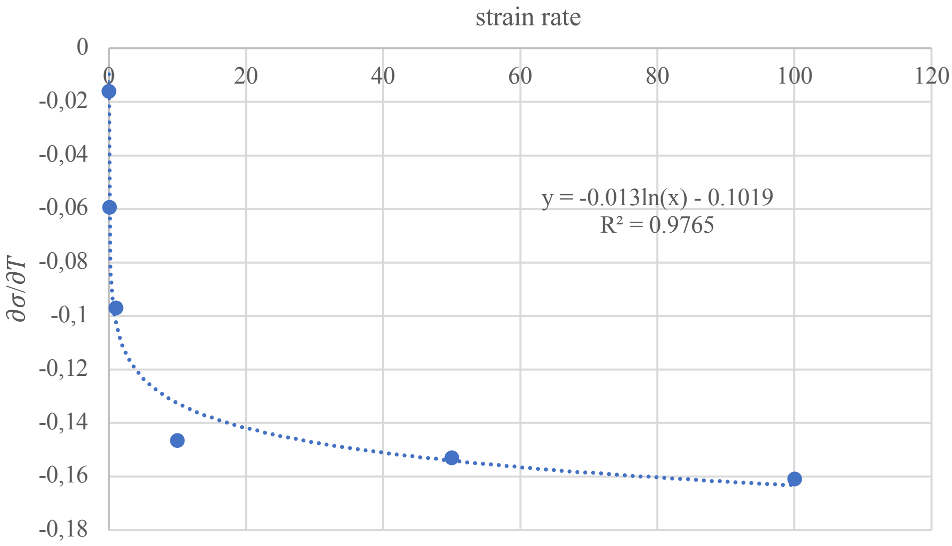

Figure 18: Strain rate dependency of $\frac{\partial\sigma}{\partial T}$ *in the* β *field.*

The increase in temperature was reported by Khan and Liang [23]. Also considering the adiabatic correction factor η like Goetz and Semiatin [32], ΔT can be calculated as the following.

$$\Delta T = \frac{(\eta \; 0.95 \; \int \sigma \, d\varepsilon)}{\delta \; C_p} \qquad \textit{eq. 11}$$

The constant 0.95 corresponds to the amount of mechanical energy converted to heat (varies between 0.9-0.95), δ is the density and C_p the specific heat of the material. The integral represents the area under the uncorrected flow curve. The adiabatic correction factor considers the temperature decrease of the work piece due to heat losses to the dies and the environment. As the temperatures are lower than assumed by complete adiabatic condition, the flow curves corrected by η will be in between the measured curve and the corrected one assuming pure adiabatic condition. η is used between isothermal conditions ($\dot{\varepsilon} \leq 10^{-3} s^{-1}$) where it reaches its minimum 0 and adiabatic condition ($\dot{\varepsilon} \geq 10^{1} s^{-1}$) where $\eta = 1$. For isothermal conditions the generation of heat is quite small due to low strain rate, where the heat can be conducted away from the specimen.

In their investigation Goetz and Semiatin [32] found, that η is not constant with strain but gets lower for higher strains at a given strain rate. They derived an analytical formula for the correction factor.

$$\eta = \left(1 + (h_{all} \Delta\varepsilon) / \left(x_w \delta \; C_p \dot{\varepsilon}\right)\right)^{-1} \qquad \textit{eq. 12}$$

$$h = \left(\frac{x_w}{K_w} + \frac{1}{HTC} + \frac{x_D}{K_D}\right)^{-1} \qquad \textit{eq. 13}$$

Where x_w is half of the workpiece height, K_w and K_D are workpiece and die thermal conductivities, HTC is the interface heat-transfer coefficient, x_D is the distance from the die surface to the die interior and h_{all} marks an overall HTC.

The variables of the equations in the case of hot compression of Ti64 are taken as follows: δ = 4300 kg/m^3 [33], K_w =22 Jm/sK for titanium aluminides and also used for Ti64 [32], HTC for Ti64 at high pressures for coated samples is 3000 W/m^{2}K [34]. In the publication of Semiatin and Goetz [32] $\delta\, C_p$ is taken as a combined parameter, the heat capacity. In their work the thermal properties are dependent on temperature, see Table 5.

Table 5: Thermal properties of Ti64.[32]

T [°C]	$\delta\, C_p$ [kJ/m^{3}K]	K_w [Jm/sK]
800	3.06	25.50
900	3.06	24.41
1000	3.10	23.32
1100	3.50	22.23
1200	4.40	21.14

For the calculations the heat capacity was assumed to be constant until 1000°C and subsequently it follows a polynomial fit, which was the best fit in the regarding temperature range.

The thermal conductivity follows a smooth linear law with temperature, see Figure 19.

$$\delta\, C_p = 2.5 \cdot 10^{-5} \cdot \mathrm{T}^2 - 0.00485 \cdot \mathrm{T} + 26.6 \qquad \textit{eq. 14}$$

$$K_w = -0.0109 \cdot \mathrm{T} + 34.22 \qquad \textit{eq. 15}$$

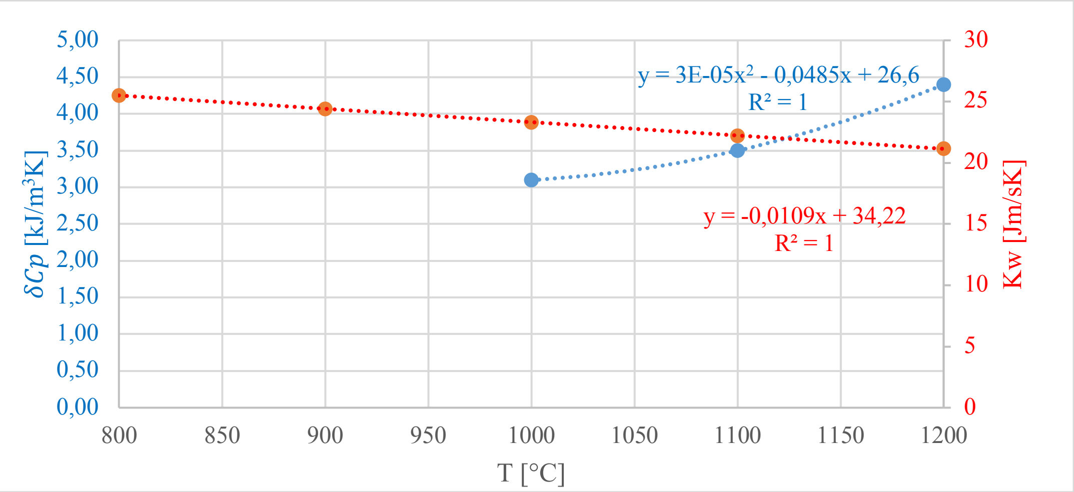

Figure 19: Thermal properties of TiAl, data points taken from [32].

The compression samples had a height of 24.6 mm, so the initial value for x_w is 12.3 mm. As the height of the sample decreases with proceeding compression, the actual x_w was set as the function of the increasing strain $x_w = x_0 \exp(-\Delta\varepsilon)$. The dies for the hot compression test were made of SiN with a cylindrical shape, x_D and K_D were found to be 20 mm and 10 Jm/sK [32], respectively.

3.5.2. Torsion flow curves

The raw data obtained from the hot torsion tests at the Gleeble® is shown in Figure 20.

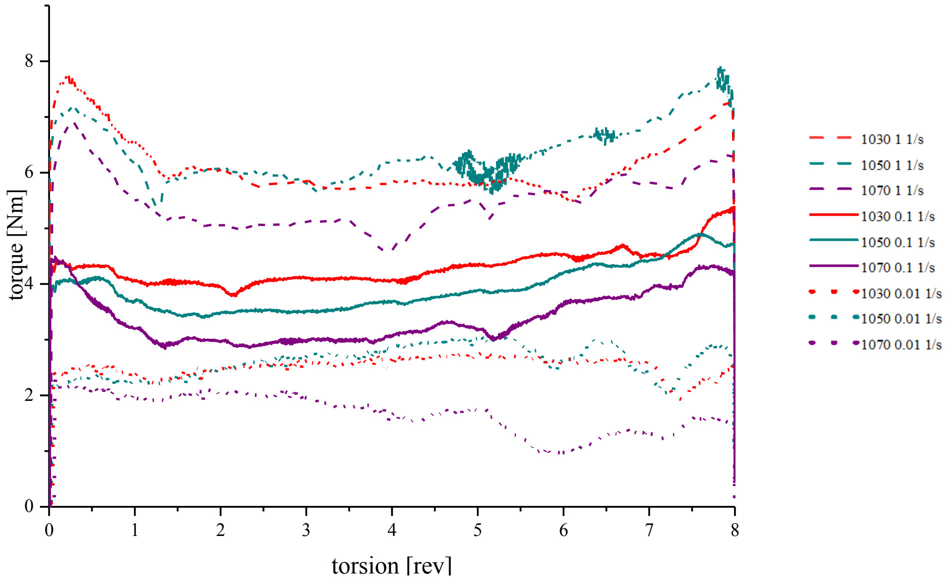

Figure 20: Torque curves measured during hot torsion with the Gleeble® in the β field.

As a first step, the curves were smoothed in the Origin software with the method "Adjacent-Averaging", considering the option for "Weighted Average". The number of measured points considered in the smoothing process (Points of Window) was set to 100 and no boundary condition was chosen. For the flow curves of the material with initial lamellar microstructure the Points of Window were selected as 20, because the shape of these curves was more irregular. None of the characteristics were lost.

The performance of the Gleeble® during operation can be monitored with the signal of the power angle, which indicates the power supplied by the machine. An analysis of the evolution of the Power angle signal (PA) can be an indicator for the validity of the measured curves. If there were strong irregularities in the PA signal, which might also be visible in the flow curve, the curve was cut at the starting point of the irregularity (Figure 21). One problem for these irregularities can be the failure of a thermocouple, which is also visible in the difference in temperature (ΔT) between the two thermocouples (TC1 - TC2).

Table 6 lists the measured flow curves and their validity analysis.

Table 6: Validity analysis of measured flow curves. 'lam' corresponds to initial lamellar microstructure.

$\dot{\varepsilon}$ [s^{-1}]	T [°C]	N_{cut} [rev]	Reason for cutting
0.1	950	8	-
0.1	970	8	-
0.1	950 lam	8	-
1	950 lam	8	-
0.01	970 lam	5.7	Interrupted test, TC2 increases to over 1000°C (failure in contact?) and falls off, PA constant
0.1	970 lam	6	-
1	970 lam	7.5	PA decreases strongly
0.01	1030	6.99	Sudden decrease in σ, TC2 rises over TC1
0.1	1030	6.67	TC1 decreases to 1022°C, σ decreases at this point
1	1030	6.75	Strong decrease in PA
0.01	1050	8	-
0.1	1050	8	-
1	1050	6.86	Strong decrease in PA
0,01	1070	8	-
0,1	1070	8	-
1	1070	8	-

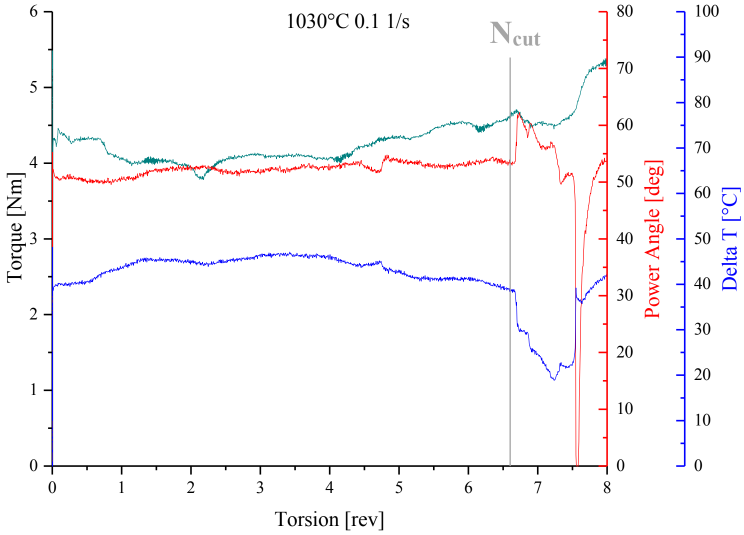

Figure 21: Exemplary validity analysis by monitoring of ΔT and PA signal for torque curve 1030°C 0.1 1/s. Delta T is the difference in temperature between the two thermocouples (TC1-TC2). The point of cutting is marked (N_{cut}).

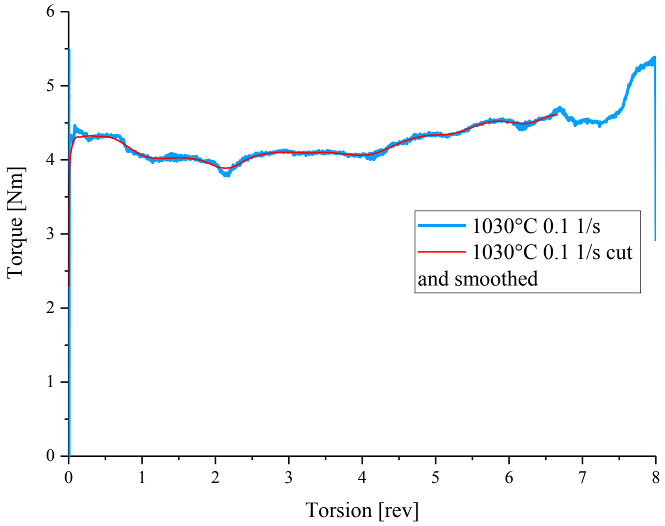

Figure 22: Exemplary data treatment: cutting and smoothing of torque curve 1030°C and 0.1 1/s from a hot torsion test.

Several options are available in the literature to convert hot torsion data into flow curves. Fields and Backofen suggest the most widely used method [12].

The effective strain ε_{eff} and effective stress σ_{eff} can be calculated as the following.

$$\varepsilon_{eff} = \frac{N\,2\pi\,r}{\sqrt{3}\,l} \qquad \textit{eq. 16}$$

$$\sigma_{eff}[N/mm^2] = \frac{M_{Torque}\,\sqrt{3}\,1000\,(3+n+m)}{2\pi\,r^3} \qquad \textit{eq. 17}$$

N is the number of torsion revolutions in the torsion experiment, r and l the outer radius and length of the sample respectively, M_{Torque} is the measured torque in Nm, n is the experimental hardening coefficient and m is the strain rate sensitivity. These last two coefficients are defined in eq. 18 and eq. 19.

$$n = \frac{\delta \ln \sigma_{eff}}{\delta \ln \varepsilon_{eff}} \qquad \textit{eq. 18}$$

$$m = \frac{\delta \ln \sigma_{eff}}{\delta \ln \dot{\varepsilon}} \qquad \textit{eq. 19}$$

m was calculated in an iteration process. As initial value m was set to 0.09992, a value obtained from the applied Kocks Mecking model, see section 3.6.1. In a next step $\ln \sigma_{eff}$ was plotted versus $\ln \dot{\varepsilon}$ for five different strains.

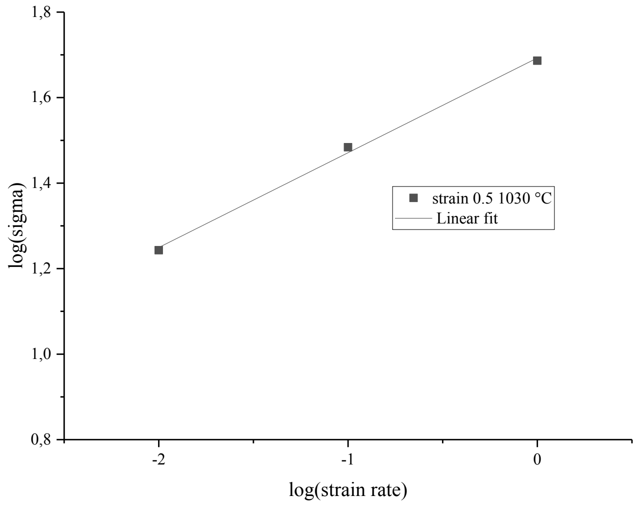

Figure 23: Exemplary derivation of m for a strain of 0.5 and 1030°C.

For different temperatures at one defined strain there was no visible correlation between m and the temperature. Nevertheless, m decreased for revolutions around 3 and increased again for larger revolutions. Therefore, m was plotted versus N and a polynomial law of second order for m as a function of N could be derived.

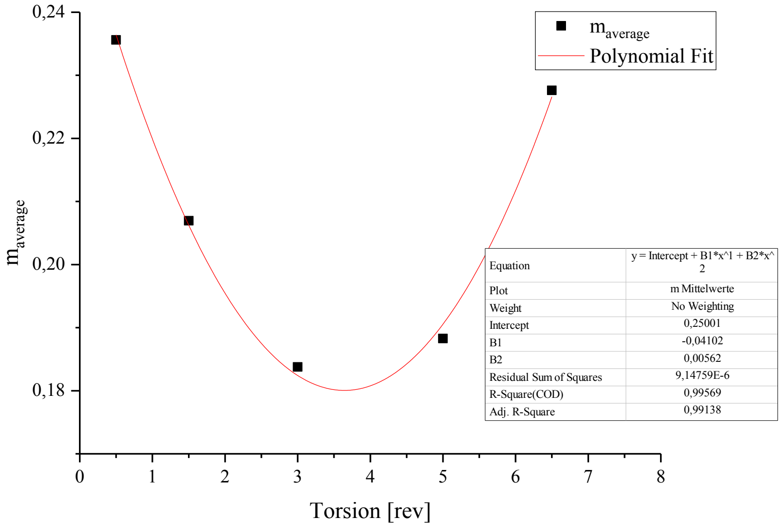

Figure 24: Polynomial law for strain rate sensitivity m as a function of N.

This function was used to calculate new m values and in the following new flow curves. Using these new flow curves a new function for m was obtained. As there was only a slight change in m, the iteration process was stopped at this point.

Table 7: Iteration process for strain rate sensitivity m.

$m = a + b \cdot N + c \cdot N^2$			
a_0	b_0	c_0	**α+β**
0,23015	-0,04291	0,00466	
a_2	b_2	c_2	
0,23015	-0,04291	0,00467	
a_3	b_3	c_3	
0,23015	-0,04291	0,00467	
a	b	c	**β**
0,25576	-0,04156	0,0057	
a_2	b_2	c_2	
0,24773	-0,04118	0,00656	

For the strain hardening coefficient n, an initial value of 0.2 was set according to Lee et al. [35]. In the following, a method from previous calculations (to be published work of Thierry Simonet-Fotso) was adapted. Before calculation of the derivative of $\ln \sigma_{eff}$ with respect to $\ln \varepsilon_{eff}$ the experimental curves were fitted with an exponential function of 5th order.

$$\begin{aligned} y = a_0 + a_1 \exp(-c_1\, x^{m_1}) + a_2 \exp(-c_2\, x^{m_2}) + a_3 \exp(-c_3\, x^{m_3}) \\ + a_4 \exp\,(-c_4\, x^{m_4}) + a_5 \exp\,(-c_5\, x^{m_5}) \end{aligned}$$

eq. 20

The initial set for the fitting parameters is listed in Table 8.

Table 8: Initial parameter set for exponential fitting function for the calculation of n.

-0.0134	-11.7593	2.58309	0.87999	12.69433	0.72401	0.43154	5.80441
a_0	a_1	c_1	m_1	a_2	c_2	m_2	a_3
3.31388	1.04798	-1.0366	0.07404	3.29052	-0.34244	7.87E-05	6.90532
c_3	m_3	a_4	c_4	m_4	a_5	c_5	m_5

The fitting of parameters for each curve was continued in Origin until the fit met the characteristics of the experimental curve to a satisfying level. The derivation of this function with strain was used as n for converting the measured torsion signals to flow curves. For n no iteration steps were done, because the range of the parameter value stayed the same and small fluctuations in the stress values would be amplified by the derivative of the second iteration. An example of the process is illustrated in Figure 25.

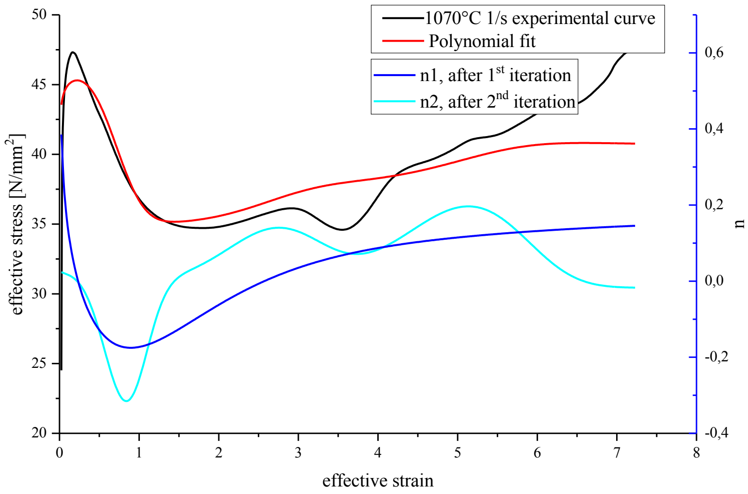

Figure 25: Exemplary illustration for the calculation of the strain hardening coefficient n. n1 and n2 mark the strain hardening coefficient after first and second iteration step.

n in the α+β field is only considered for the two samples with globular structure. In both cases the derivative of $\frac{\delta \ln \sigma}{\delta \ln \varepsilon}$ was calculated. Initial very high values were set to a more reasonable and moderate value from later on in the process and n was set to zero after the first softening. For the lamellar samples n was set to zero, because the irregularities of the flow curves hinder an accurate derivation of n.

During the torsion experiment one end of the sample is free to elongate or as in the present case to shorten in the process of deformation. This resulted in an increase of the L-Gauge diameter. To account for this effect the diameter of the deformed samples was measured. As the lamellar samples were too irregular in shape, the diameter values for the corresponding globular experiments were taken. If there was no equivalent globular sample, diameter values for the 1030 °C samples were taken. A linear evolution of strain was considered from the initial undeformed to the final deformed diameter for each sample. This formula was used as the actual radius for the calculation of the effective strain and stress. The process is shown in Figure 26 for one flow curve.

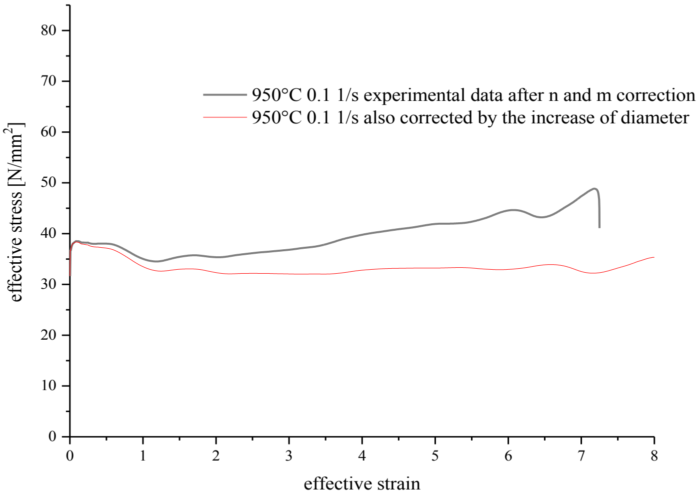

Figure 26: Exemplary flow curve at 950°C 0.1 1/s with and without correction of the diameter increment.

3.6. Flow stress and microstructure modelling

3.6.1. Kocks Mecking Model

To work with the simple model by Mecking and Kocks [24] the equation for the evolution of the dislocation density was integrated to get an expression for the dislocation density as a function of the strain ε.

$$\int_{\rho_0}^{\rho} \frac{1}{h_1\sqrt{\rho}-h_2\rho}\,\partial\rho = \int_{\varepsilon_0}^{\varepsilon} \partial\varepsilon \qquad \textit{eq. 21}$$

ε_0 … initial strain
ρ_0 … initial dislocation density
h_1 … hardening coefficient
h_2 … recovery coefficient

The lower and upper limits for the integral are the initial and actual dislocation densities and strains, respectively. The substitution method with $x = h_1 - h_2\sqrt{\rho}$ was used to solve the definite integral.

$$-\frac{2}{h_2}\, ln\left(\frac{h_1-h_2\sqrt{\rho}}{h_1-h_2\sqrt{\rho_0}}\right) = \varepsilon - \varepsilon_0 \qquad \textit{eq. 22}$$

Considering $\varepsilon_0 = 0$ and reformulating eq. 22, gave the following expression for the square root of the dislocation density.

$$\sqrt{\rho} = \frac{h_1}{h_2}\left(1 - \exp\left(-\varepsilon\,\frac{h_2}{2}\right)\left(1 - \frac{h_2}{h_1}\sqrt{\rho_0}\right)\right) \qquad \textit{eq. 23}$$

The initial dislocation density can be derived from the experimental yield stress σ_{YS} according to the following expression.

$$\sqrt{\rho_0} = \frac{\sigma_{YS}}{M\alpha Gb} \qquad \textit{eq. 24}$$

M … average Taylor factor
α … numerical constant
G … shear modulus
b … Burgers vector
σ_{YS}… measured yield stress

The modelled flow stress can be written as the following.

$$\sigma = M\alpha Gb\sqrt{\rho} \qquad \textit{eq. 25}$$

For $\varepsilon = 0$ the modelled stress equals the yield stress.

$$\sigma = M\alpha Gb\sqrt{\rho_0} = \sigma_{YS} \qquad \textit{eq. 26}$$

For large strains ($\varepsilon \rightarrow \infty$) the modelled stress saturates according to eq. 27. [36]

$$\sigma_\infty = M\alpha Gb\frac{h_1}{h_2} \qquad \textit{eq. 27}$$

The general expression for the modelled stress can be written as follows:

$$\sigma = M\alpha Gb\frac{h_1}{h_2}\left(1 - \exp\left(-\varepsilon\,\frac{h_2}{2}\right)\left(1 - \frac{h_2}{h_1}\frac{\sigma_{YS}}{M\alpha Gb}\right)\right) \qquad \textit{eq. 28}$$

The hardening and the recovery coefficient h_1 and h_2 were used as modified phenomenological functions of the temperature T and the strain rate $\dot{\varepsilon}$ like suggested by Kocks and Mecking. They are also a function of the strain rate sensitivity m and an apparent activation energy Q.

$$h_1 = h_{0,1}\,\dot{\varepsilon}^{m_{h_1}}\exp\left(\frac{m_{h_1}Q_{h_1}}{RT}\right) \qquad \textit{eq. 29}$$

$$h_2 = h_{0,2}\,\dot{\varepsilon}^{-m_{h_2}}\exp\left(-\frac{m_{h_2}Q_{h_2}}{RT}\right) \qquad \textit{eq. 30}$$

Table 9 lists all the parameters needed to set up the Kocks Mecking model for the Ti64 alloy.

Table 9: Parameters for setting up the Kocks Mecking model.

Parameter	Symbol	Value	Value taken from
initial value hardening coefficient	$h_{1,0}$	$8.08\cdot10^{7}$ m^{-1}	fitting
initial value recovery coefficient	$h_{2,0}$	469	fitting
strain rate sensitivity for h_1	m_{h_1}	0.09	fitting
strain rate sensitivity for h_2	m_{h_2}	0.1089	fitting
activation energy for h_1	Q_{h_1}	$2.38\cdot10^{5}$ J/mol	fitting
activation energy for h_2	Q_{h_2}	$1.42\cdot10^{5}$ J/mol	fitting
Taylor factor	M	3.1	literature [37]
numerical constant	α	0.1	fitting of CDRX model
burgers vector	b	$2.86\cdot10^{-10}$ m	literature [1], [38]
universal gas constant	R	8.314 J/mol K	literature [39]
shear modulus	G	function of T	calculated from JMatPro® simulation
initial dislocation density	ρ_0	depending on $\dot{\varepsilon}$	experimental yield stress

Apart from the fitting parameters in the expression for h_1 and h_2 , the other parameters are calculated or taken from the literature.

The software JMatPro® can be used to predict different material properties also for alloys with phase transformations.[40] For calculating the shear modulus the Young's modulus relationship with the Poisson ratio was used. Both Young's modulus relationship and the Poisson ratio were simulated with JMatPro® and approached with a linear function of the temperature. Accordingly, the shear modulus was inserted into the model as the following function.

$$G\ [MPa] = 1000 * \frac{43.60957 - 0.01762 * \mathrm{T}[°\mathrm{C}]}{2.6821 + 7.53004 \cdot 10^{-5} * \mathrm{T}[°\mathrm{C}]} \qquad eq.\ 31$$

The evaluation of the modelled flow curves was done using the root mean square error (RMSE). RMSE is the standard deviation of the residuals, hence the prediction errors. In this case the residuals are the difference between the experimental and the modelled flow stress values. [41] This method was used successfully in other flow stress models of Ti64 before. [2]

$$RMSE = \sqrt{\frac{1}{N} \sum_{\varepsilon}^{N} (\sigma_{meas} - \sigma_{mod})^2} \qquad eq.\ 32$$

The RMSE was calculated for each flow curve and the total sum of all RSMEs was minimized with the "Solver" function of Excel by simultaneous changing of all the fitting parameters.

3.6.2. Model of Continuous Dynamic Recrystallization (CDRX)

The model for continuous dynamic recrystallization is based on the work of Montheillet et al. [17], Poletti et al. [42] and the unpublished works of Simonet-Fotso et al. and Buzolin (IMAT PhD candidates).

The input variables of the model are the temperature, strain rate and average grain size of the microstructure in the β field. The microstructure in the model is constituted by the average grain size, the average subgrainsize, the fraction of high and low angle boundaries (LAB and HAB), the mobile, the immobile and the wall dislocation densities.

The model needs the β grain size in the β-field just before deformation as input. In the dissertation of P. Homporova [43] the grain size in the β field of Ti64 is measured at 1030°C, 1050°C and 1070°C for different holding times. As there was no data for 5 minutes holding time available, an average of the grain sizes from 2 and 10 minutes holding time was calculated and as a linear fit set as initial grain size in the model.

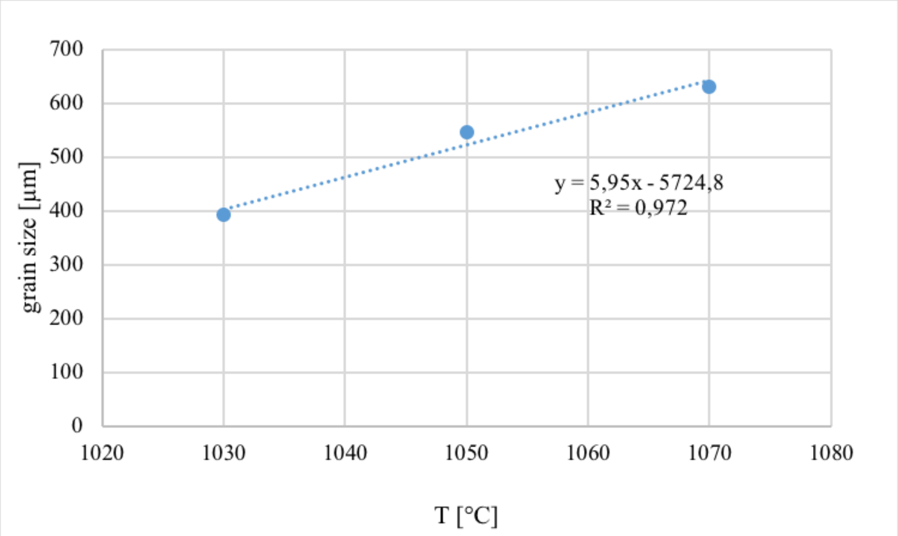

Figure 27: Average grain size for 5 minutes holding time obtained from linear fit.

The average subgrainsize in the starting condition is set equal to the average grain size, since the material is considered to be recrystallized. For the immobile dislocation density ρ_i the initial value was chosen as 10^8 m/m^3 and for the mobile dislocation density ρ_m $2 \cdot 10^{13}$ m/m^3, according to the previous work done on the model by Buzolin. The wall dislocation density ρ_w is calculated in the model according to Montheillet [17].

$$\rho_w = \frac{n_w S_V \bar{\theta} f_{LAB}}{b} \qquad \textit{eq. 33}$$

where $n_w$is the set of dislocations considered to form a LAB, S_V is the total area of boundaries per unit volume [1/m], $\bar{\theta}$ is the average misorientation angle and b is the Burger's vector [m]. f_{LAB} is the fraction of low angle boundaries calculated according to the following equation.

$$f_{LAB} = \int_{\theta_0}^{\theta_c} \varphi(\bar{\theta}, \varepsilon) d\theta \qquad \textit{eq. 34}$$

$\varphi(\bar{\theta}, \varepsilon)$ is the distribution function of the low angle boundary misorientation, θ_0 is the lower limit of the misorientation angle, chosen to be 0.15°, and θ_c is the critical misorientation angle, where a low angle grain boundary converts into a high angle grain boundary. The critical misorientation angle was set to 12°.

The constitutive equation summarizes the different stress components described in the model. The thermal stress σ_{th}, the athermal stress σ_{ath} and the Hall-Petch stress σ_{HP} contribute to the total flow stress according to the following equation.

$$\sigma = \sigma_{th} + \sigma_{ath} + \sigma_{HP} \qquad \textit{eq. 35}$$

The Hall-Petch contribution to the stress considers the influence of both grain size and subgrain size. The regarding shear stress contribution is calculated with the Hall-Petch constant K_{HAB} [44] and the corresponding constant for LAB is calculated with the critical misorientation angle θ_c as $K_{LAB} = K_{HAB}/\sqrt{\theta_c}$.

The shear stress can be derived from the Hall-Petch constants, the area fraction of the boundaries S_V and the average misorientation angle $\bar{\theta}$.

$$\tau_{HP_{LAB}} = K_{LAB}\sqrt{S_{V_{LAB}}\bar{\theta}} \qquad \textit{eq. 36}$$

$$\tau_{HP_{HAB}} = K_{HAB}\sqrt{S_{V_{HAB}}} \qquad \textit{eq. 37}$$

$$\tau_{HP} = \tau_{HP_{HAB}} + \tau_{HP_{LAB}} \qquad \textit{eq. 38}$$

The shear stress is converted to flow stress via the Taylor factor *M*.
The athermal shear stress τ_{ath} accounts for the slide of dislocations and is calculated according to a Kock Mecking equation [24].

$$\tau_{ath} = \alpha\mu b\sqrt{\rho_i + \rho_m + f_{\rho_w}\,\rho_w} \qquad \textit{eq. 39}$$

Contributions to the shear stress by the different dislocation types is shown in eq. 39. Since the strain fields produced by low energy arrangements, such as LAB, is smaller than for isolated dislocations (Figure 28), the wall dislocation density is added with a correction factor f_{ρ_w}.

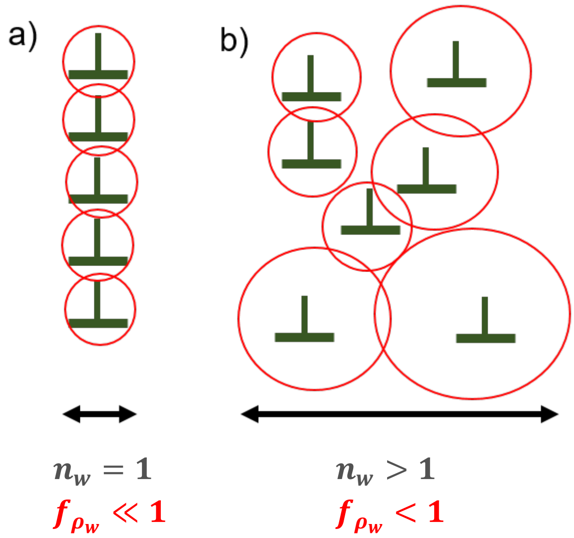

Figure 28: Arrangement of wall dislocations, a) ideally in a sharp subgrain boundary: n_w accounting for width of boundary equal to 1, and f_{ρ_w} (factor of size of strain field) with respect to isolated dislocations much smaller than 1, b) annihilation within boundaries is not promoted as for high strain rates: n_w larger than 1, and f_{ρ_w} a distribution of strain field sizes.

The thermal stress σ_{th} represents the contribution of dislocations sliding. This stress is an output parameter and is calculated from the other stress contributions including the yield stress σ_{YS} .

$$\sigma_{th} = \sigma_{YS} - \sigma_{ath} - \sigma_{HP} \qquad \textit{eq. 40}$$

The yield stress was fitted to find a correspondence for the experimental values from the compression curves and the strain rate. Linear fits between $ln\,\sigma_{YS}$ and $ln\dot{\varepsilon}$ as used by M. Semblanet [45] for Ti alloys before, show the best correlation according to root mean square error evaluation, see Table 10, Figure 29, Figure 30 and Figure 31. The power law relationship between the stress and the strain rate of a material is widely used [46] and was well described by N. J. Hoff in the example for creep. [47]

Table 10: Evaluation of different fits between yield stress and strain rate via root mean square error (RMSE).

	linear fit				**polynomial fit**				**power law fit**			
	T [°C]				T [°C]				T [°C]			
$\dot{\varepsilon}$ [1/s]	1010	1050	1100	1150	1010	1050	1100	1150	1010	1050	1100	1150
10	2.9	5.2	5.0	3.8	-28.1	-28.5	-25.1	-23.9	-2.0	-3.0	-1.8	-2.1
1	-0.6	-4.6	-5.2	-2.5	1.4	-2.1	-3.0	-0.4	7.4	-0.8	-1.7	0.5
0.1	-4.9	-3.4	-2.2	-3.8	11.9	12.1	11.7	8.7	5.2	2.8	3.4	0.9
0.001	2.6	2.9	2.4	2.5	-4.7	-25.1	-22.4	-21.9	1.5	-0.4	-0.4	-0.2
RMSE	3.1	4.1	4.0	3.2	15.4	19.9	17.9	16.8	4.7	2.1	2.1	1.2
mean	**3.6**				**17.5**				**2.5**			

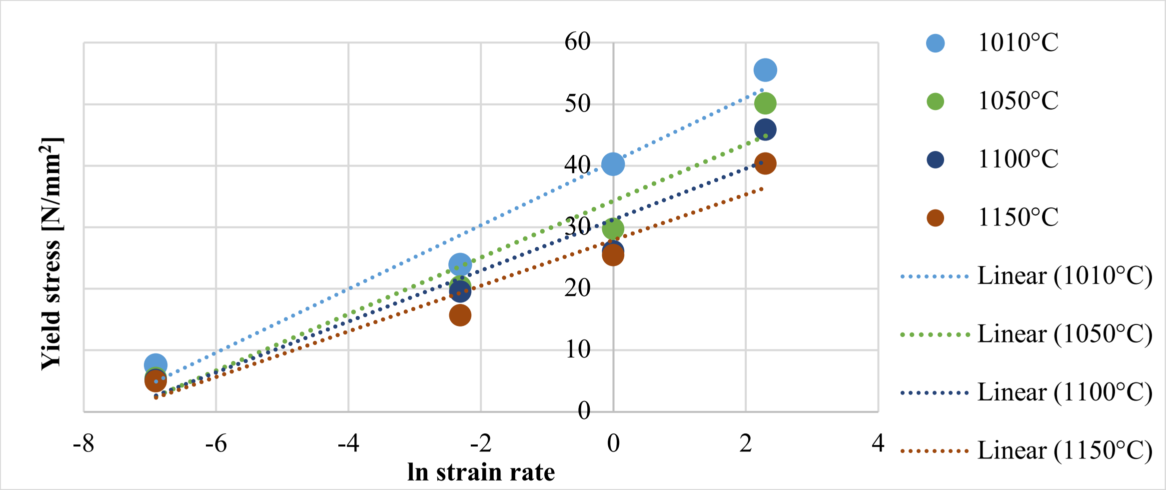

Figure 29: Linear fit for yield stresses, dashed line is the fit for the experimental points.

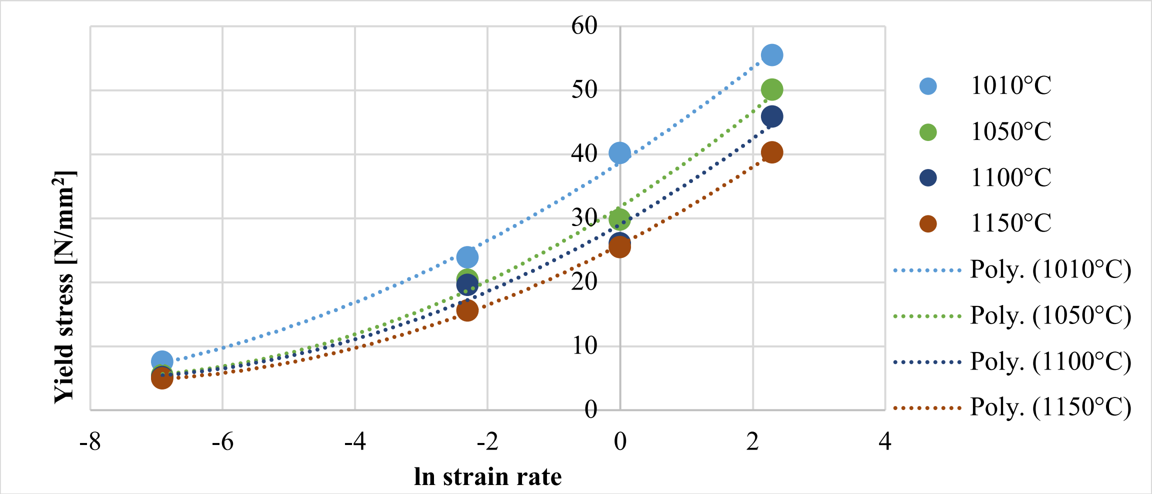

Figure 30: Polynomial fit for yield stresses, dashed line is the fit for the experimental points.

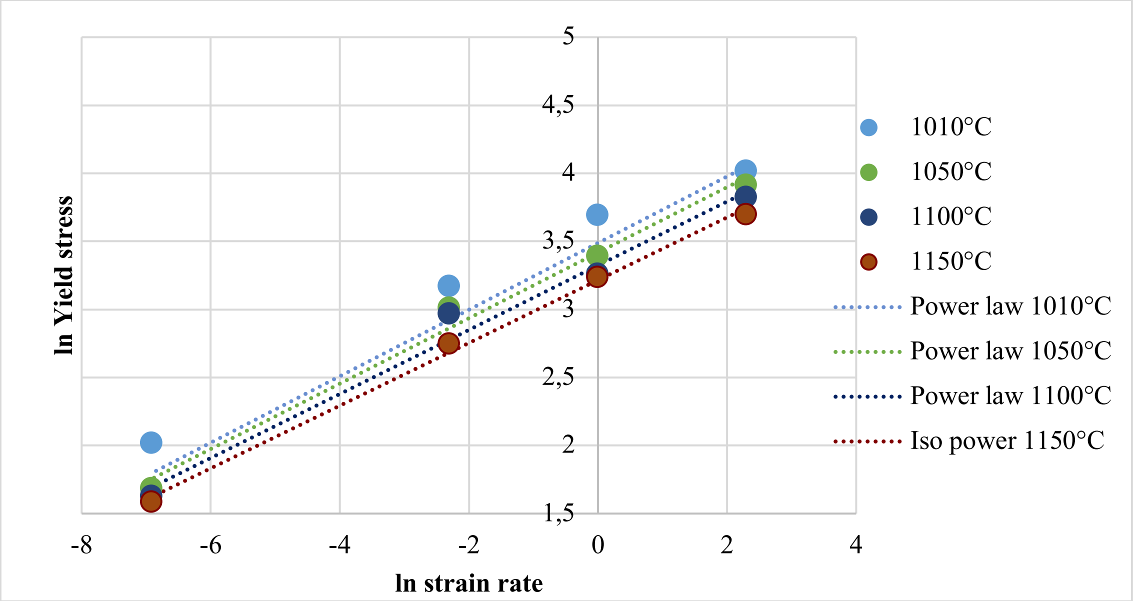

Figure 31: Fit with ln of yield stress and strain, dashed line is the fit for the experimental points.

The natural logarithm of sigma YS was plotted versus the natural logarithm of the strain rate. The slope and the exponential of the intercept of the linear fits were plotted versus the temperature.

$$\sigma_{YS} = A\,\dot{\varepsilon}^{B} \qquad eq.\ 41$$

$$ln\,\sigma_{YS} = lnA + B\,ln\dot{\varepsilon} \qquad eq.\ 42$$

Accordingly, A and B are linear functions of the temperature.

$$A = A_1 + B_1\,T \qquad eq.\ 43$$

$$B = A_2 + B_2\,T \qquad eq.\ 44$$

The correlation with temperature for the two parameters showed good agreement.

Table 11: Parameters of a linear fit for the yield stress function.

A_1	B_1	A_2	B_2
89.0	-0.0573	0.346	-0.000100
0.998	R^2	0.997	R^2

In the deformation loop of the model, which represents the deformation process, the evolution of the microstructure and the flow stress are described using modified expression from Kocks and Mecking [24] and Montheillet et al. [17]. The model was implemented in a Matlab project comprising the concept file of the model (solveFlowStress.m) and a command file (mainMultiple.m). The numerical calculation is built using incremental time steps (Δt).

From the hardening point of view dislocations can form dipoles or immobile dislocations. This is described by the hardening coefficient h_1.

$$\frac{\partial \rho_i}{\partial t} = h_1\,\dot{\varepsilon} \qquad eq.\ 45$$

In terms of recovery, the recovery coefficient h_2 is used. Immobile dislocations and dipoles may form walls or go to already existing walls and decrease thereby the subgrain size. The following equations describe these two evolutions of dislocations, and the fractions are represented by the parameter α_1.

Formation of walls:

$$\frac{\partial \rho_i}{\partial t} = h_2\, \alpha_1\, \rho_i\, \dot{\varepsilon} \qquad \textit{eq. 46}$$

Moving to walls:

$$\frac{\partial \rho_i}{\partial t} = h_2\, (1-\alpha_1)\rho_i\, \dot{\varepsilon} \qquad \textit{eq. 47}$$

A third part describes the movement of HAB.

$$\frac{\partial \rho_i}{\partial t} = -\,(\rho_i + \rho_m) S_V f_{HAB} v_{HAB} \qquad \textit{eq. 48}$$

S_V is total area of boundaries per unit volume [1/m], f_{HAB} and v_{HAB} correspond to the surface fraction and velocity [m/s] of high angle boundaries and Δt is the time step of the already modelled deformation. The fitting parameters h_1 and h_2 vary with temperature and strain rate similarly to the parameters in the Kocks Mecking model.

$$h_1 = h_{0,1}\, \dot{\varepsilon}^{m_{h_1}} \exp\left(\frac{m_{h_1} Q_{h_1}}{RT}\right) \qquad \textit{eq. 29}$$

$$h_2 = h_{0,2}\, \dot{\varepsilon}^{-m_{h_2}} \exp\left(-\frac{m_{h_2} Q_{h_2}}{RT}\right) \qquad \textit{eq. 30}$$

The change in immobile dislocation density also affects the total area of boundaries per unit volume S_V. The change in this surface fraction consists of the area of LABs with a misorientation angle θ_0 forming during the deformation $dS_V{}^{+}$ and the area annihilated through moving HABs $dS_V{}^{-}$.[17]

$$dS_V{}^{+} = \frac{b}{n_w \theta_0} \alpha_1 \frac{\partial \rho_i}{\partial t} \qquad \textit{eq. 49}$$

$$dS_V{}^{-} = S_V\, dV \qquad \textit{eq. 50}$$

$$dS_V = dS_V{}^{+} + dS_V{}^{-} \qquad \textit{eq. 51}$$

dS_V is the total change of surface fraction of HAB, dV is the volume swept by mobile boundaries. The increment in the surface fraction of LAB $S_{V,LAB}$ causes an increment in the misorientation angle θ.

$$d\theta = (1-\alpha_1) \frac{b}{2\, n_w} h_2\, \rho_i \frac{2}{S_{V,LAB}}\, \dot{\varepsilon} \qquad \textit{eq. 52}$$

A recalculation of the misorientation angle distribution yields in a new average misorientation angle, so concluding in a new wall dislocation density and new stresses.

The parameters in the expression for h_1 and h_2, the constant α_1 accounting for the recovered dislocation density forming new LAB misorientation of the starting misorientation angle θ_0 for the β phase, the factor for the wall dislocation density f_{ρ_w} and a factor for the yield stress function f_{YS} needed to be fit for Ti64. f_{ρ_w} was fitted for different strain rates and then described by a Boltzmann function, see Figure 32.

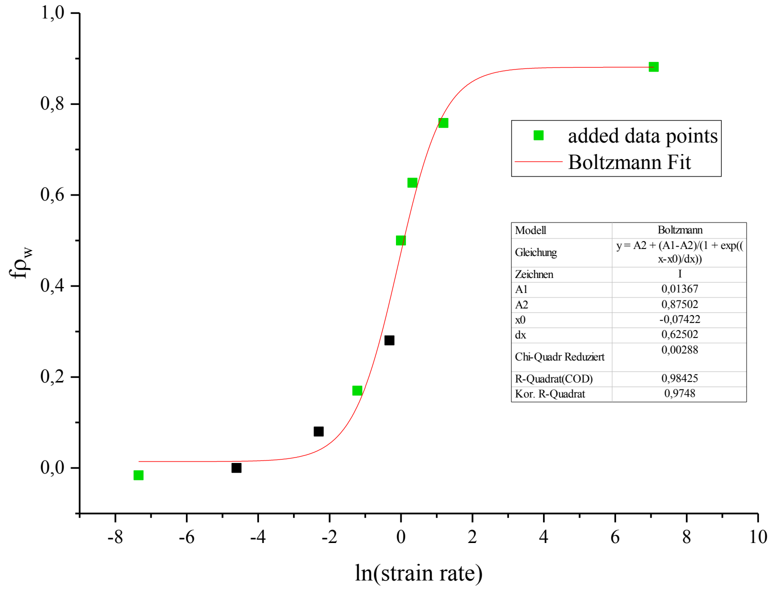

Modell	Boltzmann
Gleichung	y = A2 + (A1-A2)/(1 + exp((x-x0)/dx))
Zeichnen	I
A1	0,01367
A2	0,87502
x0	-0,07422
dx	0,62502
Chi-Quadr Reduziert	0,00288
R-Quadrat(COD)	0,98425
Kor. R-Quadrat	0,9748

Figure 32: Boltzmann fit of f_{ρ_w}. *Black data points were fitted to meet experimental values of the flow stress, green data points were added to predict a complete Boltzmann function.*

f_{YS} was introduced as a simple multiplying factor of 0.7 to account for the difference in yield strength between compression and torsion tests and was finally incorporated in the function for the yield stress itself. The strain rate sensitivity m and the activation energy Q accounted for the influence of strain rate and temperature on the flow curves.

The strategy on the fitting of the different parameters was the following: Rather than meeting the shape in the beginning, the adjustable parameters were changed so that the modelled flow curve resembled the experimental curve regarding the value of the peak stress and the amount of softening proceeding to the maximum flow stress.

Table 12 summarizes the different parameters for setting up the CDRX model for Ti64.

Table 12: Parameters for setting up the CDRX model for Ti64.

Parameter	Symbol	Value	Value taken from
initial value hardening coefficient	$h_{1,0}$	$26 \cdot 10^{14}$ m^{-1}	fitting
initial value recovery coefficient	$h_{2,0}$	570	fitting
strain rate sensitivity for h_1	m_{h_1}	0	fitting
strain rate sensitivity for h_2	m_{h_2}	0.18	fitting
activation energy for h_1	Q_{h_1}	1800 J/mol	fitting
activation energy for for h_2	Q_{h_2}	13800 J/mol	fitting
Taylor factor	M	$2.53985 + 0.48661 \cdot \exp(-2.16688 \cdot \varepsilon)$	literature [48]
numerical constant	α	0.1	fitting
constant	α_1	0.0015	fitting
Poisson ratio	v	$0.34105 + 3.76502 \cdot 10^5 \cdot T$	calculated from JMatPro® simulation
Young modulus	E	$10^9(117.3327 - 0.04563 \cdot T)\ [Pa]$	calculated from JMatPro® simulation
Yield stress	σ_{YS}	function of T and $\dot{\varepsilon}$	experimental yield stress
Factor for ρ_w	f_{ρ_w}	function of $\dot{\varepsilon}$	fitting

The used model of CDRX was originally implemented for Ti5553, therefore some material specific values were changed in this work, namely the β-transus temperature, the function of the yield stress, the Young's modulus and Poisson ratio according to calculation with the software JMatPro and the Taylor factor. The Taylor factor was assumed not to be constant but to be a function of strain. The used equation was applied before for Ti64 in the α+β field with a lamellar microstructure. [48]

4. Results

4.1. Microstructure before hot deformation

The microstructure of the base material for the fabrication of the torsion samples is shown in Figure 33 in the potential rolling direction of the plate and another section orthogonal to the first one. The microstructure consists mostly of globular α, some lamellar α and little β phase. The potential rolling direction shows some regions with elongated grains while the perpendicular section shows larger grains with less defined grain boundaries additionally to some lamellar α and little β phase.

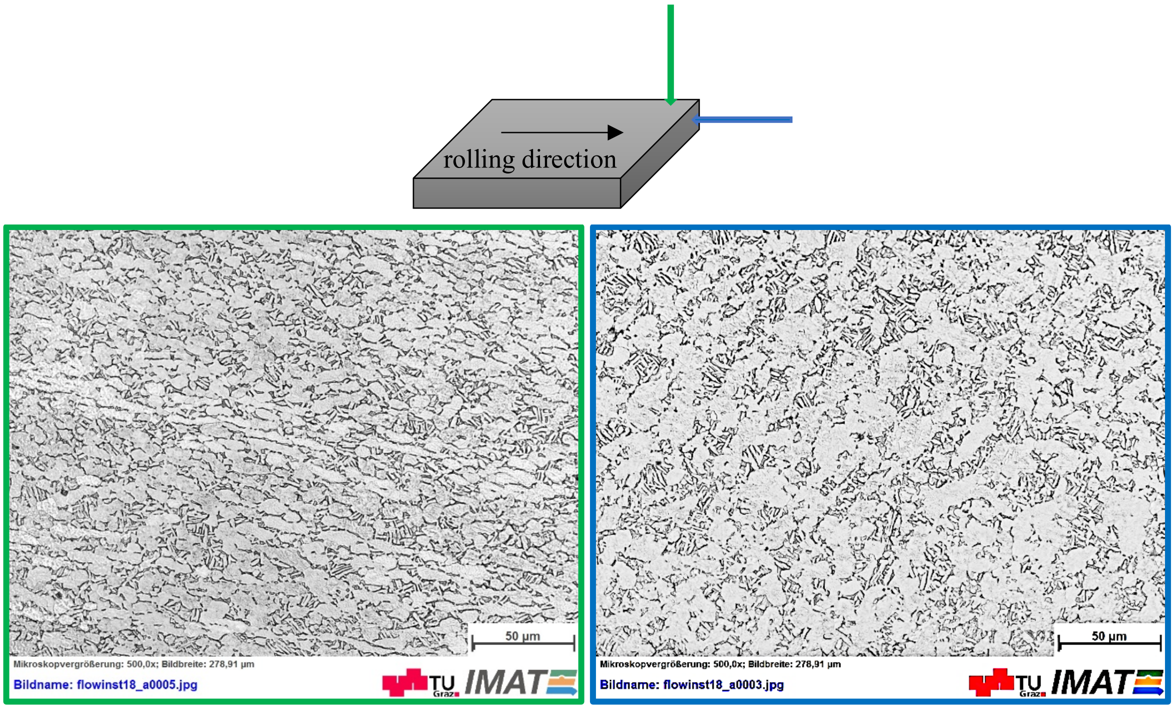

Figure 33: base material of Ti64 plate. a) potential rolling direction, b) orthogonal direction to left.

The microstructures of the base material after two different heat treatments are depicted in Figure 34 and Figure 35. The grain size obtained after heat treatments at 1050° for 30 min or 10 min holding time are similar. For the water quenched sample the microstructure shows the former β grains transformed into martensite. The samples that were cooled down slowly in the furnace show a lamellar structure. A detail of the lamellae can be seen in Figure 36. The thickness of the lamellae is similar for the two different holding times, but the shape of the lamellae seems more irregular for longer holding times. Also, the lines of α at the grain boundary are sharper for a holding time of 10 minutes, see Figure 36.

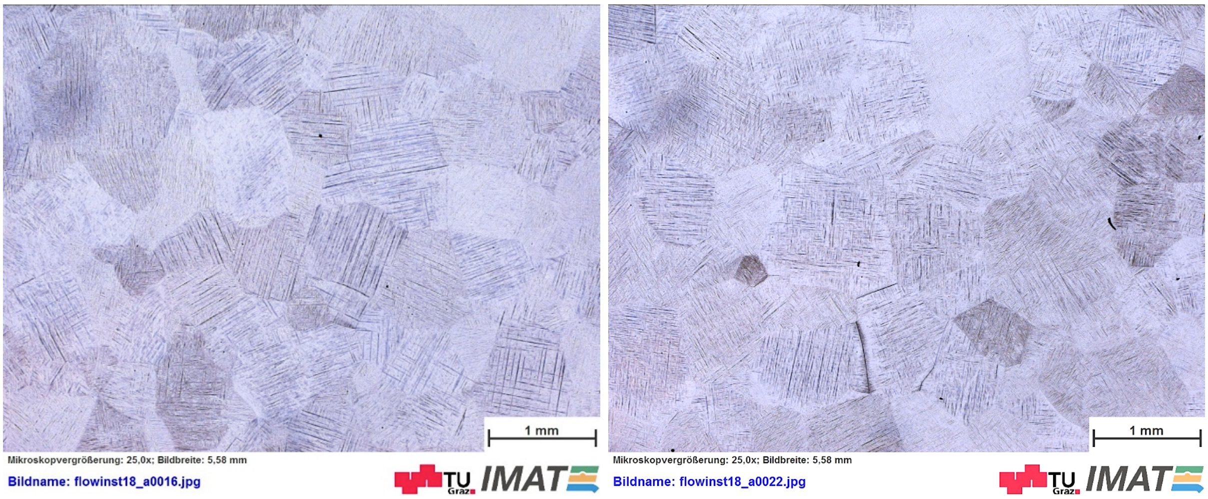

Figure 34: 1050 °C, water quenched. a) 10 min holding time, b) 30 min holding time.

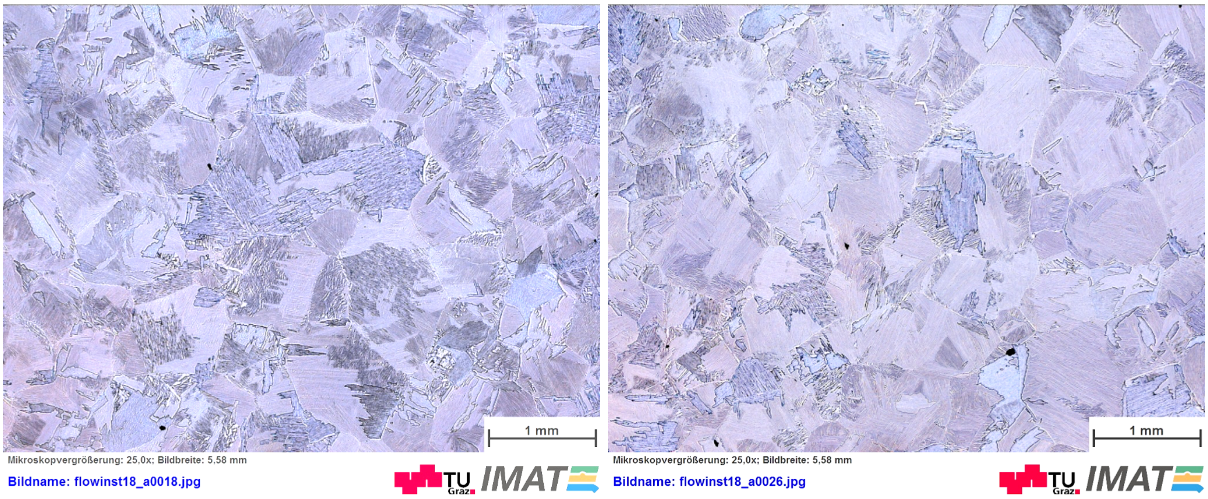

Figure 35: 1050 °C, furnace cooled. a) 10 min holding time, b) 30 min holding time.

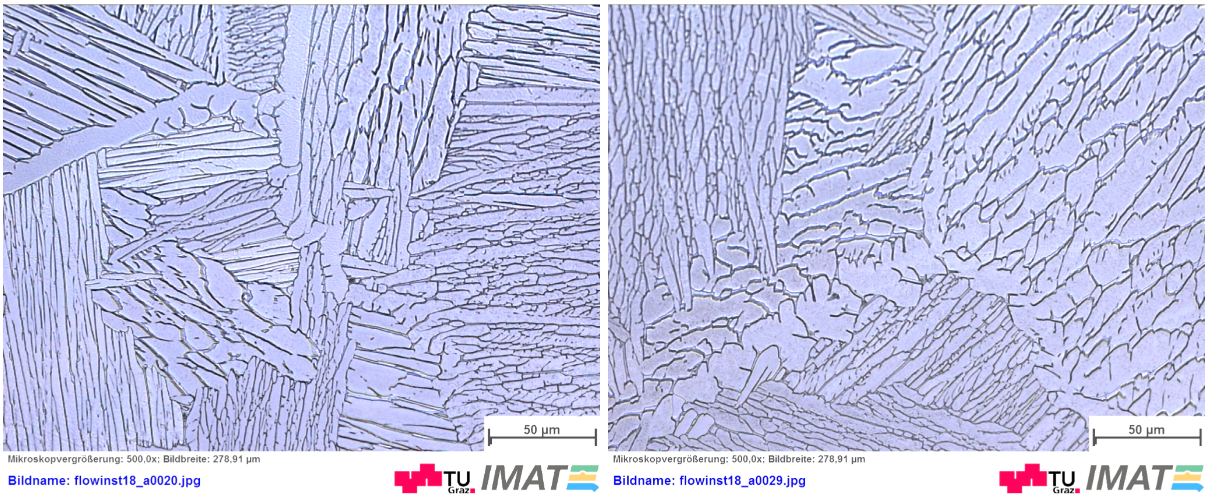

Figure 36: 1050 °C, furnace cooled. a) 10 min holding time, b) 30 min holding time.

4.2. Compression flow curves

The temperature correction was applied for all the experimental compression flow curves. Figure 37 shows the effect of the temperature correction in the α+β field for different temperatures; Figure 38 shows the effect in the β field.

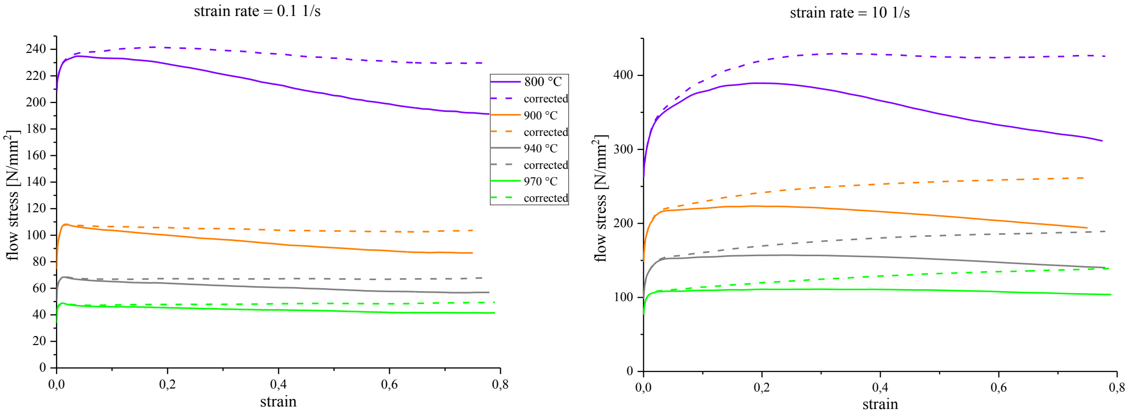

Figure 37: Temperature correction in the α+β field, a) for a strain rate of 0.1 1/s, b) for a strain rate of 10 1/s.

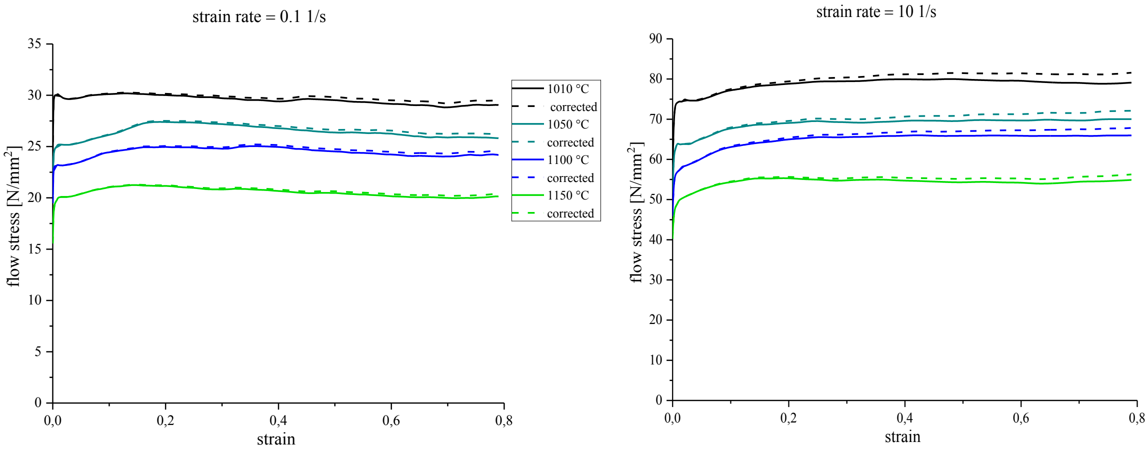

Figure 38: Temperature correction in the β field, a) for a strain rate of 0.1 1/s, b) for a strain rate of 10 1/s.

Figure 39 and Figure 40 show the effect of the temperature correction for all strain rates at one temperature, below and above β transus temperature, respectively. Looking also at Figure 41 the temperature correction shows a larger effect for high strain rates and low temperatures. The impact of the temperature correction on the flow stresses is larger for the experiments in the α+β field than in the β field.

Regarding the correlation of different conditions for a hot compression test, it can be observed that the maximum flow stresses rises for low temperatures and high strain rates. For these conditions also the steady state flow stress is reached at larger strains compared to high temperatures and low strain rates.

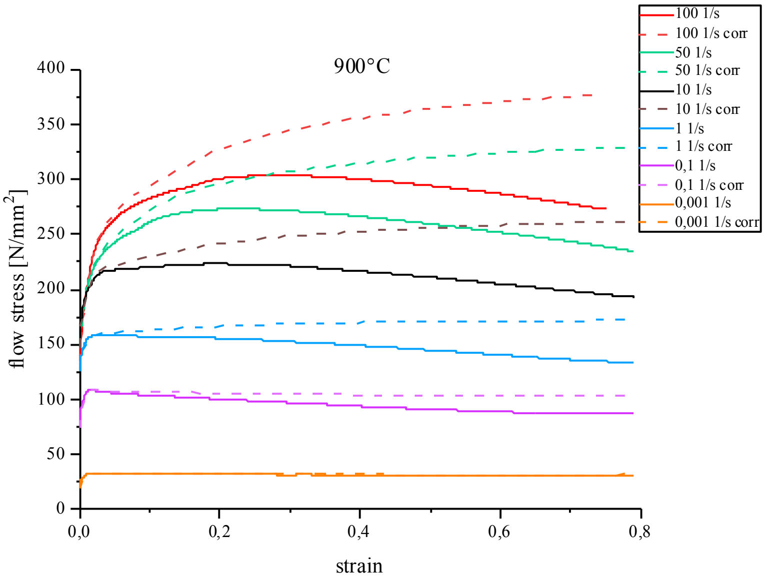

Figure 39: Temperature correction in the α+β field for a temperature of 900°C.

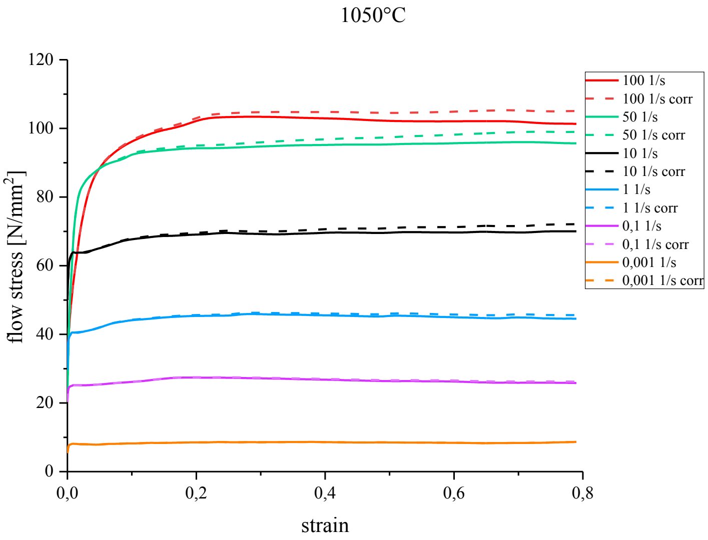

Figure 40: Temperature correction in the β field for a temperature of 1050°C.

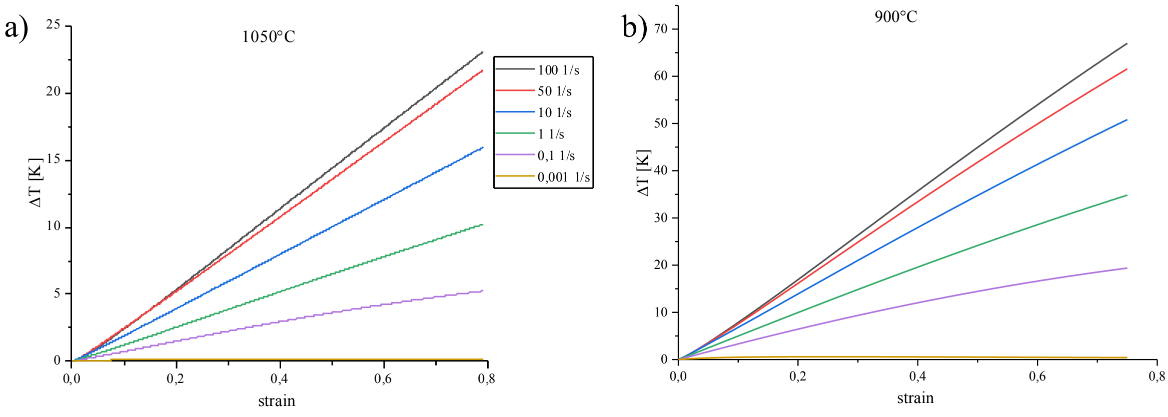

Figure 41: Calculated increment in temperature during compression at a) 1050°C and b) 900°C.

4.3.Torsion flow curves

The flow curves of samples with initial lamellar microstructure show an irregular progression of the flow stress with respect to strain. The flow curves obtained from the samples with initial lamellar microstructure show no dependency on the temperature for strains larger than 1. The tendency for higher flow stresses at low temperatures is not as pronounced as for the samples with as received material. A direct comparison of same experimental conditions is done in Figure 43 for lamellar and globular microstructure. While the steady state flow stress values are similar, the yielding in the beginning of the curve for samples with globular initial microstructure is only 75-80% of the yield stress of the samples with lamellar microstructure.

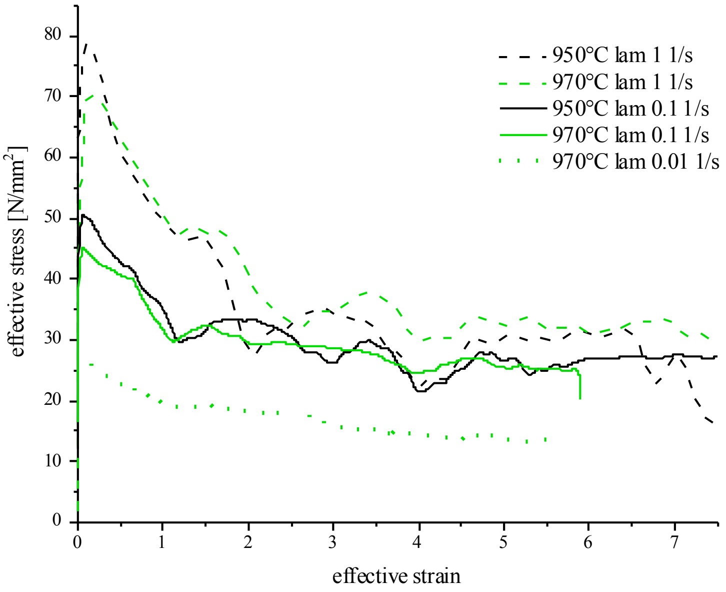

Figure 42: Flow curves of samples with starting lamellar microstructure tested in the α+β field.

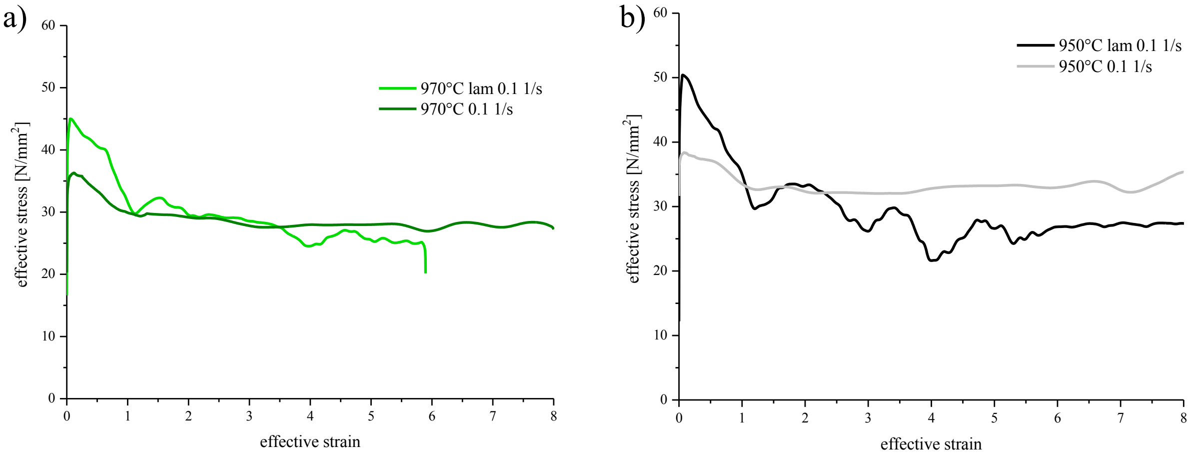

Figure 43: Flow curves of samples tested in the α+β field, comparing the as received globular with the lamellar microstructure a) at 970°C, b) at 950°C. The test at 970°C 0.1 1/s with lamellar microstructure was only programmed to 6 revolutions, while all other tests were programmed for 8 revolutions.

The flow curves with initial globular microstructure are more regular in shape, compared to the samples with initial lamellar microstructure. Figure 44 shows all flow curves measured in the β field after data treatment performed as described in 3.5.2. As for the flow curves obtained from compression, maximum flow stresses rise for low temperatures and high strain rates. Only the curve measured at 1070°C 0.1 1/s strain rate is an exception to this tendency. After a peak stress at low strains all flow curves show a softening behaviour at higher strains, which is more pronounced for higher strain rates (1 1/s).

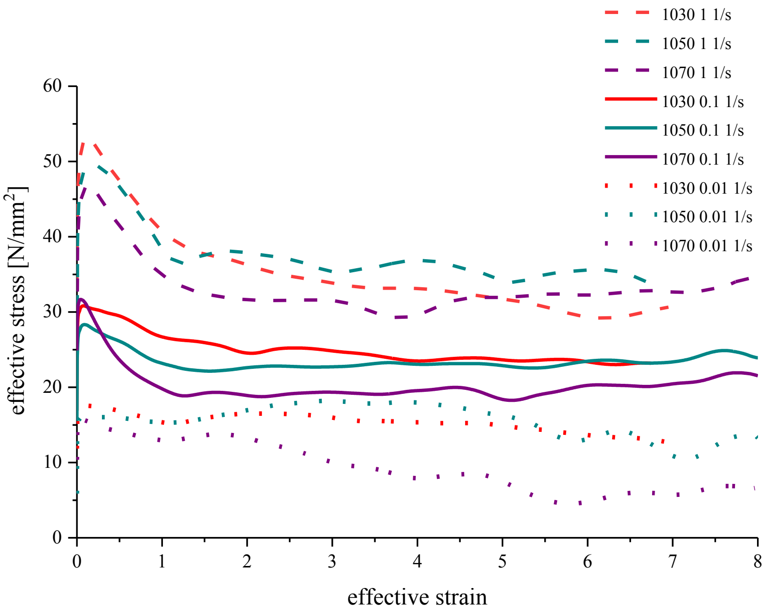

Figure 44: Flow curves of samples tested in the β field.

Comparing the flow curves measured in the α+β and the β field for a strain rate of 0.1 1/s in Figure 45, the rise in flow stress for lower temperatures can also be observed across phase transformations occurring inside of the material.

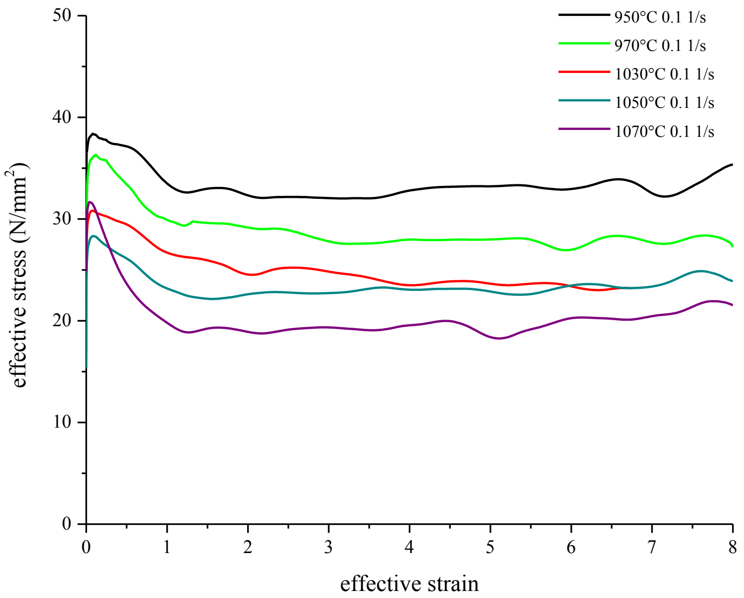

Figure 45: Flow curves of samples tested in as received condition at a strain rate of 0.1 1/s for different temperatures.

4.4. Microstructure after deformation

The details of the deformed microstructures are always taken in the longitudinal axis or the transverse axis of the sample, see Figure 46.

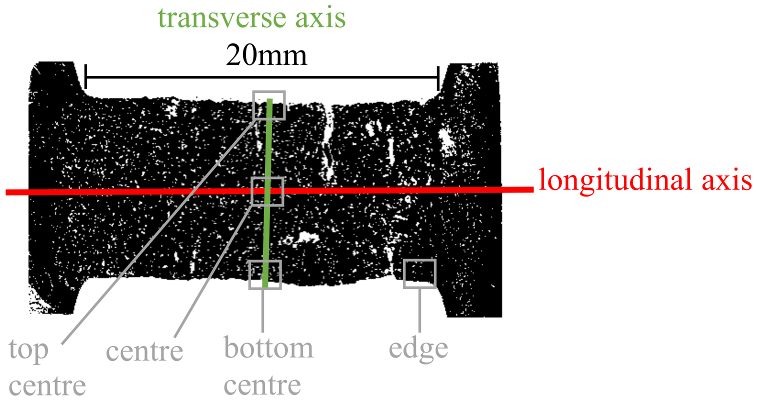

Figure 46: Torsion sample prepared for metallography marked with transverse and longitudinal axis and exemplary observed positions.

The samples with globular starting microstructure deformed in the α+β field show next to martensitic grains some particles of globular α. The microstructure of samples deformed at 950°C shows more α particles than after deformation at 970°C for the same strain rate. Also, a gradient of the particles is visible with more globular α on the edge and fewer globular α in direction of the centre of the sample, see Figure 47.

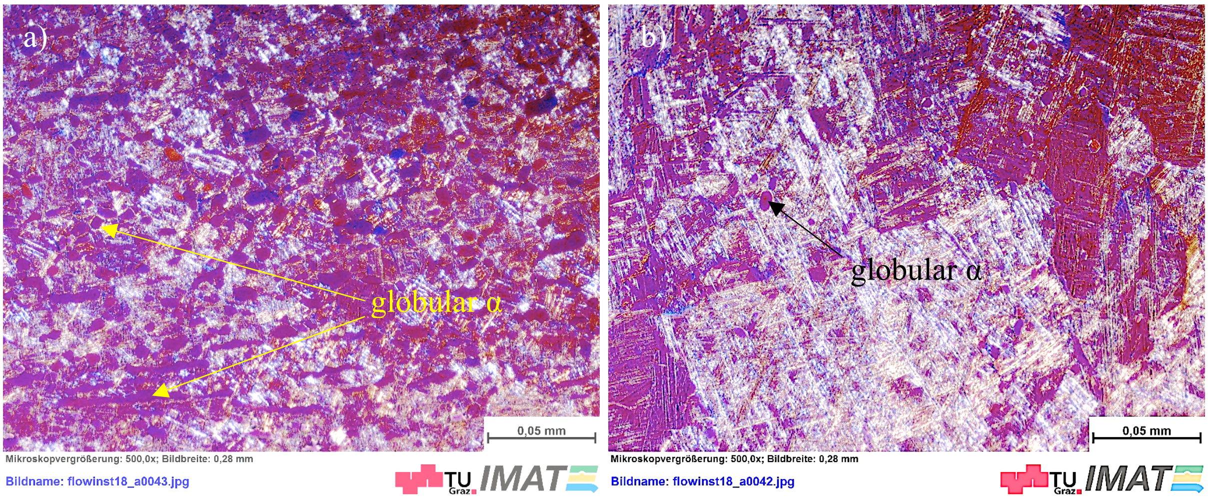

Figure 47: 950°C 0.1 1/s strain rate in polarized light. a) edge of sample, b) 4 mm closer to the centre of sample.

For all observed sections of the torsion samples deformed in the α+β field, a gradient in grain size from the centre to the sides was observed, see one example in Figure 48. Comparing the top centre of the sample (where the thermocouple was mounted) and the bottom centre, not a clear difference can be seen in the qualitative analysis, Figure 48 and Figure 49.

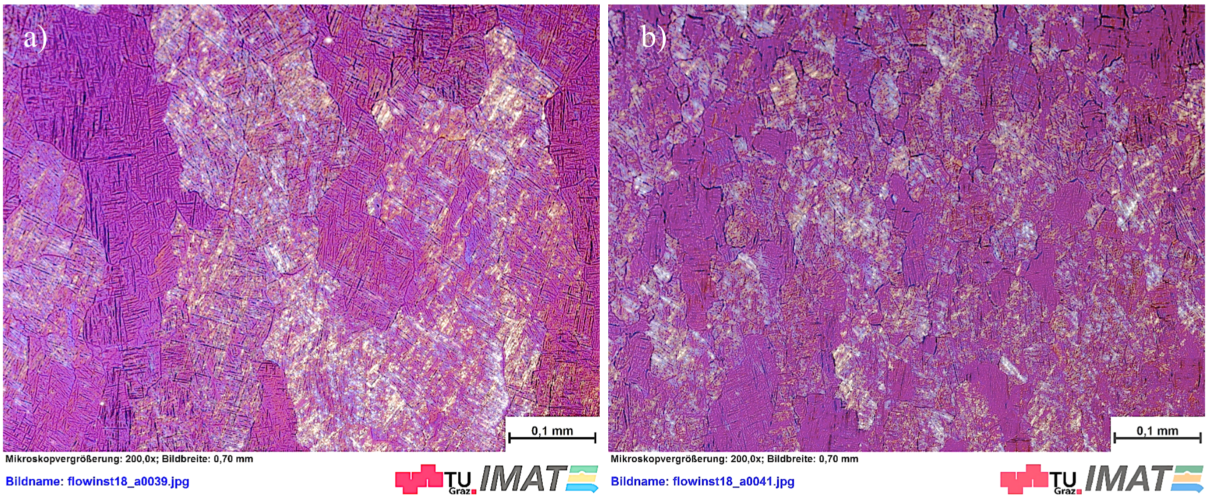

Figure 48: 950°C 0.1 1/s strain rate in polarized light. a) centre of sample, b) bottom centre.

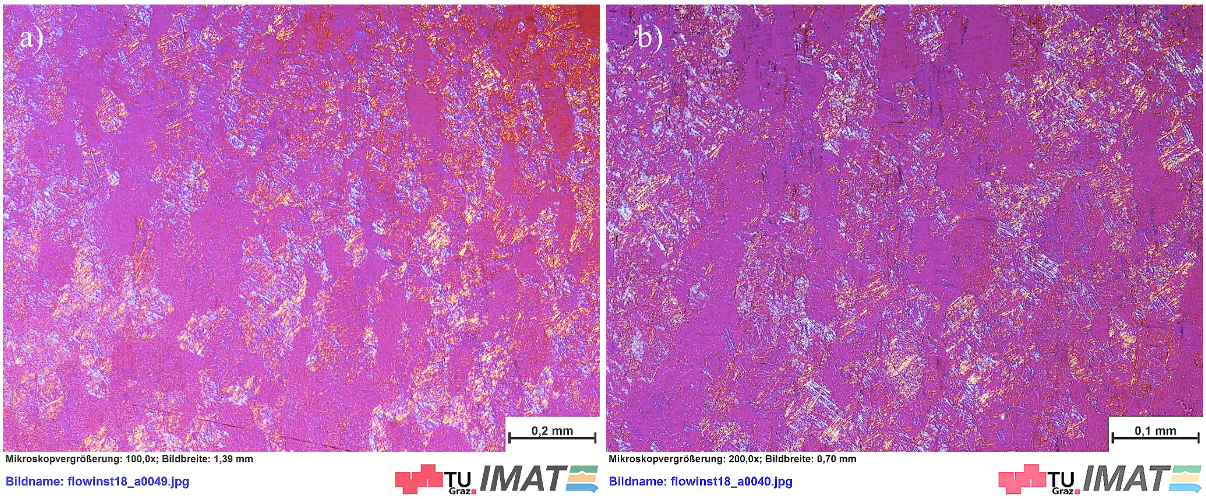

Figure 49: Top centre of the samples in polarized light. a) 970°C 0.1 1/s, b) 950°C 0.1 1/s.

In Figure 50 the transition from the undeformed to the deformed microstructure is visible. For the deformation at 970°C with 0.1 1/s the as received globular starting microstructure shows small grains in the undeformed zone, while the sample with lamellar starting microstructure shows large undeformed grains, resulting from the heat treatment above the β transus temperature. A difference in the flow behaviour between the as received and the heat treated material cannot only be seen in the measured data, but also on a macroscopic scale. The deformed section for the heat treated sample deformed at 950°C 0.1 1/s strain rate looks more irregular than the sample deformed at the same conditions with the material in as received condition, see Figure 51.

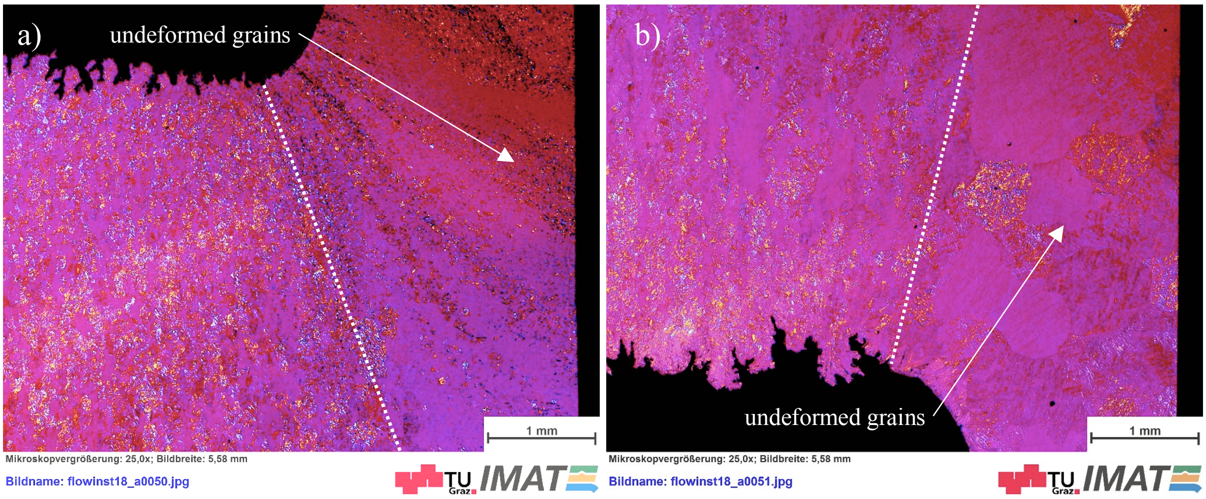

Figure 50: Transition (dotted line) from deformed to undeformed material 970°C 0.1 1/s. a) as received material, b) lamellar initial microstructure.

Figure 51: Macropicture of samples deformed at 950 °C 0.1 1/s strain rate up to strains of 8. Top: after deformation of as received structure, bottom: lamellar initial microstructure.

The lamellae for the heat treated torsion samples that formed at the deformation temperature, occurred to be thin and hard to distinguish from martensite formed during quenching. With large magnification fine features of primary α are visible in the microstructure, see Figure 52 and Figure 53. The α phase either occurs as lamellae or thin layers on the prior β grain boundaries.

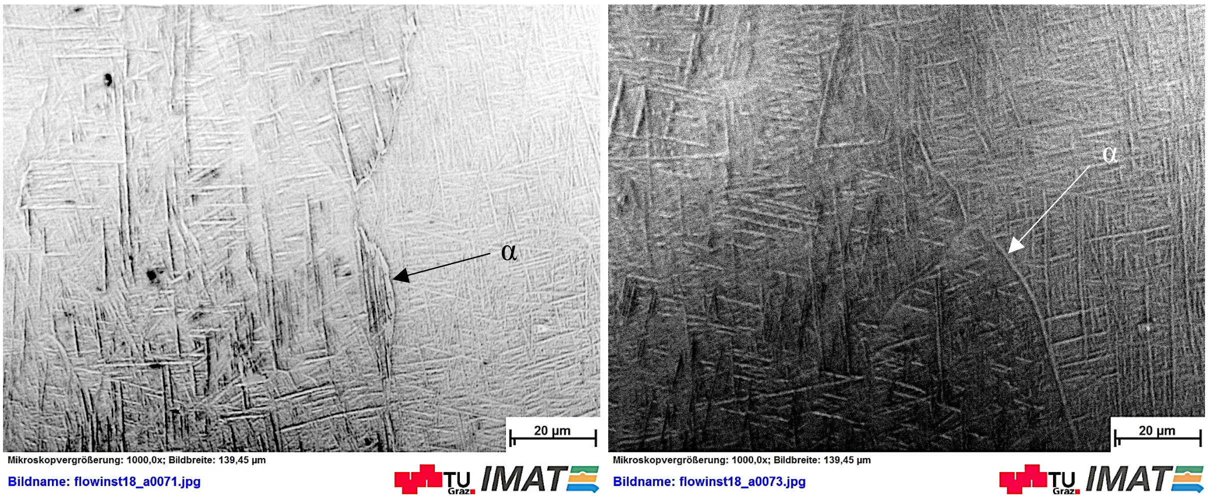

Figure 52: 970°C 1 1/s lamellar. α phase at prior β grain boundaries.

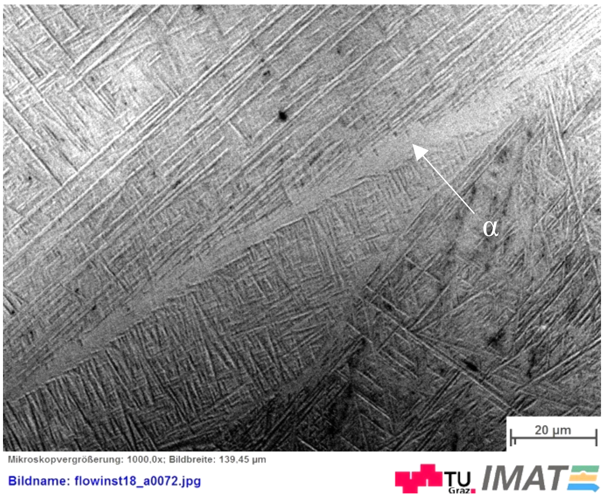

Figure 53: 970°C 1 1/s lamellar. Grain boundary α.

The samples deformed in the β field for a temperature of 1070°C show larger grains for slow strain rates, see Figure 54. The gradient of grain size from the sample centre to the sides is not as pronounced in the β field as for the deformation in the α+β field, for comparison see Figure 55. For low strain rates the difference in grain size for varying temperatures is not very distinct, see Figure 56.

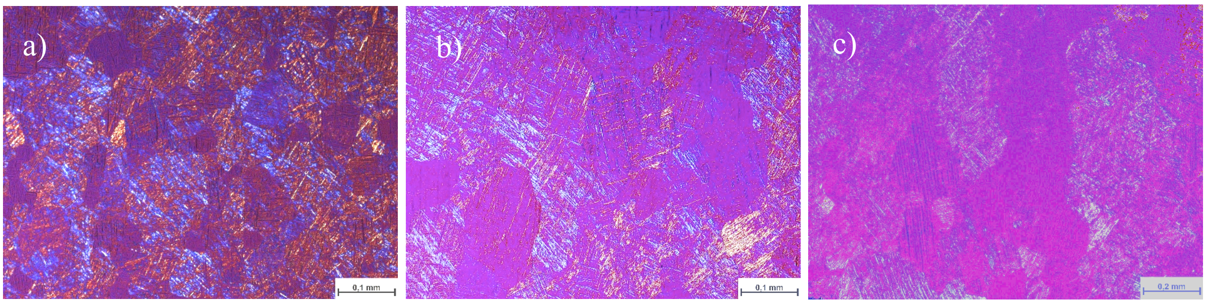

Figure 54: Deformation at 1070 °C with a strain rate of a) 1 1/s, b): 0.1 1/s, c) 0.01 1/s.

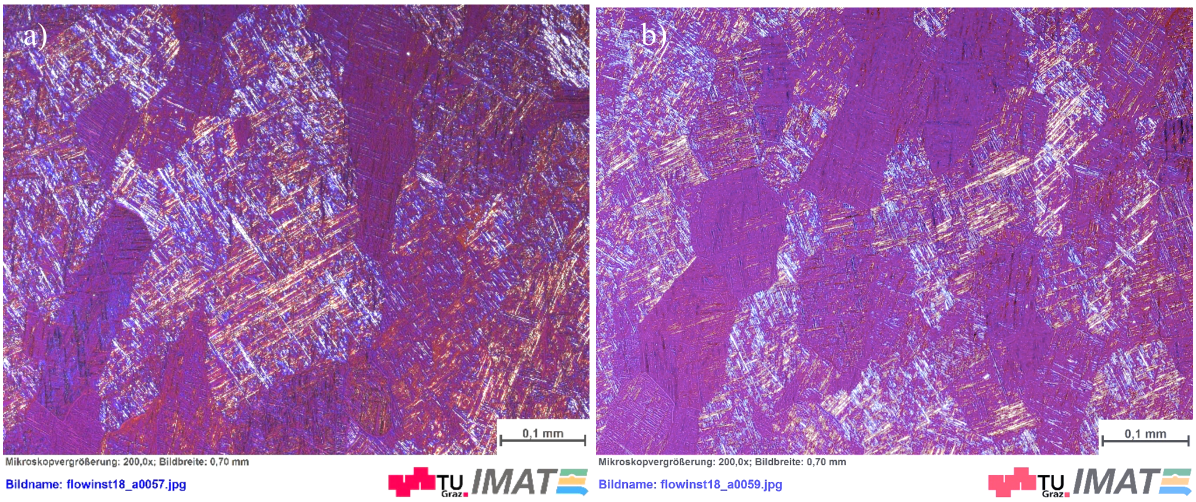

Figure 55: 1070°C 0.1 1/s strain rate in polarized light. a) centre of sample. b) bottom centre.

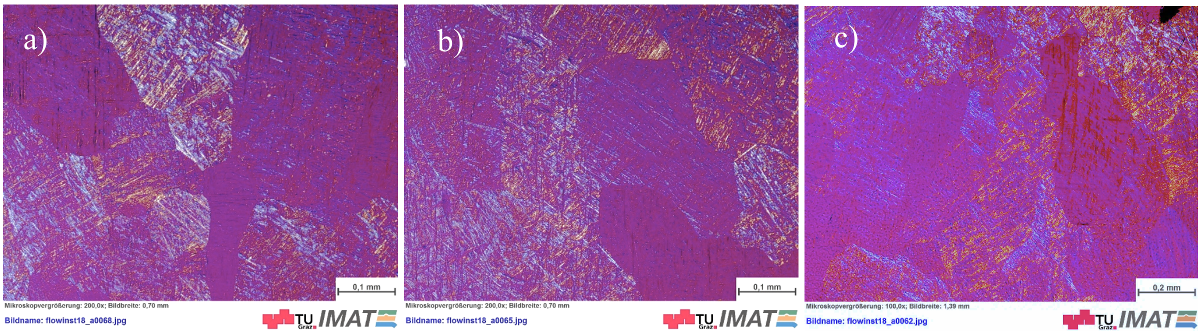

Figure 56: Deformation with 0.01 1/s strain rate, bottom centre. a) 1030 °C, b) 1050°C, c) 1070°C.

Within some very large grains, the substructure in the former β grains can be estimated. The martensite within these grains is not exactly parallel but changes its direction slightly within the grains, i.e. from prior subgrain to subgrain. Figure 57 shows a detail of β grains deformed and quenched.

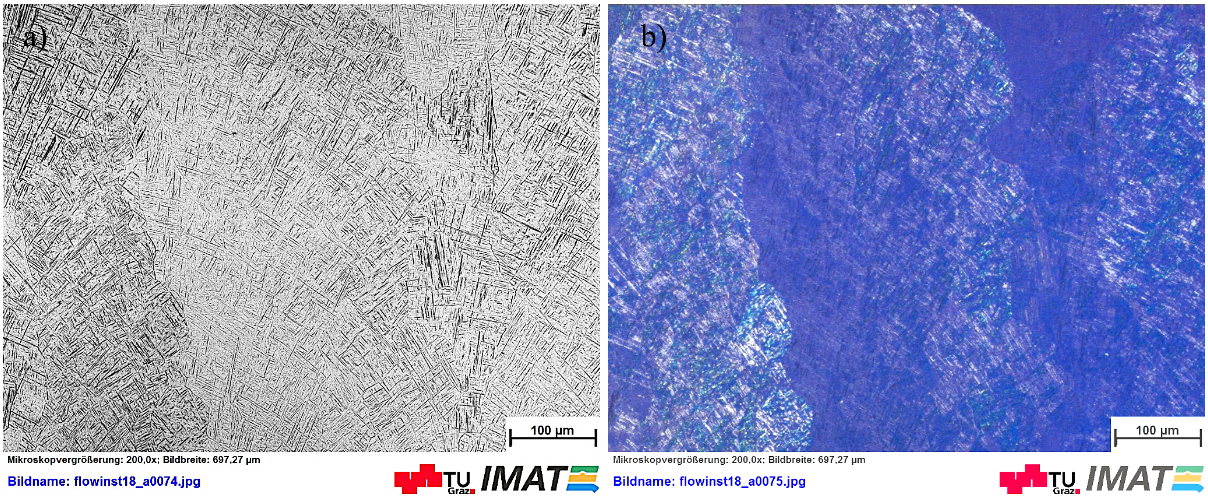

Figure 57: Sample deformed at 1070°C 1 1/s, detail in a) bright field, b) polarized light.

4.5. Modelling results

4.6. Kocks Mecking modelling

The evolution of hardening and the recovery coefficients of the Kocks Mecking model with strain rate and temperature is shown in Figure 58. The hardening coefficient rises for high strain rates and low temperatures, while the recovery coefficient is large for low strain rates and high temperatures.

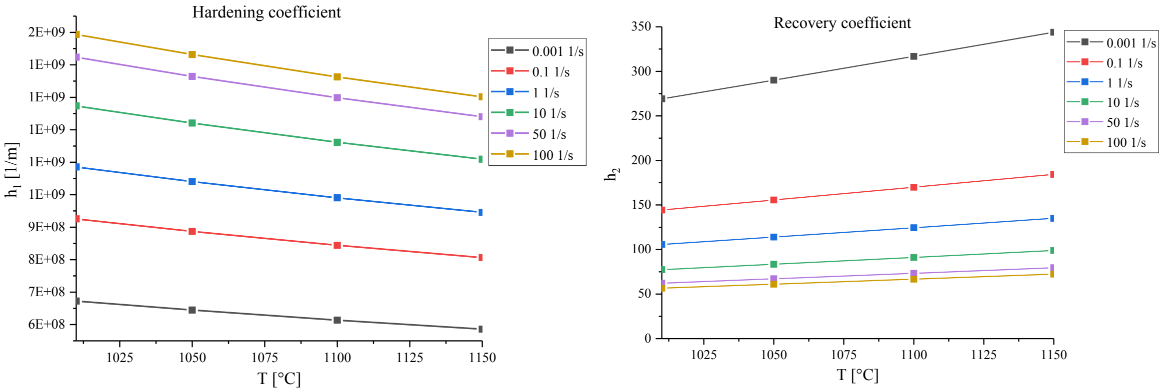

Figure 58: Evolution of hardening (h_1) and recovery (h_2) coefficient with strain rate and temperature.

The root mean square error fitting using Solver function of Excel fitted all parameters for the Kocks Mecking model for all flow curves at the same time. The total difference between modelled and experimental curves was 59.46 MPa, ranging from 0.7 to 8.08 N/mm^2 difference for each curve. Generally, the modelling results fitted better for intermediate strain rates from 0.1-10 1/s than for very low (0.001 1/s) and very high (50 and 100 1/s) strain rates. Figure 59 to Figure 61 show the flow stresses obtained from Kocks Mecking modelling results for strain rates from 0.001 1/s to 100 1/s compared to experimental flow curves. For all strain rates and temperatures, the steady state flow stress of the modelled flow curves is reached at very low strains ($\varepsilon < 0.2$). The steady state in flow stress is reached earlier for low strain rates. For one strain rate the steady state is reached at the same strain, even if the temperature differs.

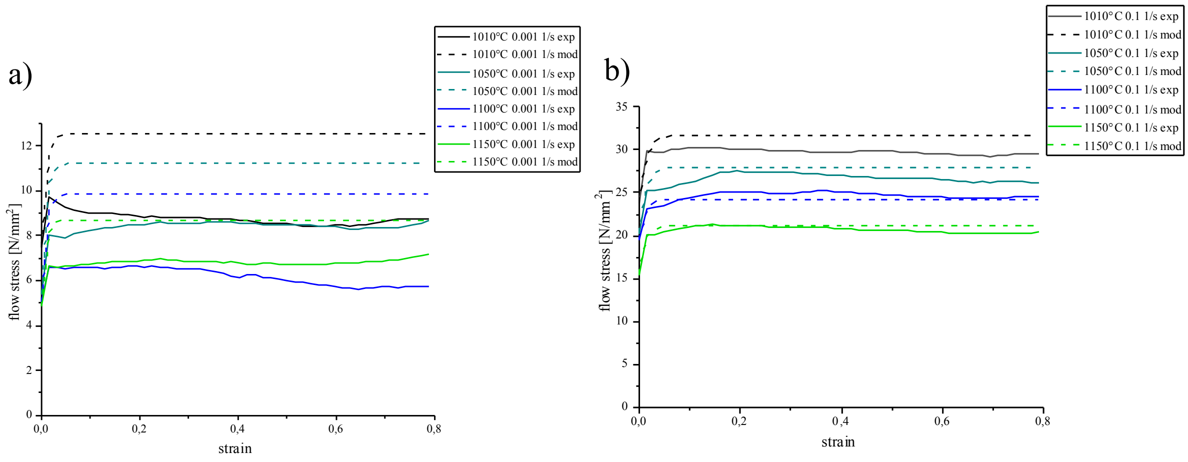

Figure 59: Modelled (dashed) compared to experimental (full line) flow stresses for a strain rate of a) 0.001 1/s, b) 0.1 1/s.

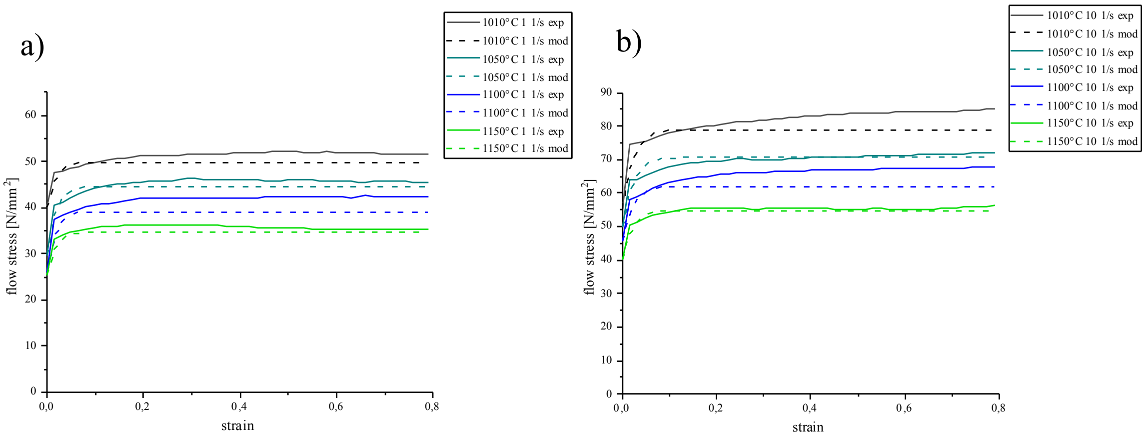

Figure 60: Modelled (dashed) compared to experimental (full line) flow stresses for a strain rate of a) 1 1/s, b) 10 1/s.

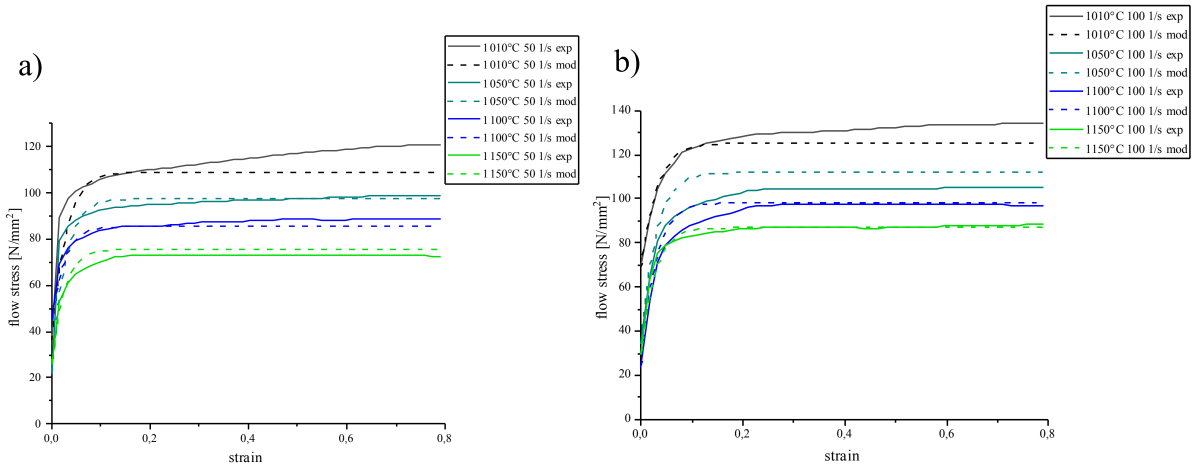

Figure 61: Modelled (dashed) compared to experimental (full line) flow stresses for a strain rate of a) 50 1/, b) 100 1/s.

The Kocks Mecking model also provides a dislocation density evolution as output. Figure 62, Figure 63 and Figure 64 show the evolutions of dislocation density for different strain rates and temperatures in the β field of Ti64. The final value of dislocation density rises for high strain rates and low temperatures. Also, it can be noted, that the steady state dislocation density is reached earlier (at lower strains) for slow strain rates, while the temperature has no influence on the saturation behaviour.

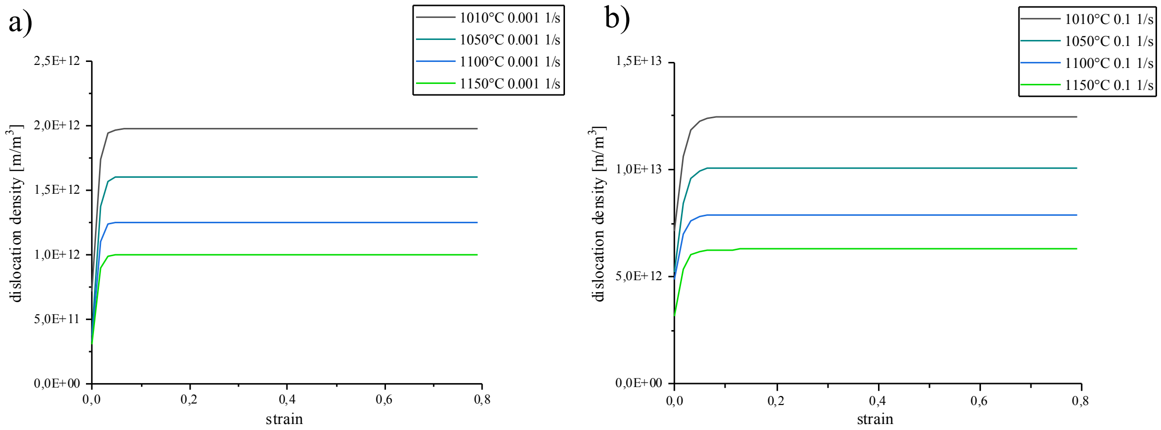

Figure 62: Modelled dislocation density for a strain rate of a) 0.001 1/s, b) 0.1 1/s.

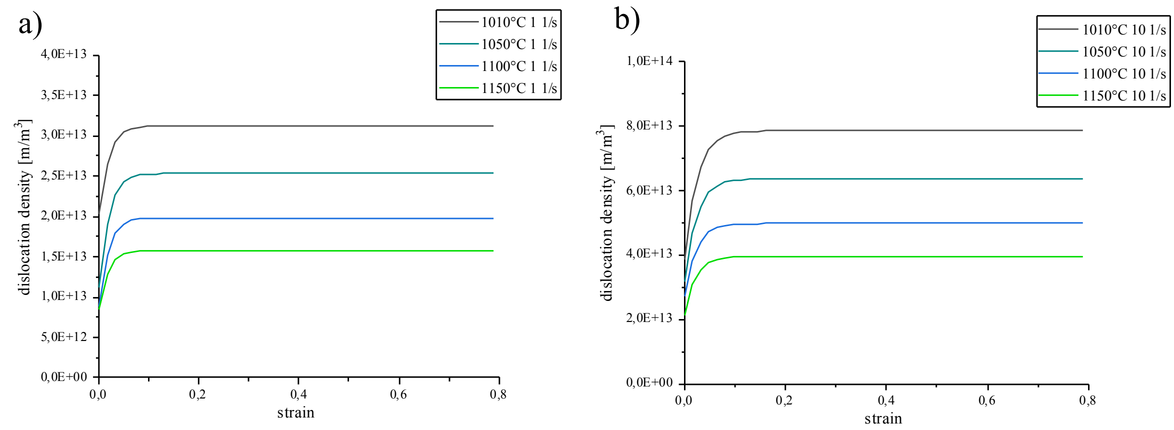

Figure 63: Modelled dislocation density for a strain rate of a) 1 1/s, b) 10 1/s.

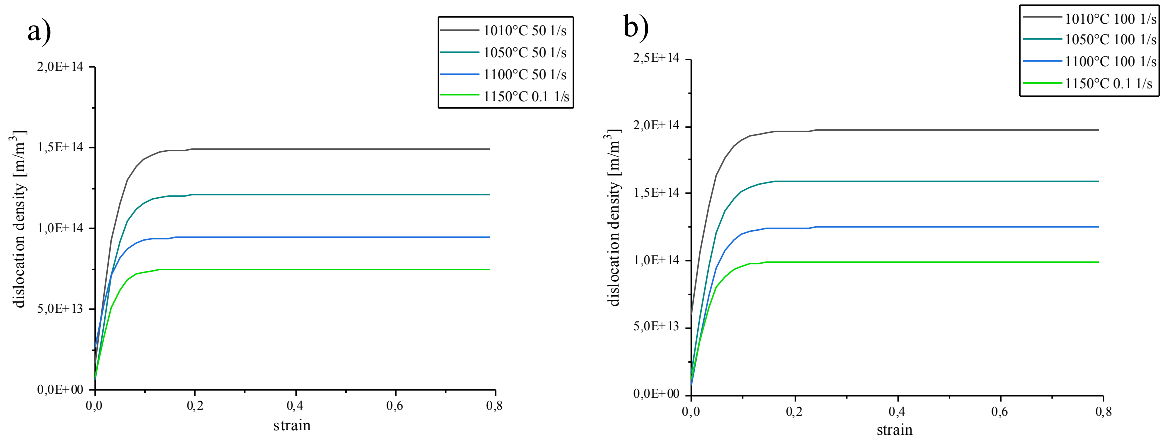

Figure 64: Modelled dislocation density for a strain rate of a) 50 1/s, b) 100 1/s.

4.7. CDRX modelling

The evolution of hardening and the recovery coefficients *h_1* and *h_2* with strain rate and temperature for the model of continuous dynamic recrystallization is shown in Figure 65. The hardening coefficient *h_1* is independent of strain rate and temperature because the strain rate sensitivity m_{h_1} (compare eq. 29, Table 12) was fitted to a value of zero. The recovery coefficient *h_2* rises for low strain rates and also shows a small increment for higher temperatures.

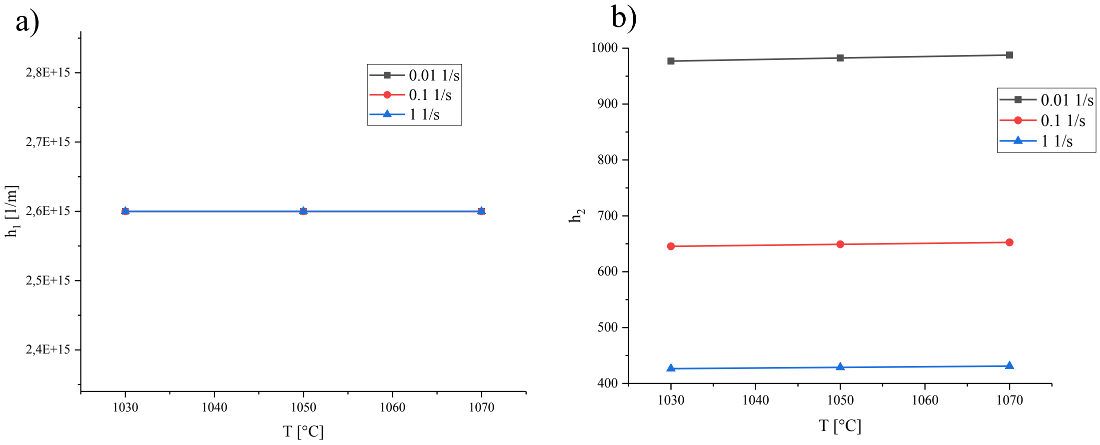

Figure 65: Evolution with strain rate and temperature of a) h_1 hardening and b) h_2 recovery coefficients<.

The model of continuous dynamic recrystallization was able to reproduce the flow stress values of Ti64 in the β field for different strain rates and temperatures up to high strains, see Figure 66 and Figure 67.

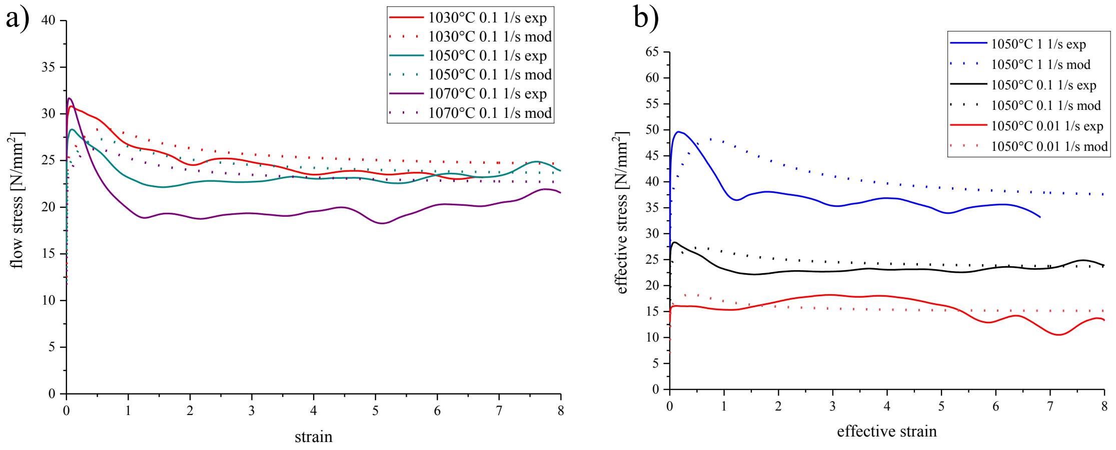

Figure 66: Modelled flow stress, a) for different temperatures, b) for different strain rates.

In a first approach, the peak of the experimental curve up to a strain of 1 was intended to be fit, giving unreasonable results regarding the microstructure, i.e. reaching of a steady state for the different internal variables at very low strains. In a second approach, the adjustable parameters were changed so that the modelled flow curve resembled the experimental curve regarding the value of the peak stress and the amount of softening proceeding to the maximum flow stress. The amount of softening was well described by the model for the strain rates 0.1 and 0.01 1/s, whilst for a strain rate of 1 1/s the amount of softening is too little compared to the experimental curves, see Figure 67.

The evolution with strain of the different types of stresses, that contribute to the total flow stress, can be seen in Figure 68. The effective stress remains constant for the whole deformation, while the large contribution of the athermal stress decreases slowly from an initial peak value. The stresses from the Hall-Petch contribution are in the same magnitude as the effective stress. While the stress from the grain size reaches a constant value at strains of 1.5, the stress from the subgrain size reaches a peak at strain 0.6 and decreases in the following.

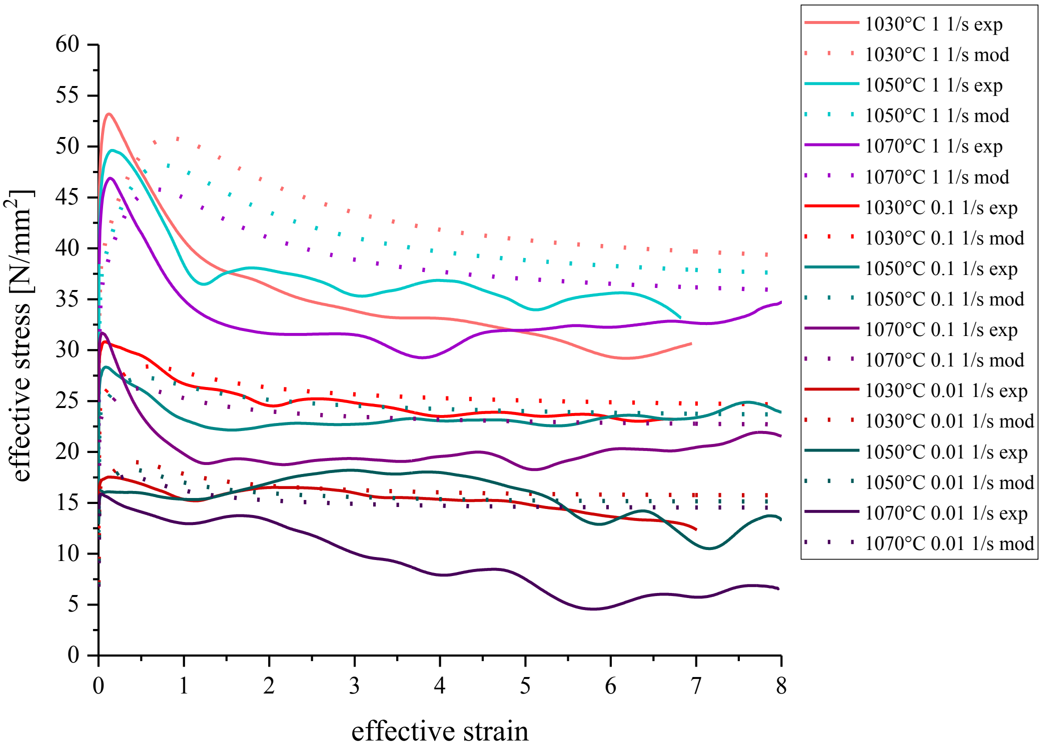

Figure 67: All modelled flow stresses with the CDRX model.

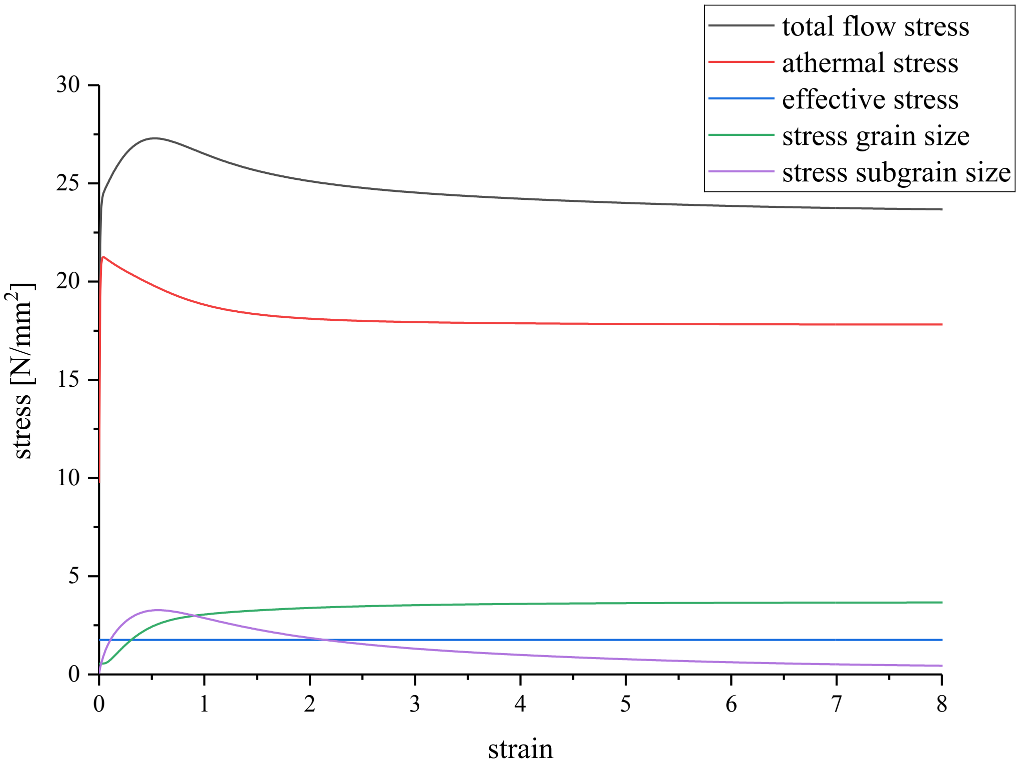

Figure 68: Modelled evolution of different stresses for 1050°C 0.1 1/s.

The model also describes the evolution of the microstructure during deformation. Figure 69 shows different types of dislocation densities for a deformation at 1050°C with 0.1 1/s strain rate. While the mobile and the immobile dislocation density remain mainly constant, the total dislocation density evolves with the wall dislocation density. A strong increase until a peak value at strain 0.6 is followed by a dropping behaviour for both these dislocation densities. Figure 70 compares the evolution of the total flow stress with the evolution of the total dislocation density for different strain rates and temperatures.

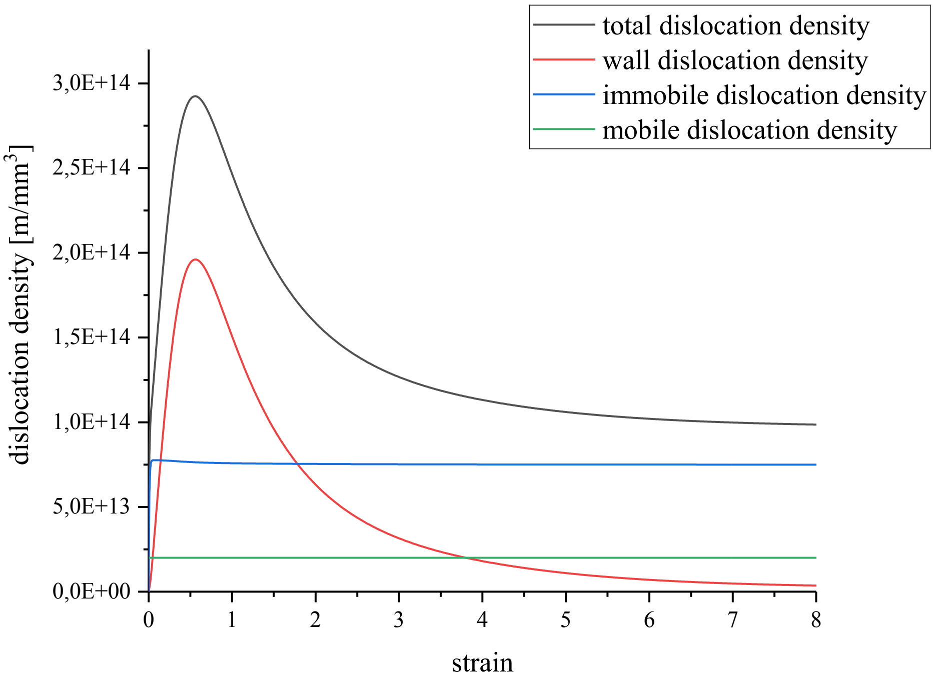

Figure 69: Modelled evolution of different dislocation densities 1050°C 0.1 1/s.

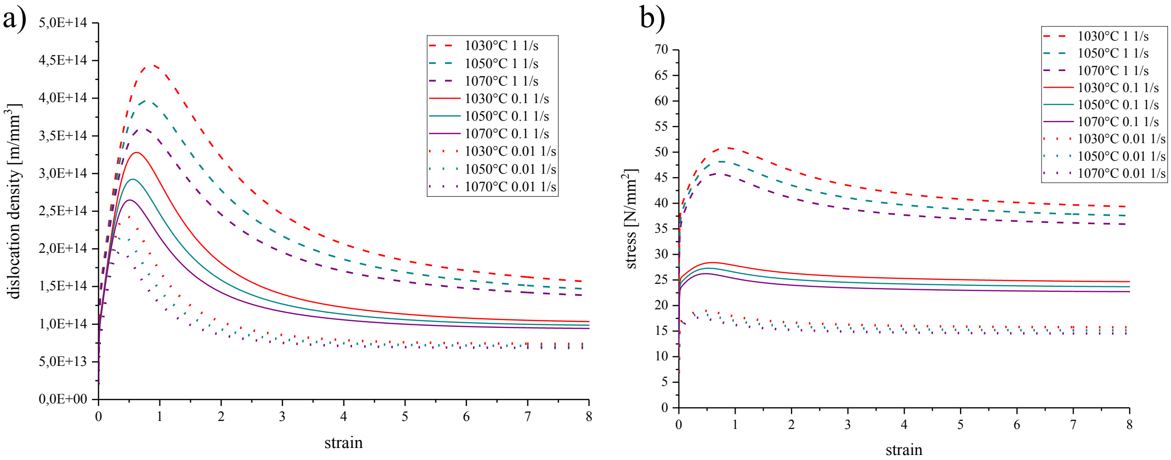

Figure 70: Modelling results for a) total dislocation density, b) total flow stress.

The model also delivers information about the fraction of high and low angle boundaries and the size of grains and subgrains. The fraction of HABs increases with the same rate, as the fraction of LABs decreases (Figure 71). For low strain rates and high temperatures f_{HAB} reaches faster a value around the maximum of 1 and f_{LAB} a value around the minimum 0. In the range of performed simulations the effect is more pronounced for different strain rates, than for different temperatures, see Figure 72 and Figure 73.

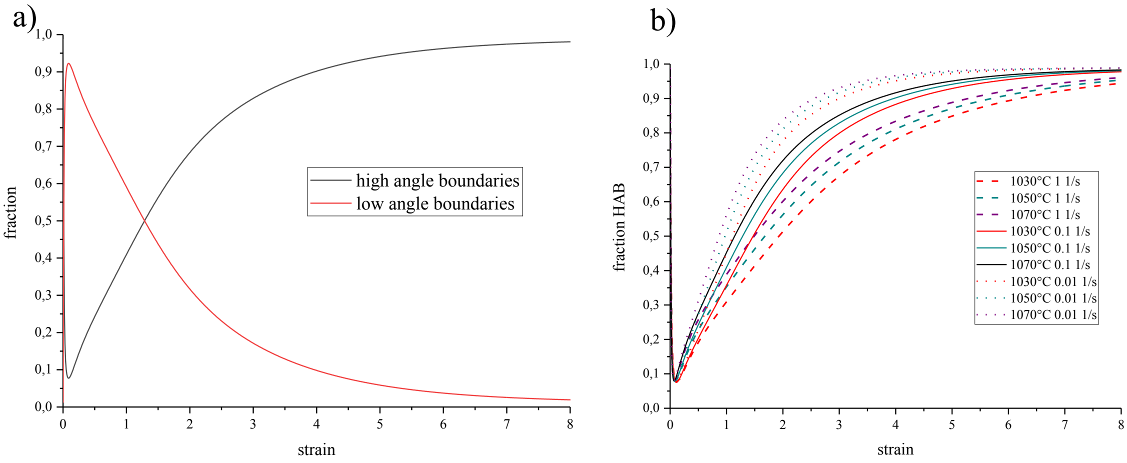

Figure 71: a) evolution of the fraction of HAB and LAB for 1050°C 0.1 1/s, b) evolution of f_{HAB} for different strain rates and temperatures.

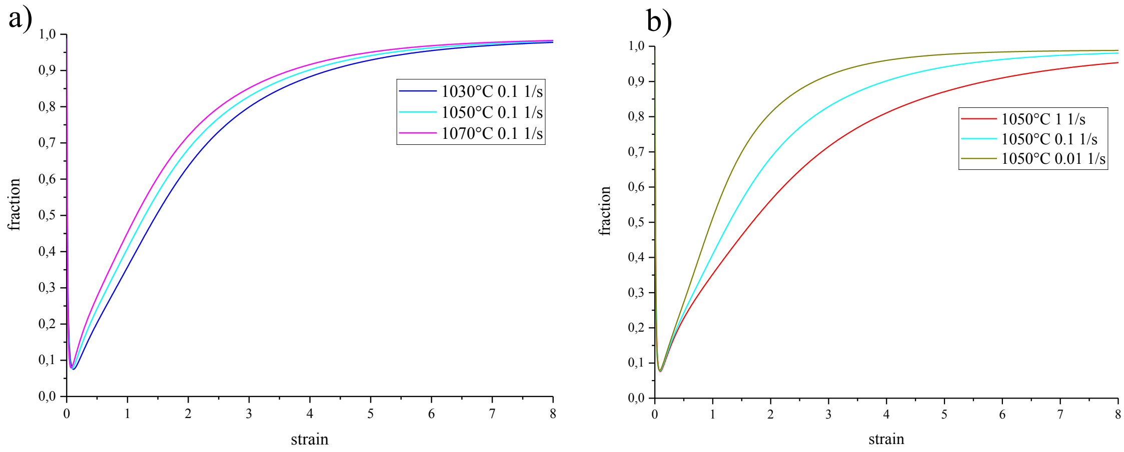

Figure 72: Modelled evolution of the fraction of HAB a) for different temperatures, b) different strain rates.

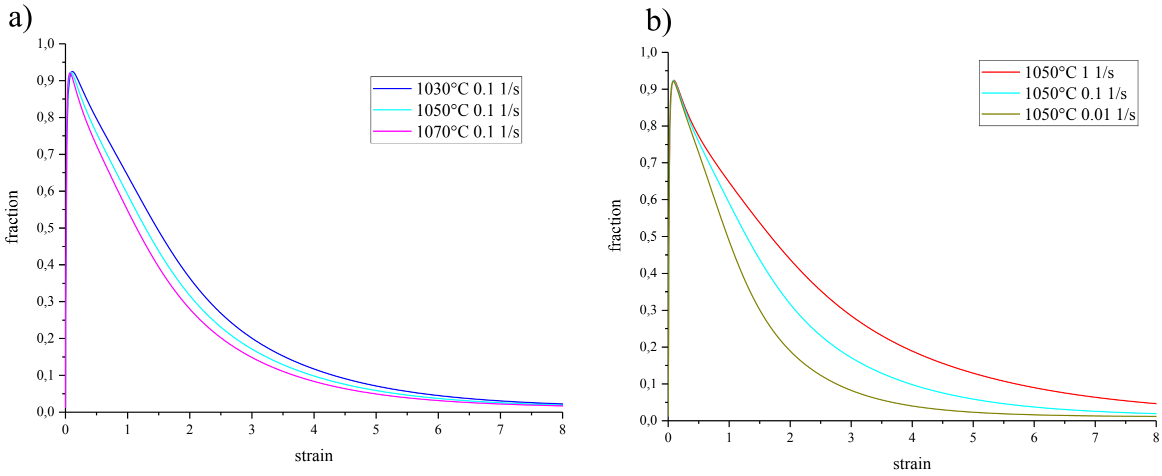

Figure 73: Modelled evolution of the fraction of LAB a) for different temperatures, b) different strain rates.

According to the model input, that assumes an initial recrystallized state, the grain size and the subgrain size start from the same initial value, see Figure 74 for 1050°C 0.1 1/s. While the grain size decreases and saturates at values between 7-20 µm, the subgrain size reaches a minimum at strains between 0.5-1 and saturates at values about 5-18 µm, for comparison see Figure 75 and Figure 76. Both grain size and subgrain size saturate at larger values for lower strain rates and higher temperatures.

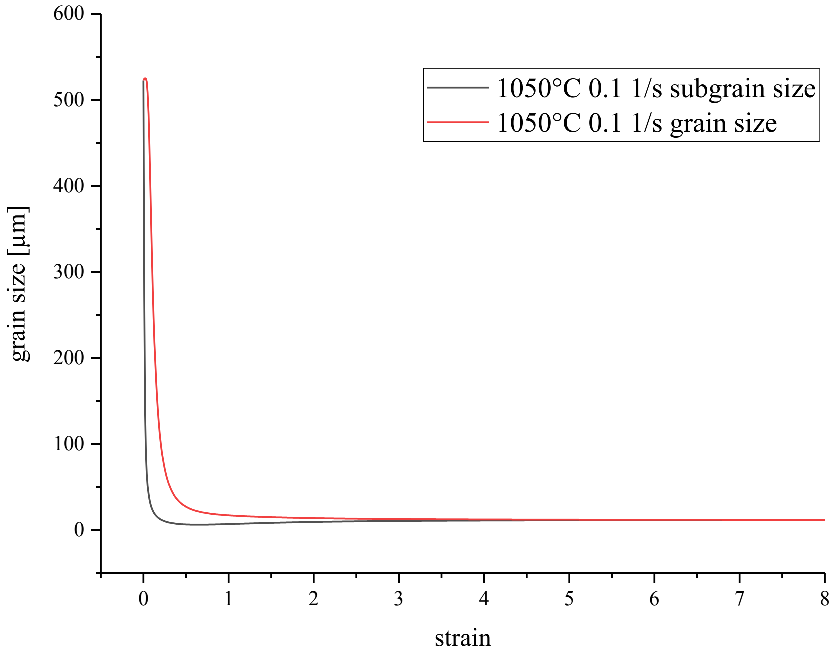

Figure 74: Modelled evolution of grain size and subgrain size for 1050°C 0.1 1/s.

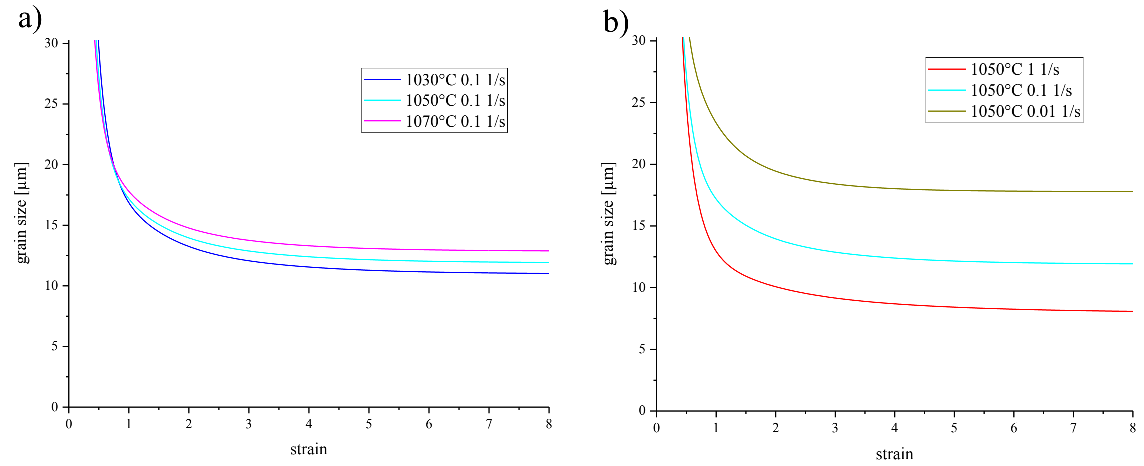

Figure 75: Modelled evolution of grain size, a) for different temperatures, b) for different strain rates.

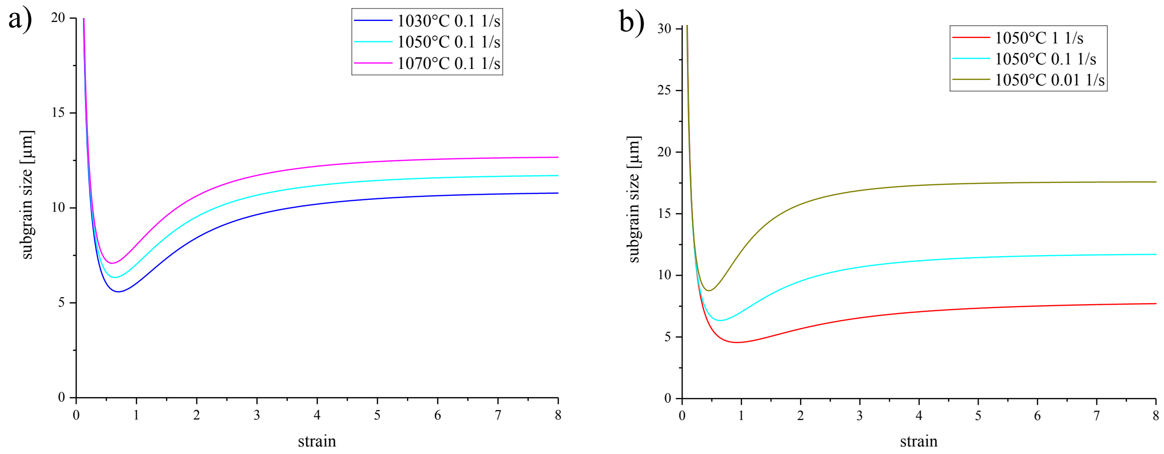

Figure 76: Modelled evolution of subgrain size, a) for different temperatures, b) for different strain rates.

5. Discussion

5.1.Modelling

The essential difference between the Kocks Mecking and the CDRX model causing their varying output is the respective description of the microstructure. The model of Kocks and Mecking assumes that the effects of different features of the microstructure are negligible. Basically, the microstructure model does not consider grain boundaries (low or high angle), therefore dislocations are not hindered or influenced by Hall-Petch effects.

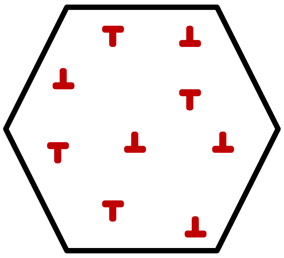

Figure 77: Sketch of a microstructure as assumed for the Kocks Mecking model with one kind of dislocations and neglible contribution of grain boundaries, i.e. one infinite large grain.

Another limitation of the model is the use of solely one kind of dislocation density. Dislocations in the Kocks Mecking model are isolated and all cause the same strain field in the microstructure, so no dipoles or immobile dislocations are considered. The evolution of dislocation density in this model only considers the production and the evolution by two phenomenological expressions, meaning dislocations are either produced or annihilated, but no interactions with other dislocations or features of the microstructure are considered. This principally means, that the model does not distinguish between dynamic recovery and dynamic recrystallization, because dislocations are produced and reduced dynamically during the deformation process without further illumination of the mechanism.

In the model of CDRX the microstructure description is more detailed than in the Kocks Mecking model, also allowing the description of more sophisticated processes happening in the microstructure. As the model distinguishes not only mobile and immobile dislocations, but also divides the latter in wall dislocations and immobile dislocations within the grains, the evolution of these different kinds of dislocations can be analysed separately. The whole process of CDRX may only be modelled through these descriptions of the dislocation density evolutions. The description of microstructure and the modelled process of CDRX are illustrated in Figure 78. The activation of the movement of dislocations and the sliding of dislocations is accounted for by the different stress contributions.

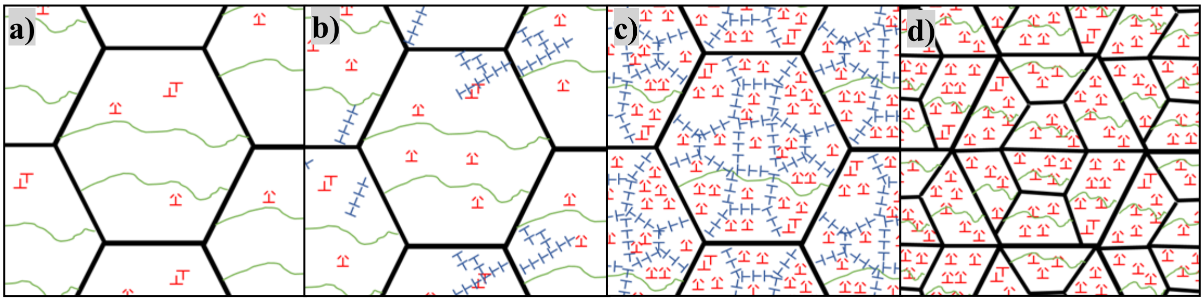

Figure 78: Microstructure evolution with strain and process of CDRX. a) initial, b) formation of LAB, c) large amount of newly formed LAB, d) transformation of LAB to HAB. Immobile dislocations and dipoles are marked in red, mobile dislocations in green and wall dislocations in blue. Modified from a scheme by Buzolin.

Even though these major advancements compared to the Kocks Mecking model, the present model has its limitations. The model does not consider texture. This is a drawback, because some hot forming processes cause the evolution of texture in the microstructure, as reported by Yapici et al. for deformation of Ti64 by equal channel angular extrusion at 800°C [49]. Although a function for the Taylor factor as a function of strain taken from the literature was implemented, further research should be done on this aspect. Also, heterogeneous deformation causing a gradient in grain size within one sample, like observed for hot torsion experiments before [50], cannot be modelled with the present set-up.

The yield stress function of the model, that is derived from experimental hot compression values, needed modification for modelling the hot torsion flow curves by introduction of the factor f_{YS}. A physical description of differences in yielding for different starting microstructures should therefore be incorporated into the model.

Two other assumptions of the model, that limit its application, are the equal distribution of stresses and the pure viscoplastic behaviour, neglecting elastic strains. The former is important for modelling of deformation processes under conditions favouring the occurrence of flow instabilities and flow localizations.

A comparison of the two differently modelled flow curves up to moderate strains with the corresponding experimental curve can be seen in Figure 79. The predicted flow stress between strains of 0.4 and 0.8 is very similar for both models, while the initial flow stress differs. The Kocks Mecking model is suitable for describing deformations up to moderate strains. The first increase in flow stress is similar for the experimental compression and the modelled curve. However, the Kocks Mecking model fails to describe the flow stress softening. The CDRX model can predict this behaviour, e.g. see Figure 67. However, the exact amount and evolution of this flow softening cannot be caught by this model as well. Additionally, the sharp increase in stress at the beginning of the flow curve cannot be modelled with the CDRX model to a satisfying level. Comparing Figure 68 and Figure 69 this characteristic seems to be related to the modelled evolution of the wall dislocation density. As ρ_w reaches its maximum value, also the total dislocation density and the total flow stress show a peak. With the present setting, wall dislocations form too slow to predict the hardening behaviour in the beginning of the flow curve accurately, which is most likely related to the hardening coefficient h_1.

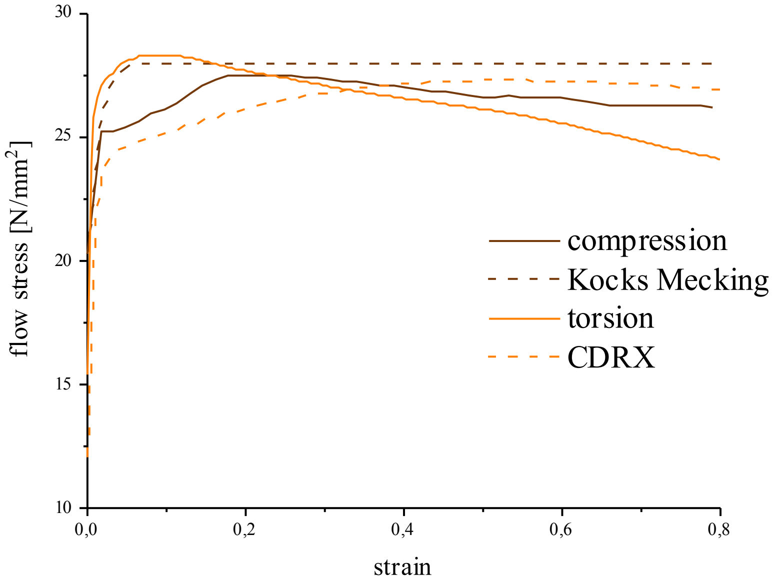

Figure 79: Flow stress modelling results for Kocks Mecking and CDRX during a deformation at 1050°C and 0.1 1/s for compression and torsion modes.

Regarding the total dislocation density, the differences of the two models are clearly visible, see Figure 80. The dislocation density generated as an output by the Kocks Mecking model reaches a steady state at low strains. The total dislocation density for the CDRX model reaches a maximum at strains ~1 then it decreases and reaches a steady state at strains ~7 for 1050°C 0.1 1/s. This evolution of the total dislocation density also indicates, that microstructural changes occur up to large strains, which is not shown by the Kocks Mecking model. The difference in steady state total dislocation density for both models is a factor of 10. This can be explained by the different strain fields attributed to the dislocations in the two models. In the Kocks Mecking model the dislocations are considered to be isolated, hence having a larger strain field than the dislocations in the CDRX model. The factor for the wall dislocation density f_{ρ_w} used in the calculation for τ_{ath} considers just this effect of a different strain field caused by the wall dislocations compared to mobile and interior immobile dislocations. Therefore, the Kocks Mecking model needs less dislocations to account for the same stress value.

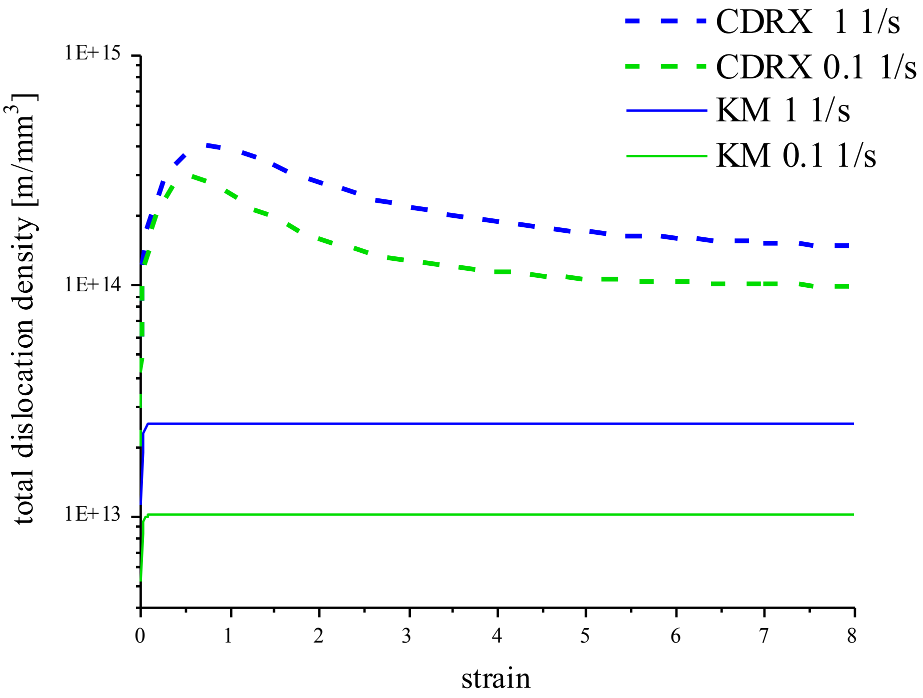

Figure 80: Total dislocation density during deformation at 1050°C at two different strain rates (1 and 0.1 1/s) calculated using Kocks Mecking and CDRX models.

A drawback for both models is the dependency on the phenomenological expressions for the hardening and the recovery coefficients $h_1$and h_2. While most other parameters, needed to be adjusted for the modelling, are fitted within a plausible range for the parameter, there are no limitations for these two coefficients, because no physical meaning has been attributed to them. However, the fitting of $h_1$and h_2 is also influenced by finding reasonable values for the strain rate sensitivity and the activation energy. In the CDRX model both activation energies $Q_{h_1} = 1.6\ \mathrm{kJ/mol}$ and $Q_{h_2} = 13.8\ \mathrm{kJ/mol}$ do not fulfil this criterion (activation energies in the β field are reported to be between 210-285 kJ/mol [51], [52]), but it has to be noted that the value for Q_{h_1} is freely convertible due to fitting m_{h_1} to a value of zero. The sole information of the used phenomenological expressions for h_1 and h_2 is that e.g. hardening is favoured at low temperatures and high strain rates. This effect, that was observed experimentally in terms of microstructural evolution, corresponds to the formation of dislocations and less mobility in annihilation. Still, there is no information about the mechanism of such production. The difference for $h_{1,0}$ is large between the two models, see Table 13. As especially the CDRX model includes several parameters, that were estimated within a certain range, some kind of difference between the coefficients was expected from the beginning. Also, due to the different concepts of the two models, the meaning of h_1 and h_2 in the context of microstructural evolution is most likely to be different, hence justifying different values. Regarding the evolution of the two coefficients with strain rate and temperature (compare Figure 58 and Figure 65) similar tendencies were found for the recovery coefficient. h_2 increases for high temperatures and low strain rates, indicating that recovery processes are facilitated for these experimental conditions, which is the expected tendency. In the Kocks Mecking model the hardening coefficient h_1 increases inversely to h_2. For the model of CDRX the hardening coefficient is independent of both temperature and strain rate, due to fitting the strain rate sensitivity to a value of zero. Similar behaviour for this coefficient was also reported in the literature. [25]

Table 13: Comparison of initial values of hardening and recovery coefficient in Kocks Mecking and CDRX model.

Kocks Mecking model	$h_{1,0}$	$8.08\cdot10^{7}\,\mathrm{m}^{-1}$
	$h_{2,0}$	469
CDRX model	$h_{1,0}$	$26\cdot10^{14}\,\mathrm{m}^{-1}$
	$h_{2,0}$	570

5.2. Phenomena during plastic deformation at high temperature and large strain

To validate the modelled evolution of the microstructure the metallography data of selected samples from the hot torsion tests can be consulted. Regarding the samples deformed in the α+β field, the large amount of martensitic grains in the microstructure allow the assumption that most of the microstructure at 950°C and 970°C consisted of β phase. Also, particles of globular α indicate the presence of α during deformation. For the samples heat treated in the β field to obtain a lamellar structure, no globular α was observed. The α phase in these samples is visible in the fine lamellae and at the prior β grain boundaries, see Figure 52 and Figure 53. During torsion these α features may be broken. As the α phase of titanium is harder than the β phase [8] the flow stress is expected to increase when such a feature of α phase is broken. The flow curves obtained for the lamellar structures show exactly that characteristic, see Figure 42. The several bumps observed in the stress values indicate that new α phase influences the flow behaviour of the material. As new α grows at the β grain boundaries it may be broken again during deformation, but also effects of texture and the rotation of α phase may play a role. In all cross sections of the samples deformed in the α+β field grains get refined with increasing torsion radius, a characteristic that was observed for torsion samples of Ti64 before [53] and can easily be explained by the deformation gradient within the torsion samples.

The deformation in the β field also shows refined grains close to the sample surface, even though the gradient of grain size is not as pronounced in the β field as for the α+β field. This fact suggests, that grain growth in the β field is very fast, which was also reported in the literature especially for the first 15 minutes of a β field heat treatment. [54]

For low strain rates (0.01 1/s) the cross sections showed a fully recrystallized microstructure, see Figure 56. Also, microstructures for the higher strain rates 0.1 and 1 1/s show recrystallized grains, but to a smaller amount. This corresponds very well with the modelled results. As during the proceeding of CDRX the amount of HABs increases by a constant conversion of LABs into HABs, the fraction of HABs can be used as a sign of the grade of recrystallization. Figure 81 indicates, that for a strain rate of 0.01 1/s a nearly fully recrystallized microstructure is obtained at strains ~5, while for a strain rate of 1 1/s the recrystallized state is not reached at a strain of 8, like present for the investigated samples.

The reason for this effect can be found in the evolution of the dislocation densities. As the strain rate is directly included in the expression for the production term of dislocations, more dislocations form for high strain rates. This means, that also the peak value of the total dislocation density is reached at a later stage and the successive decrease in dislocation density will reach a steady state at a larger strain compared to the deformation at a lower strain rate. The formation of a larger amount of dislocations at a strain rate of 1 1/s is also visible in the hardening regime in the beginning of the flow curve, that is more pronounced for the higher strain rate, see Figure 44. Both the larger amount of dislocations and reaching the maximum at higher strains influence the modelling of the flow softening.

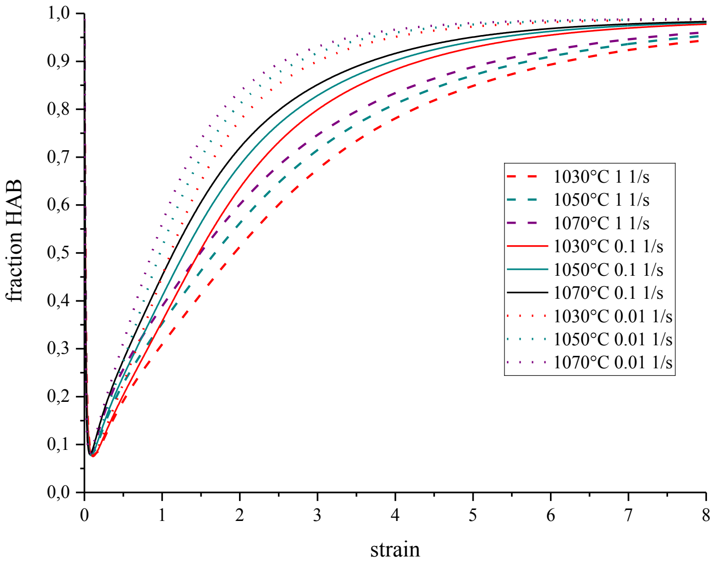

Figure 81: Modelled fraction of HABs for different strain rates and temperatures in the β field.

The dominant role of recovery processes and the transformation of LAB into HAB at larger strains explain the observed softening in all flow curves. The higher amount of softening i.e. the increased recovery processes for dislocations at higher strain rates can be correlated to the more pronounced hardening preceding the softening for these deformation conditions.

The existence of a substructure and subgrain boundaries could not be evidenced for Ti64 with standard equipment due to the formation of a martensitic microstructure upon quenching. However, within some very large grains the substructure in the former β grains can be vaguely suspected. The martensite within these grains is not exactly parallel, but changes its direction slightly within the grains, i.e. from subgrain to subgrain, see Figure 57 for illustration.

The size of grains after deformation as an output of the CDRX model can be compared to the experimentally obtained grain sizes. The model predicts for the fully recrystallized microstructure at 0.01 1/s grain sizes with average diameters of 16-19 µm for 1030-1070°C, see Figure 82. Even though the difference in grain size between the different temperatures at strain rate 0.01 1/s seems relatively smaller as predicted, the experimentally obtained grain sizes are a lot larger with a diameter around 100-150 µm, see Figure 83.

It has to be noted, that the gradient in grain size within the torsion samples is not considered in the model, still also the smallest grains are much larger than the predicted values. This means, that the function for the grain size directly before deformation in the β field needs to be adapted and other effects like diffusional processes, that facilitate grain growth, should be considered to give more plausible results.

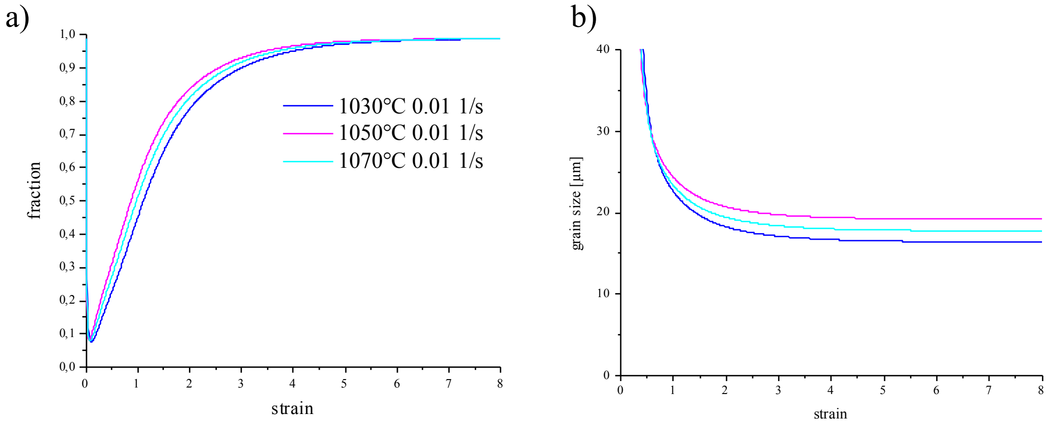

Figure 82: CDRX model results for strain rate 0.01 for different temperatures, a) fraction of HAB, b) grain size.

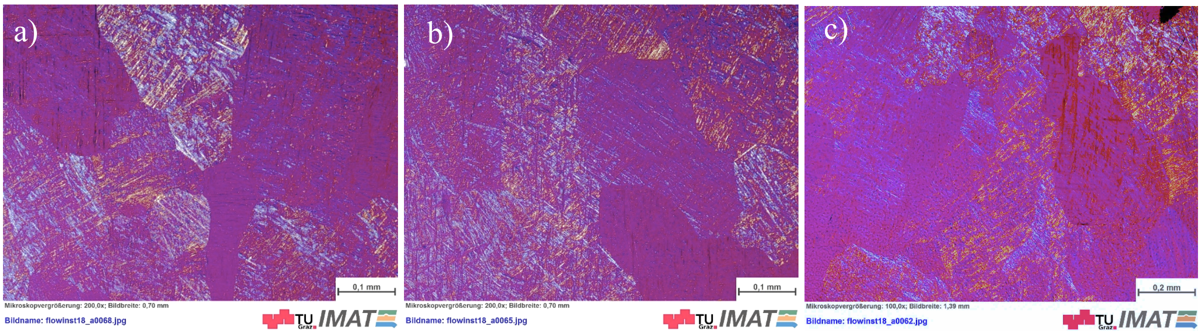

Figure 83: 0.01 1/s strain rate, bottom center. a) 1030 °C, b) 1050°C, c) 1070°C.

5.3. Experimental methods

A large factor of uncertainty during hot torsion experimental procedures is the measurement of temperature. The temperature profile in Figure 10 shows clearly that there is a temperature gradient within the sample even without deformation. The temperature in the Gleeble® can only be controlled via one thermocouple, meaning no temperature adjustment is possible on other parts of the sample during deformation. Furthermore, as the sample diameter increases during deformation also the cross section increases, reducing the temperature. A temperature correction for hot torsion data to receive isothermal flow curves, as they are assumed for both models, would need to consider all these effects. Regarding the effect of the temperature correction performed for the hot compression curves, the effect may be large especially for high strain rates and low temperatures. Analysis of the microstructure verifies the considerations made about the temperature gradient within the sample. The distribution of α particles in the samples deformed at 950°C and 970 °C shows decreasing globular α in direction of the centre, thus indicating larger temperatures in the centre of the sample. In the β field the samples show different grain sizes along the centreline of the sample, namely largest grains in the very centre of the sample.

Still, attempts should be made to correct experimental flow curves for e.g. deformation heating. Also, an increment in temperature within the sample may cause the transformation of α into β phase and thereby a reduction in flow stress. It needs to be considered, that while the measured flow stresses can be corrected, the obtained microstructure cannot.

Another problem during the torsion tests at the Gleeble® was the misalignment of the quenching system. After deformation the samples were not quenched equally fast from all sides. This caused a gradient in the internal stresses of the sample and forced the sample to bend after losing the fixation of the sample holder, see Figure 13. A metallographic comparison of the bend (top centre) and the contracted side (bottom centre) showed no differences between both sides. The flow curve data is not affected by this problem, because torsion is finished before the quenching starts.

Additionally, other effects influence the experiment and the measured data, namely any irregularities during the experiments (e.g. bad contact of thermocouple), inhomogeneities in the material or oxide layer formation during the experiment, which cannot be avoided as the test chamber of the Gleeble® is not perfectly sealed. Generally, it can be said, that for moderate strain rates the experimental data is more accurate, because for very low or very high strain rates experimental conditions are more difficult to control and so irregularities in the data are more frequently. This is especially problematic as the model assumes perfect conditions for every strain rate.

Despite all the irregularities occurring during the experimental procedure, similar results for flow curves can be obtained by torsion and compression, see Figure 84. Hot deformation tests performed at different locations, with different material batches and even via different experimental procedures gave comparable results regarding the flow stress for moderate strains.

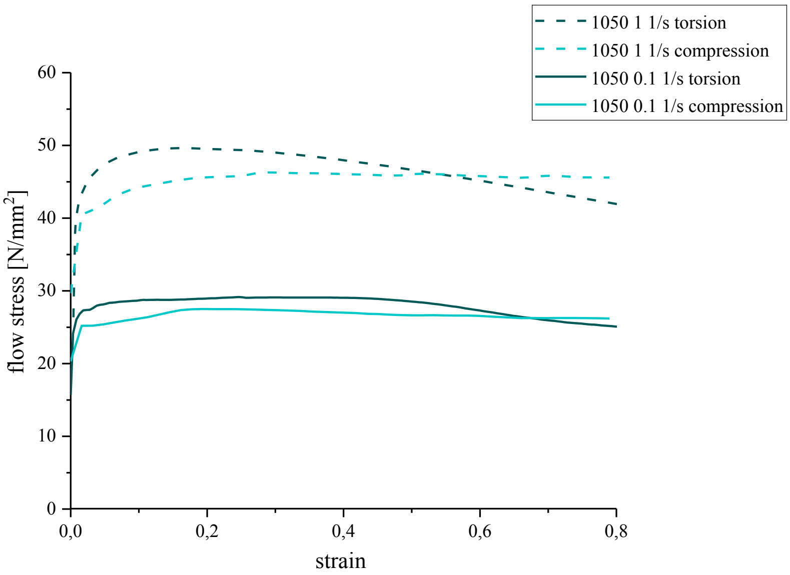

Figure 84: Comparison of experimental torsion and compression flow curves for deformations at 1050°C and strain rates of 1 and 0.1 1/s.

6. Summary and conclusions

The model by Kocks and Mecking was successfully set up for the titanium alloy Ti64. The modelling results were validated with experimental hot compression flow curves from hot compression that were corrected for deformation heating. For moderate strains up to 0.8, the Kocks Mecking model is well suited to describe the deformation behaviour of Ti64. Both the modelled flow stress and the dislocation density saturate at low strains. The steady state extends to large strains, so the model is limited to low grades of deformation.

The model of continuous dynamic recrystallization is based on a more detailed evolution of microstructure, that allows to describe also the metallurgical phenomena occurring up to large strains. Flow stresses up to strains of 8 were successfully modelled assuming CDRX and validated with experimentally obtained hot torsion flow curves in the β field of Ti64. Beside the flow stress, the model also predicts the evolution of the microstructure by describing the evolution of grain sizes and dislocation densities. While the tendencies for different experimental conditions were modelled, certain features of the flow curve and the microstructure were not accurately described by the modelling results. This leaves the assumption that the process of CDRX is likely to occur in Ti64 for a high degree of deformation, but not all happening mechanisms are yet described by the investigated model.

Despite the diversity in output parameters of the model for CDRX, regarding the flow stress prediction for moderate strains the Kocks Mecking model delivers more accurate results. The simplicity of this model allows a quick set-up, while for the CDRX model the effort for adjusting all required parameters is larger, but so is the output. A summary of the input and output of both models is depicted in Figure 85.

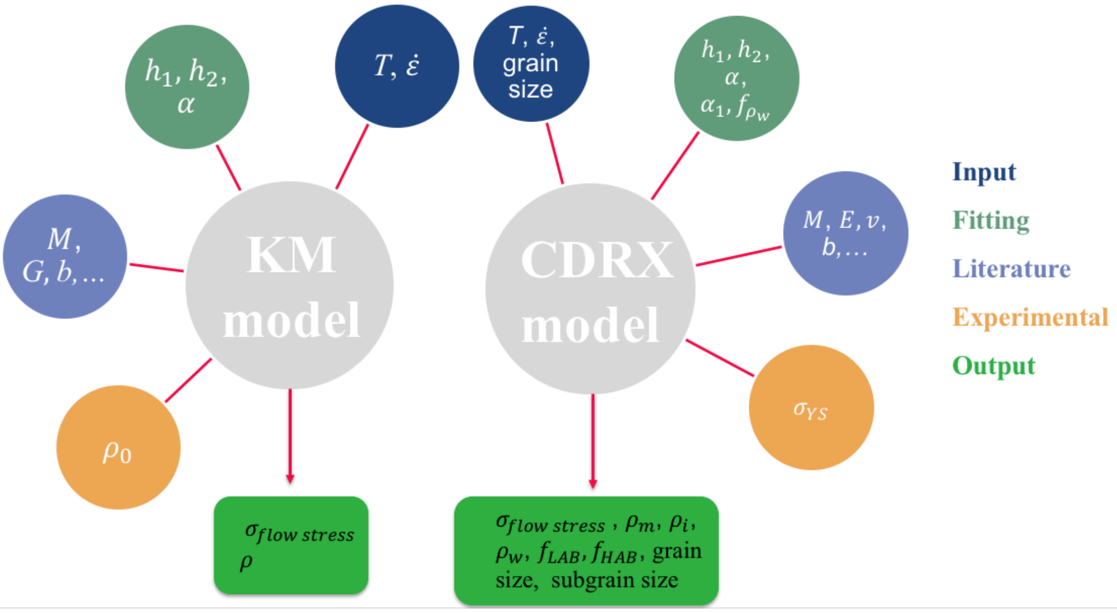

Figure 85: Summary of Kocks Mecking model and model for continuous dynamic recrystallization.

Concluding it has to be added, that however large the accuracy of the description of metallurgical phenomena in a model is, there will always be differences to the error-prone processes in reality. However, flow models are a useful tool to correlate microstructural characteristics with macroscopic properties. Using these models, one has to keep in mind, that the quality of a physically-based model rises with the description and the knowledge about the material’s microstructure.

7. Outlook

Future research on the topic of this master's thesis is suggested in several aspects. Regarding the experimental procedure for hot torsion on the Gleeble®, the existing quenching system should be modified to allow homogenous quenching of the whole sample. Also, it is advised to perform future tests in a properly sealed testing chamber to reduce the amount of oxides forming during the experiment and to aim for reducing the temperature gradient within the sample e.g. by using different heating sources. For the torsion data a way to consider different changes in temperature during deformation is desired.

In view of the modelling both the Kocks Mecking and the CDRX model should be extended to the α+β field of Ti64 to allow deformation prediction in a wider field of temperature. This can be done e.g. by considering a rule of mixture for the different phases.

To get further insight into the restoration mechanisms of Ti64 at large strains during hot deformation, a close investigation of the martensitic structure would be of great interest. A special analysis of the martensitic EBSD pattern as used by Poletti et al. [18] may be used to reconstruct β phase in the alloy before quenching. In this way the existence and distribution of subgrains may be revealed, which may help to better understand the microstructural evolution.

8. References

[1] G. Lütjering and J. C. Williams, *Titanium*. New York: Springer-Verlag Berlin Heidelberg GmbH, 2003.

[2] J. Porntadawit, V. Uthaisangsuk, and P. Choungthong, “Modeling of flow behavior of Ti-6Al-4V alloy at elevated temperatures,” *Mater. Sci. Eng. A*, vol. 599, pp. 212–222, 2014.

[3] A. S. Khan, Y. S. Suh, and R. Kazmi, “Quasi-static and dynamic loading responses and constitutive modeling of titanium alloys,” *Int. J. Plast.*, vol. 20, no. 12, pp. 2233–2248, 2004.

[4] X. G. Fan and H. Yang, “Internal-state-variable based self-consistent constitutive modeling for hot working of two-phase titanium alloys coupling microstructure evolution,” *Int. J. Plast.*, vol. 27, no. 11, pp. 1833–1852, 2011.

[5] S. M. Wei Sha, *Titanium alloys: modelling of microstructure, properties and applications*, First. Cambridge: Woodhead Publshing Limited, 2009.

[6] S. L. Semiatin, S. L. Knisley, P. N. Fagin, D. R. Barker, and F. Zhang, “Microstructure evolution during alpha-beta heat treatment of Ti-6Al-4V,” *Metall. Mater. Trans. A*, vol. 34, no. 10, pp. 2377–2386, 2003.

[7] A. Majorell, S. Srivatsa, and R. C. Picu, “Mechanical behavior of Ti-6Al-4V at high and moderate temperatures - Part II: Constitutive modeling,” *Mater. Sci. Eng. a-Structural Mater. Prop. Microstruct. Process.*, vol. 326, no. 2, pp. 306–316, 2002.

[8] E. W. C. R. Boyer, G. Welsch, *Materials Properties Handbook: Titanium alloys*, Forth prin. Materials Park, OH 44073-7586: ASM International, 2007.

[9] J. G. Malcor, “Mechanical and Microstructural Behaviour of Ti-6Al-4V Alloy in the Hot Working Range,” *Titanium, Sci. Technol.*, pp. 1495–1502, 1985.

[10] C. J. Bennett, S. B. Leen, E. J. Williams, P. H. Shipway, and T. H. Hyde, “A critical analysis of plastic flow behaviour in axisymmetric isothermal and Gleeble compression testing,” *Comput. Mater. Sci.*, vol. 50, no. 1, pp. 125–137, 2010.

[11] H. J. M. and J. J. Jonas, *Metal Forming-Interrelation Between Theory and Practice*. Ohio: Plenum Press, New York, 197 t., 1971.

[12] J. Fields, D. S. and W. A. Backofen, “Determination of strain-hardening characteristics by torsion testing,” *ASTM Proc.*, vol. 57, p. 1259, 1957.

[13] G. R. Canova, S. Shrivastava, J. J. Jonas, and C. G’Sell, “The use of Torsion Testing to Asses Material Formabilty,” *Formability Met. Mater.*, pp. 189–210, 1982.

[14] S. Khoddam and P. D. Hodgson, “Conversion of the hot torsion test results into flow curve with multiple regimes of hardening,” *J. Mater. Process. Technol.*, vol. 153–154, no. 1–3, pp. 839–845, 2004.

[15] F. J. H. and M. Hatherly, *Recrystallization and Related Annealing Phenomen*, 2nd ed. Pergamon, 2004.

[16] S. Ion, S.E., Humphreys, F.J. and White, “Dynamic recrystallisation and the development of microstructure during the high temperature deformation of magnesium,” *Acta Met.*, vol. 30, no. 10, pp. 1909–1919, 1982.

[17] S. Gourdet and F. Montheillet, “A model of continuous dynamic recrystallization,” *Acta Mater.*, vol. 51, no. 9, pp. 2685–2699, 2003.

[18] C. Poletti, L. Germain, F. Warchomicka, M. Dikovits, and S. Mitsche, “Unified description of the softening behavior of beta-metastable and alpha+beta titanium alloys during hot deformation,” *Mater. Sci. Eng. A*, vol. 651, pp. 280–290, 2016.

[19] M. S. F. Warchomicka, Maria Cecilia Poletti, “Microstructural characterization of hot deformed Ti-6A1-4V,” *Ti 2011 - Proc. 12th World Conf. Titan.*, vol. 1, pp. 729–732, 2012.

[20] K. G. Guo X., Pettifor D., Kubin L, “Multiscale Materials Modelling,” *Mater. Sci. Eng.*

A, pp. 1–354, 2004.

[21] J. Störig, *Der Grosse Knaur, Band 3 - Lexikon*. Droemersche Verlagsanstalt, 1967.

[22] A. S. Khan, R. Kazmi, and B. Farrokh, "Multiaxial and non-proportional loading responses, anisotropy and modeling of Ti-6Al-4V titanium alloy over wide ranges of strain rates and temperatures," *Int. J. Plast.*, vol. 23, no. 6, pp. 931–950, 2007.

[23] A. S. Khan and R. Liang, "Behaviors of three BCC metal over a wide range of strain rates and temperatures: Experiments and modeling," *Int. J. Plast.*, vol. 15, no. 10, pp. 1089–1109, 1999.

[24] H. Mecking and U. F. Kocks, "Kinetics of flow and strain-hardening," *Acta Metall.*, vol. 29, no. 11, pp. 1865–1875, 1981.

[25] Y. Estrin, "Dislocation theory based constitutive modelling: foundations and applications," *J. Mater. Process. Technol.*, vol. 80–81, pp. 33–39, 1998.

[26] U. F. Kocks, "Laws for Work-Hardening and Low-Temperature Creep," *J. Eng. Mater. Technol*, vol. 98, no. 76–85, 1976.

[27] F. Roters, D. Raabe, and G. Gottstein, "Work hardening in heterogeneous alloys - a microstructural approach based on three internal state variables," *Acta Mater.*, vol. 48, no. 17, pp. 4181–4189, 2000.

[28] J.Kratochvíl, S.Libovický, "Dipole drift mechanism of early stages of dislocation pattern formation in deformed metal single crystals," *Scr. Metall.*, vol. 20, no. 11, pp. 1625–1630, 1986.

[29] D. S. Inc., *Torsion Operations Manual*. NY, 2017.

[30] R. Kapoor and S. Nemat-Nasser, "Comparison between high and low strain-rate deformation of tantalum," *Metall. Mater. Trans. A*, vol. 31, no. 13, pp. 815–823, 2000.

[31] R. Kapoor, J. B. Singh, and J. K. Chakravartty, "High strain rate behavior of ultrafine-grained Al-1.5 Mg," *Mater. Sci. Eng. A*, vol. 496, no. 1–2, pp. 308–315, 2008.

[32] R. L. Goetz and S. L. Semiatin, "The adiabatic correction factor for deformation heating during the uniaxial compression test," *J. Mater. Eng. Perform.*, vol. 10, no. 6, pp. 710–717, 2001.

[33] B. Song, S. Dong, B. Zhang, H. Liao, and C. Coddet, "Effects of processing parameters on microstructure and mechanical property of selective laser melted Ti6Al4V," *Mater. Des.*, vol. 35, pp. 120–125, 2012.

[34] R. Sethy, L. Galdos, J. Mendiguren, and E. Sáenz de Argandoña, "Friction and Heat Transfer Coefficient Determination of Titanium Alloys during Hot Forging Conditions ," *Adv. Eng. Mater.*, pp. 1–7, 2016.

[35] W.-S. Lee and C.-F. Lin, "Plastic deformation and fracture behaviour of Ti–6Al–4V alloy loaded with high strain rate under various temperatures," *Mater. Sci. Eng. A*, vol. 241, no. 1–2, pp. 48–59, 1998.

[36] F. Montheillet, D. Piot, N. Matougui, and M. L. Fares, "A critical assessment of three usual equations for strain hardening and dynamic recovery," *Metall. Mater. Trans. A Phys. Metall. Mater. Sci.*, vol. 45, no. 10, pp. 4324–4332, 2014.

[37] T. Seshacharyulu and B. Dutta, "Influence of prior deformation rate on the mechanism of b to a+b transformation in Ti6Al4V," *Scr. mater.*, vol. 46, pp. 673–678, 2002.

[38] S. Suri, G. B. Viswanathan, T. Neeraj, D. H. Hou, and M. J. Mills, "Room temperature deformation and mechanisms of slip transmission in oriented single-colony crystals of an α/β titanium alloy," *Acta Mater.*, vol. 47, no. 3, pp. 1019–1034, 1999.

[39] M. R. Moldover, J. P. M. Trusler, and T. J. Edwards, "Measurement of the Universal Gas Constant R Using a Spherical Acoustic Resonator," *Phys. Rev. Lett.*, vol. 60, no. 4, pp. 249–252, 1988.

[40] "JMatPro PRACTICAL SOFTWARE FOR MATERIALS PROPERTIES." [Online]. Available: https://www.sentesoftware.co.uk/jmatpro.

[41] S. how To, "Statistcs how to," 2018. [Online]. Available:

http://www.statisticshowto.com/rmse/. [Accessed: 29-May-2018].

[42] C. Poletti, R. Bureau, P. Loidolt, P. Simon, S. Mitsche, and M. Spuller, “Microstructure Evolution in a 6082 Aluminium Alloy during Thermomechanical Treatment,” *Materials (Basel).*, vol. 11, no. 8, p. 1319, 2018.

[43] P. Homporova, “Thermal history of alpha morphology in titanium alloy Ti-6Al-4V,” Technische Universität Wien, 2011.

[44] K. H. Chia, K. Jung, and H. Conrad, “Dislocation density model for the effect of grain size on the flow stress of a Ti-15.2 at.% Mo β-alloy at 4.2-650K,” *Mater. Sci. Eng. A*, vol. 409, no. 1–2, pp. 32–38, 2005.

[45] M. Semblanet-Helliere, “TRAITEMENT THERMOMECANIQUE DE L’ALLIAGE Ti17 : FORGEAGE EN α + β ET MAINTIEN POST-FORGEAGE EN β,” Ecole Nationale Supérieure des Mines Saint-Etienne, 2014.

[46] L. S. Tóth, A. Molinari, and O. Bouaziz, “Effective strain rate sensitivity of two phase materials,” *Mater. Sci. Eng. A*, vol. 524, no. 1–2, pp. 186–192, 2009.

[47] N. J. Hoff, “Approximate Analysis of Structures in the Presence of Moderately Large Creep Deformations,” *Q. Appl. Math.*, vol. 12, no. 1, pp. 49–55, 1954.

[48] C. H. Park, J. H. Kim, Y. T. Hyun, J. T. Yeom, and N. S. Reddy, “The origins of flow softening during higherature deformation of a Ti-6Al-4V alloy with a lamellar microstructure,” *J. Alloys Compd.*, vol. 582, pp. 126–129, 2014.

[49] G. G. Yapici, I. Karaman, and Z. P. Luo, “Mechanical twinning and texture evolution in severely deformed Ti-6Al-4V at high temperatures,” *Acta Mater.*, vol. 54, no. 14, pp. 3755–3771, 2006.

[50] B. Eghbali and M. Shaban, “Effect of Hot Torsion Parameters on Development of Ultrafine Ferrite Grains in Microalloyed Steel,” *J. Iron Steel Res. Int.*, vol. 19, no. 1, pp. 47–52, 2012.

[51] G. J. Tchein *et al.*, “Analytical modeling of hot behavior of Ti-6Al-4V alloy at large strain,” *Mater. Des.*, vol. 161, pp. 114–123, 2019.

[52] J. Luo, M. Li, H. Li, and W. Yu, “Effect of the strain on the deformation behavior of isothermally compressed Ti-6Al-4V alloy,” *Mater. Sci. Eng. A*, vol. 505, no. 1–2, pp. 88–95, 2009.

[53] H. Chen, F. Li, J. Li, X. Ma, J. Li, and Q. Wan, “Hardening and softening analysis of pure titanium based on the dislocation density during torsion deformation,” *Mater. Sci. Eng. A*, vol. 671, pp. 17–31, 2016.

[54] F. J. Gil and J. A. Planell, “Behaviour of normal grain growth kinetics in single phase titanium and titanium alloys 10_1016-S0921-5093(00)00731-0 Materials Science and Engineering A ScienceDirect_com,” vol. 283, pp. 17–24, 2000.

9. Appendix

Protocol of performed hot torsion tests

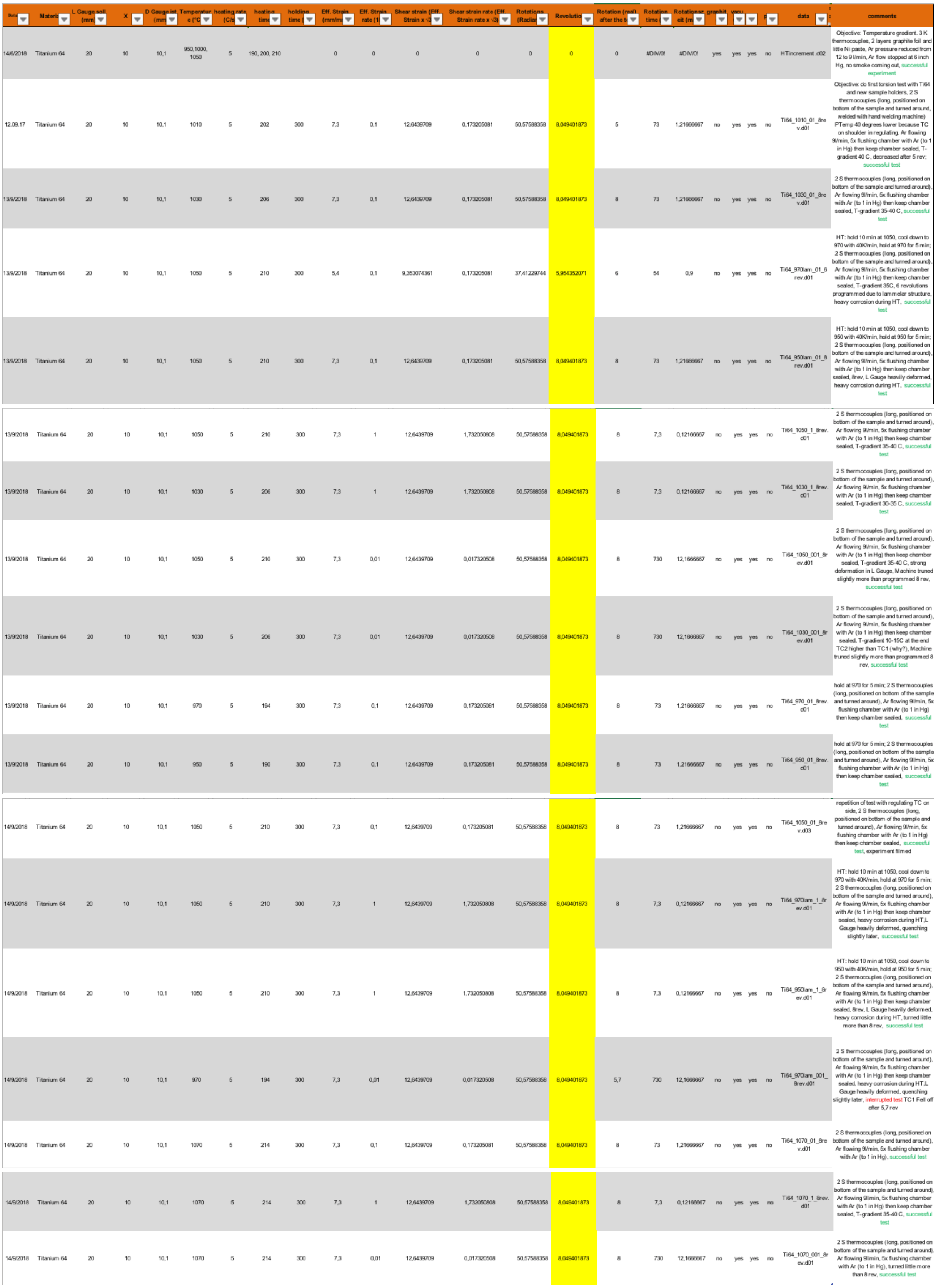

Datu	Materi	L Gauge soll (mm)	X	D Gauge ist (mm	Temperature (°C	heating rate (C/s	heating time	holding time (	Eff. Strain (mm/mm	Eff. Strain rate (1/	Shear strain (Eff. Strain x √3	Shear strain rate (Eff. Strain rate x √3)	Rotations (Radian	Revolutio	Rotation (real) after the t	Rotation time (	Rotationszeit (m	graphit	vacu		p	data	comments
14/6/2018	Titanium 64	20	10	10,1	950,1000, 1050	5	190, 200, 210		0	0	0	0	0	0	0	#DIV/0!	#DIV/0!	yes	yes	yes	no	HTincrement .d02	Objective: Temperature gradient. 3 K thermocouples, 2 layers graphite foil and little Ni paste, Ar pressure reduced from 12 to 9 l/min, Ar flow stopped at 6 inch Hg, no smoke coming out, successful experiment
12.09.17	Titanium 64	20	10	10,1	1010	5	202	300	7,3	0,1	12,6439709	0,173205081	50,57588358	8,049401873	5	73	1,21666667	no	yes	yes	no	Ti64_1010_01_8rev.d01	Objective: do first torsion test with Ti64 and new sample holders, 2 S thermocouples (long, positioned on bottom of the sample and turned around, welded with hand welding machine) PTemp 40 degrees lower because TC on shoulder in regulating, Ar flowing 9l/min, 5x flushing chamber with Ar (to 1 in Hg) then keep chamber sealed, T-gradient 40 C, decreased after 5 rev; successful test
13/9/2018	Titanium 64	20	10	10,1	1030	5	206	300	7,3	0,1	12,6439709	0,173205081	50,57588358	8,049401873	8	73	1,21666667	no	yes	yes	no	Ti64_1030_01_8rev.d01	2 S thermocouples (long, positioned on bottom of the sample and turned around), Ar flowing 9l/min, 5x flushing chamber with Ar (to 1 in Hg) then keep chamber sealed, T-gradient 35-40 C, successful test
13/9/2018	Titanium 64	20	10	10,1	1050	5	210	300	5,4	0,1	9,353074361	0,173205081	37,41229744	5,954352071	6	54	0,9	no	yes	yes	no	Ti64_970lam_01_6rev.d01	HT: hold 10 min at 1050, cool down to 970 with 40K/min, hold at 970 for 5 min; 2 S thermocouples (long, positioned on bottom of the sample and turned around), Ar flowing 9l/min, 5x flushing chamber with Ar (to 1 in Hg) then keep chamber sealed, T-gradient 35C, 6 revolutions programmed due to lammelar structure, heavy corrosion during HT, successful test
13/9/2018	Titanium 64	20	10	10,1	1050	5	210	300	7,3	0,1	12,6439709	0,173205081	50,57588358	8,049401873	8	73	1,21666667	no	yes	yes	no	Ti64_950lam_01_8rev.d01	HT: hold 10 min at 1050, cool down to 950 with 40K/min, hold at 950 for 5 min; 2 S thermocouples (long, positioned on bottom of the sample and turned around), Ar flowing 9l/min, 5x flushing chamber with Ar (to 1 in Hg) then keep chamber sealed, 8rev, L Gauge heavily deformed, heavy corrosion during HT, successful test
13/9/2018	Titanium 64	20	10	10,1	1050	5	210	300	7,3	1	12,6439709	1,732050808	50,57588358	8,049401873	8	7,3	0,12166667	no	yes	yes	no	Ti64_1050_1_8rev.d01	2 S thermocouples (long, positioned on bottom of the sample and turned around), Ar flowing 9l/min, 5x flushing chamber with Ar (to 1 in Hg) then keep chamber sealed, T-gradient 35-40 C, successful test
13/9/2018	Titanium 64	20	10	10,1	1030	5	206	300	7,3	1	12,6439709	1,732050808	50,57588358	8,049401873	8	7,3	0,12166667	no	yes	yes	no	Ti64_1030_1_8rev.d01	2 S thermocouples (long, positioned on bottom of the sample and turned around), Ar flowing 9l/min, 5x flushing chamber with Ar (to 1 in Hg) then keep chamber sealed, T-gradient 30-35 C, successful test
13/9/2018	Titanium 64	20	10	10,1	1050	5	210	300	7,3	0,01	12,6439709	0,017320508	50,57588358	8,049401873	8	730	12,1666667	no	yes	yes	no	Ti64_1050_001_8rev.d01	2 S thermocouples (long, positioned on bottom of the sample and turned around), Ar flowing 9l/min, 5x flushing chamber with Ar (to 1 in Hg) then keep chamber sealed, T-gradient 35-40 C, strong deformation in L Gauge, Machine truned slightly more than programmed 8 rev, successful test
13/9/2018	Titanium 64	20	10	10,1	1030	5	206	300	7,3	0,01	12,6439709	0,017320508	50,57588358	8,049401873	8	730	12,1666667	no	yes	yes	no	Ti64_1030_001_8rev.d01	2 S thermocouples (long, positioned on bottom of the sample and turned around), Ar flowing 9l/min, 5x flushing chamber with Ar (to 1 in Hg) then keep chamber sealed, T-gradient 10-15C at the end TC2 higher than TC1 (why?), Machine truned slightly more than programmed 8 rev, successful test
13/9/2018	Titanium 64	20	10	10,1	970	5	194	300	7,3	0,1	12,6439709	0,173205081	50,57588358	8,049401873	8	73	1,21666667	no	yes	yes	no	Ti64_970_01_8rev.d01	hold at 970 for 5 min; 2 S thermocouples (long, positioned on bottom of the sample and turned around), Ar flowing 9l/min, 5x flushing chamber with Ar (to 1 in Hg) then keep chamber sealed, successful test
13/9/2018	Titanium 64	20	10	10,1	950	5	190	300	7,3	0,1	12,6439709	0,173205081	50,57588358	8,049401873	8	73	1,21666667	no	yes	yes	no	Ti64_950_01_8rev.d01	hold at 970 for 5 min; 2 S thermocouples (long, positioned on bottom of the sample and turned around), Ar flowing 9l/min, 5x flushing chamber with Ar (to 1 in Hg) then keep chamber sealed, successful test
14/9/2018	Titanium 64	20	10	10,1	1050	5	210	300	7,3	0,1	12,6439709	0,173205081	50,57588358	8,049401873	8	73	1,21666667	no	yes	yes	no	Ti64_1050_01_8rev.d03	repetition of test with regulating TC on side, 2 S thermocouples (long, positioned on bottom of the sample and turned around), Ar flowing 9l/min, 5x flushing chamber with Ar (to 1 in Hg) then keep chamber sealed, successful test, experiment filmed
14/9/2018	Titanium 64	20	10	10,1	1050	5	210	300	7,3	1	12,6439709	1,732050808	50,57588358	8,049401873	8	7,3	0,12166667	no	yes	yes	no	Ti64_970lam_1_8rev.d01	HT: hold 10 min at 1050, cool down to 970 with 40K/min, hold at 970 for 5 min; 2 S thermocouples (long, positioned on bottom of the sample and turned around), Ar flowing 9l/min, 5x flushing chamber with Ar (to 1 in Hg) then keep chamber sealed, heavy corrosion during HT,L Gauge heavily deformed, quenching slightly later, successful test
14/9/2018	Titanium 64	20	10	10,1	1050	5	210	300	7,3	1	12,6439709	1,732050808	50,57588358	8,049401873	8	7,3	0,12166667	no	yes	yes	no	Ti64_950lam_1_8rev.d01	HT: hold 10 min at 1050, cool down to 950 with 40K/min, hold at 950 for 5 min; 2 S thermocouples (long, positioned on bottom of the sample and turned around), Ar flowing 9l/min, 5x flushing chamber with Ar (to 1 in Hg) then keep chamber sealed, 8rev, L Gauge heavily deformed, heavy corrosion during HT, turned little more than 8 rev, successful test
14/9/2018	Titanium 64	20	10	10,1	970	5	194	300	7,3	0,01	12,6439709	0,017320508	50,57588358	8,049401873	5,7	730	12,1666667	no	yes	yes	no	Ti64_970lam_001_8rev.d01	2 S thermocouples (long, positioned on bottom of the sample and turned around), Ar flowing 9l/min, 5x flushing chamber with Ar (to 1 in Hg) then keep chamber sealed, heavy corrosion during HT,L Gauge heavily deformed, quenching slightly later, interrupted test TC1 Fell off after 5,7 rev
14/9/2018	Titanium 64	20	10	10,1	1070	5	214	300	7,3	0,1	12,6439709	0,173205081	50,57588358	8,049401873	8	73	1,21666667	no	yes	yes	no	Ti64_1070_01_8rev.d01	2 S thermocouples (long, positioned on bottom of the sample and turned around), Ar flowing 9l/min, 5x flushing chamber with Ar (to 1 in Hg), successful test
14/9/2018	Titanium 64	20	10	10,1	1070	5	214	300	7,3	1	12,6439709	1,732050808	50,57588358	8,049401873	8	7,3	0,12166667	no	yes	yes	no	Ti64_1070_1_8rev.d01	2 S thermocouples (long, positioned on bottom of the sample and turned around), Ar flowing 9l/min, 5x flushing chamber with Ar (to 1 in Hg) then keep chamber sealed, T-gradient 35-40 C, successful test
14/9/2018	Titanium 64	20	10	10,1	1070	5	214	300	7,3	0,01	12,6439709	0,017320508	50,57588358	8,049401873	8	730	12,1666667	no	yes	yes	no	Ti64_1070_001_8rev.d01	2 S thermocouples (long, positioned on bottom of the sample and turned around), Ar flowing 9l/min, 5x flushing chamber with Ar (to 1 in Hg), turned little more than 8 rev, successful test

Figure 86:Protocol of hot torsion tests of Ti64.

Torsion samples prepared for metallography

Figure 87: Torsion samples with lamellar structure prepared for metallography. From top to bottom: 950°C 1 1/s, 970°C 1 1/s, 970°C 0.01 1/s, 970°C 0.1 1/s, 950°C 0.1 1/s.

Figure 88: Torsion samples prepared for metallography deformed at 970°C. From top to bottom: 970°C 0.1 1/s, 970°Clam 0.1 1/s, 970°Clam 1 1/s, 970°C 0.1 1/s, 970°C 0.01lam 1/s.

Figure 89: Torsion samples prepared for metallography deformed in the β field of Ti64. From top to bottom: 1070°C 1 1/s, 1070°C 0.01 1/s, 1030°C 0.01 1/s, 1070°C 0.1 1/s,10950°C 0.1 1/s.

Further results of the temperature correction of compression flow curves

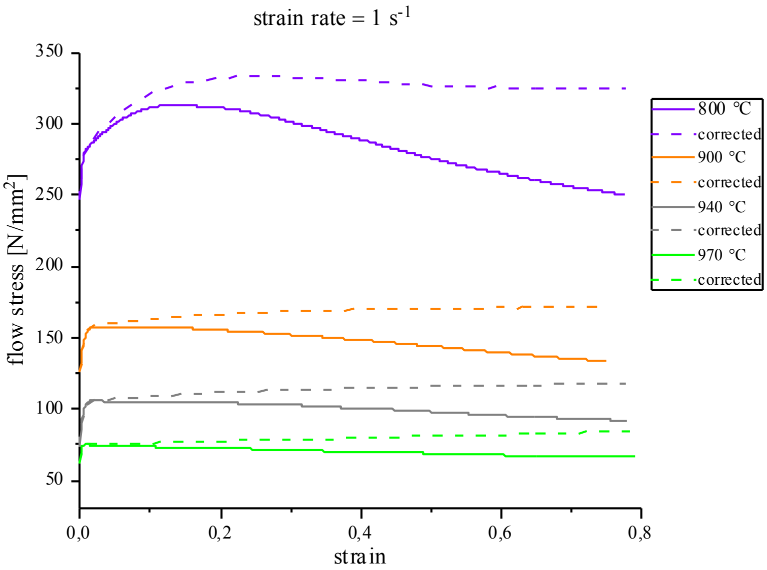

Figure 90: Temperature correction in the α+β field for a strain rate of 1 1/s.

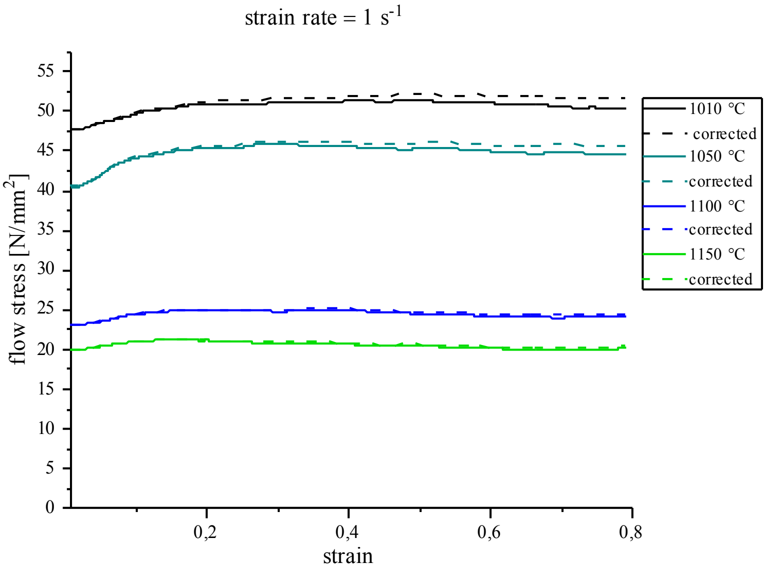

Figure 91: Temperature correction in the β field for a strain rate of 1 1/s.

Further results of the CDRX model

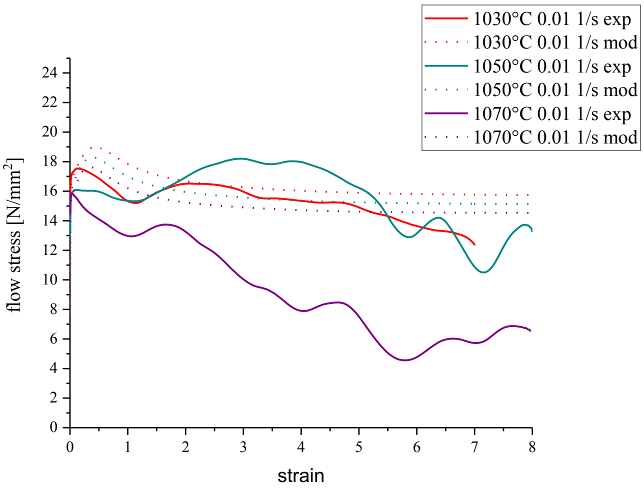

Figure 92: Modelled flow stress for a strain rate of 0.01 1/s.

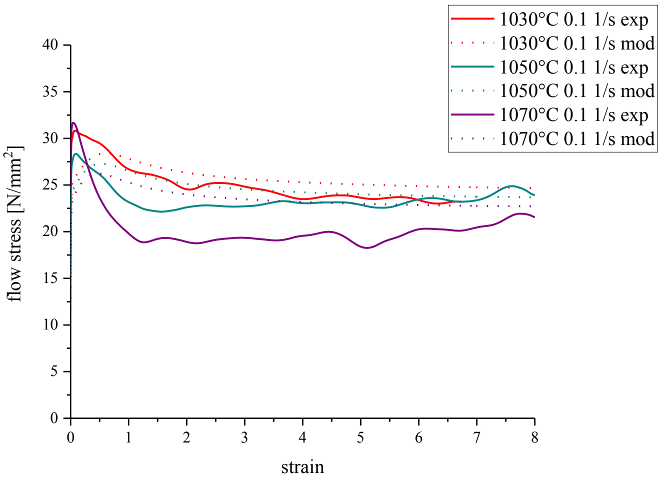

Figure 93: Modelled flow stress for a strain rate of 0.1 1/s.

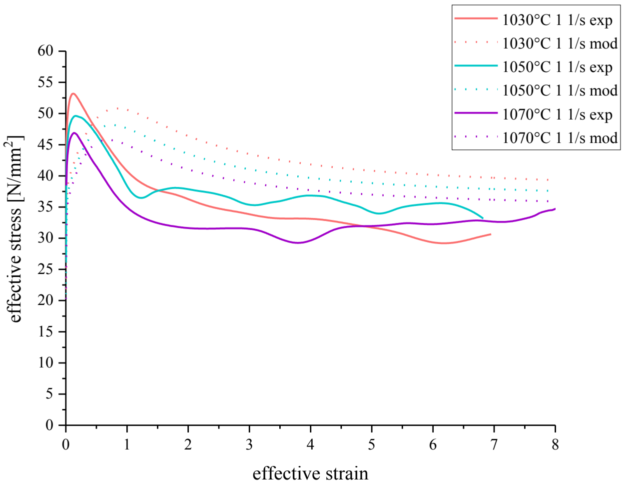

Figure 94: Modelled flow stress for a strain rate of 1 1/s.

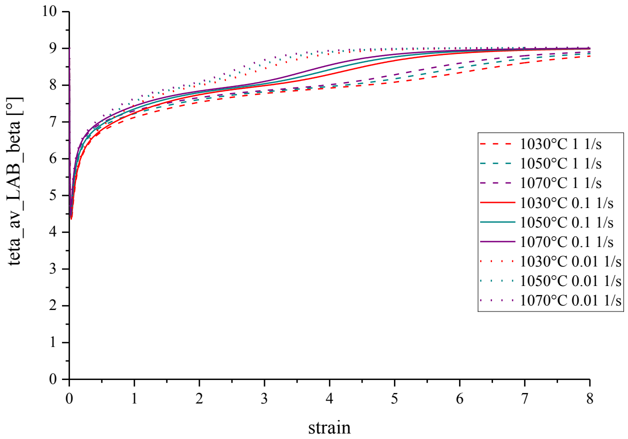

Figure 95: Average misorientation angle of LAB in the β phase of Ti64 as modelled with the CDRX model.

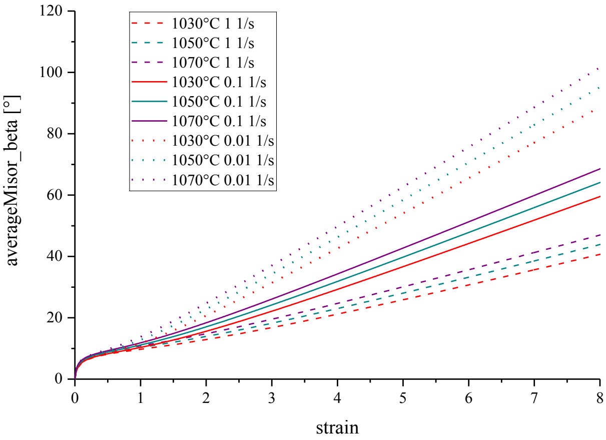

Figure 96: Average misorientation of the Rayleigh distribution in the β phase of Ti64 as modelled with the CDRX model.

Further pictures of prepared metallography samples

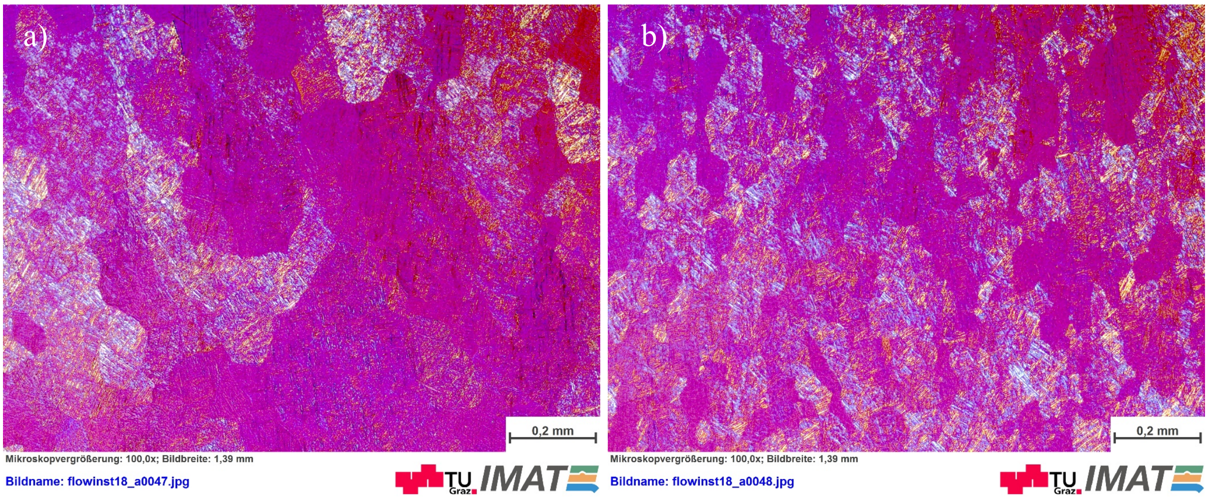

Figure 97: 970°C 0.1 1/s strain rate in polarized light. a) center of sample. b) bottom center.

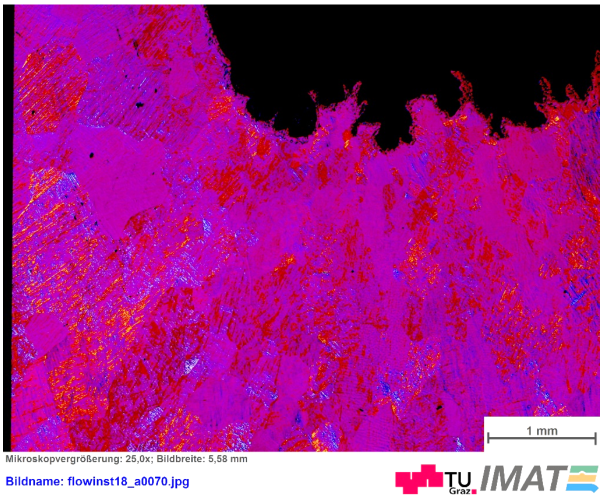

Figure 98: transition from deformed to undeformed material 1030°C 0.01 1/s.

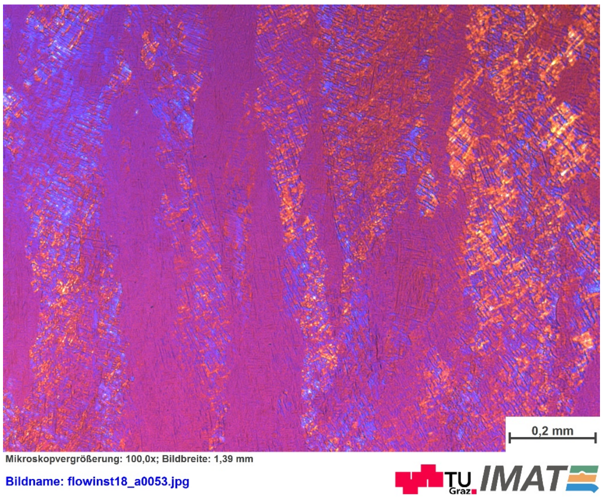

Figure 99: polarized light. a) 950lam 1 1/s, large deformed grains, martensite gradient?

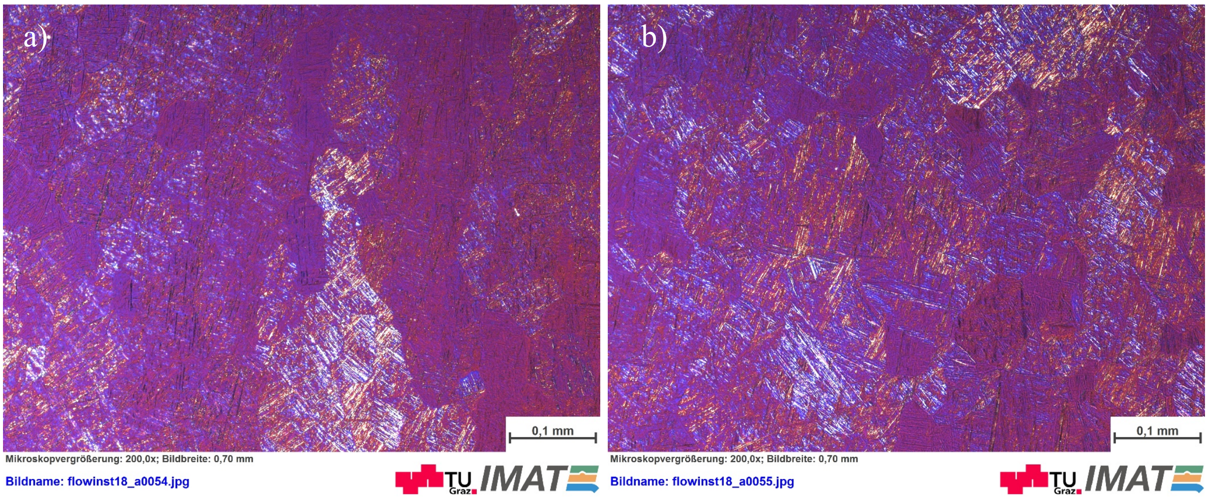

Figure 100: 1070°C 1 1/s strain rate in polarized light. a) center of sample. b) bottom center.

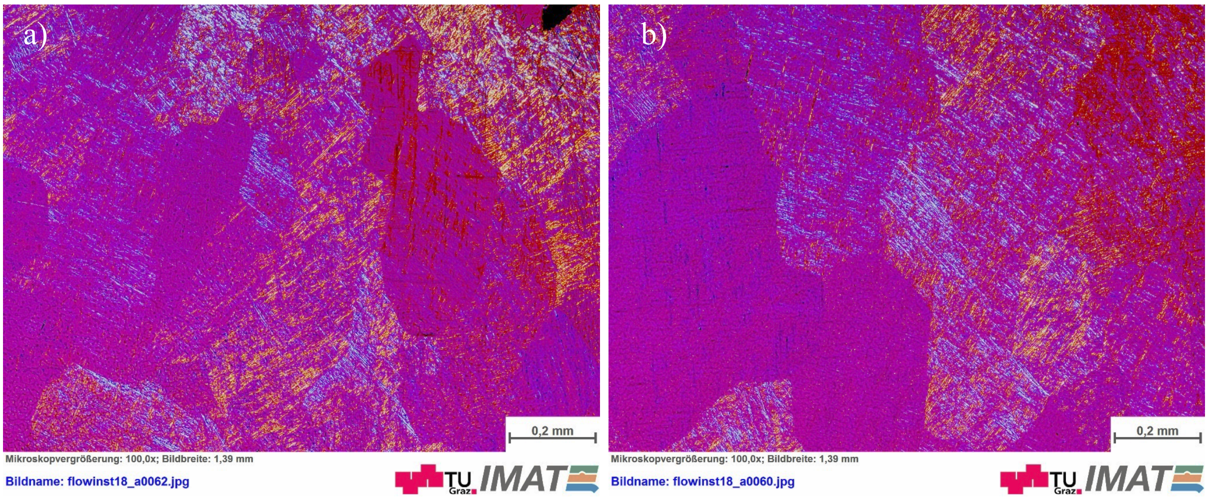

Figure 101: 1070°C 0.01 1/s strain rate in polarized light. a) center of sample. b) bottom center.

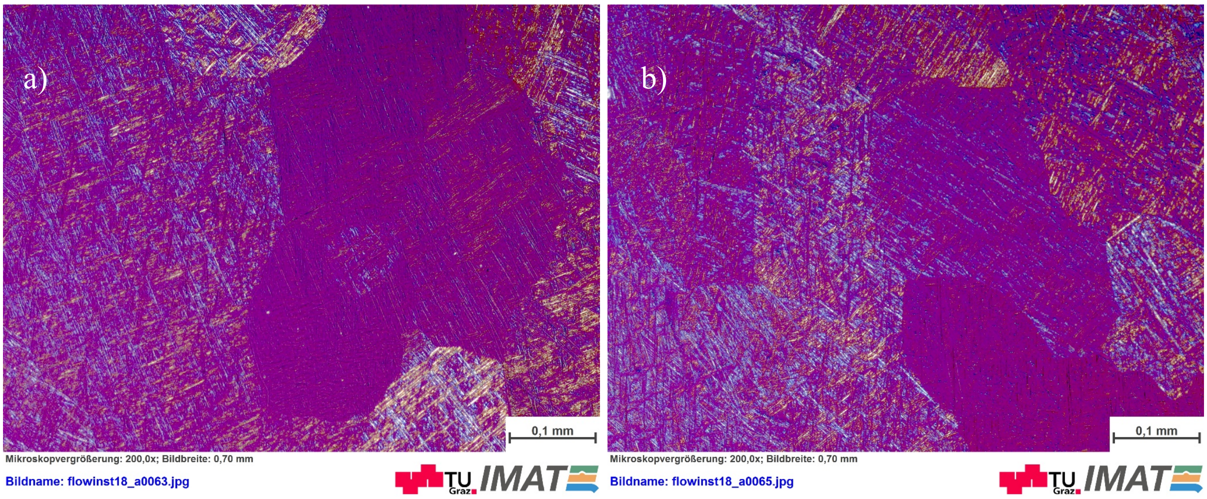

Figure 102: 1050°C 0.01 1/s strain rate in polarized light. a) center of sample. b) bottom center.

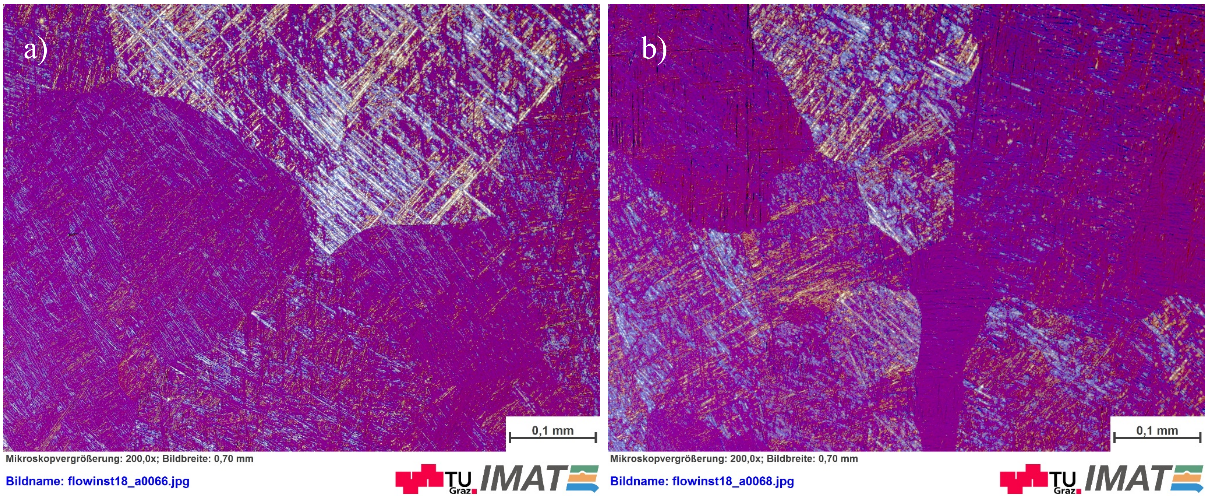

Figure 103: 1030°C 0.01 1/s strain rate in polarized light. a) center of sample. b) bottom center.